# STRUCTURAL, ELECTRONIC AND MAGNETIC PROPERTIES OF VARIOUS NANOSYSTEMS: MOLECULAR DYNAMICS SIMULATIONS AND DENSITY FUNCTIONAL THEORY CALCULATIONS

A THESIS SUBMITTED TO
THE GRADUATE SCHOOL OF NATURAL AND APPLIED SCIENCES
OF
MIDDLE EAST TECHNICAL UNIVERSITY

BY

SHOLEH ALAEI

IN PARTIAL FULFILLMENT OF THE REQUIREMENTS
FOR
THE DEGREE OF DOCTOR OF PHILOSOPHY
IN
PHYSICS

APRIL 2014

Approval of the thesis:

**STRUCTURAL, ELECTRONIC AND MAGNETIC PROPERTIES OF VARIOUS NANOSYSTEMS: MOLECULAR DYNAMICS SIMULATIONS AND DENSITY FUNCTIONAL THEORY CALCULATIONS**

submitted by **SHOLEH ALAEI** in partial fulfillment of the requirements for the degree of **Doctor of Philosophy in Physics Department**, **Middle East Technical University** by,

Prof. Dr. Canan Özgen _____
Dean, Graduate School of **Natural and Applied Sciences**

Prof. Dr. Mehmet T. Zeyrek _____
Head of Department, **Physics**

Prof. Dr. Şakir Erkoç _____
Supervisor, **Physics Dept., METU**

Prof. Dr. Seifollah Jalili
Co-Supervisor, **Chemistry Dept., K. N. T. Univ. of Tech., Iran** _____

**Examining Committee Members:**

Prof. Dr. İshak Karakaya, _____
Metallurgical and Materials Engineering Dept., METU

Prof. Dr. Şakir Erkoç _____
Physics Dept., METU

Prof. Dr. Bilal Güneş _____
Physics Education Dept., Gazi University

Prof. Dr. Ramazan Sever _____
Physics Dept., METU

Assoc. Prof. Dr. Hande Toffoli, _____
Physics Dept., METU

**Date: 25 .04.2014**

**I hereby declare that all information in this document has been obtained and presented in accordance with academic rules and ethical conduct. I also declare that, as required by these rules and conduct, I have fully cited and referenced all material and results that are not original to this work.**

Name, Last name: **SHOLEH ALAEI**

Signature :

## ABSTRACT

STRUCTURAL, ELECTRONIC AND MAGNETIC PROPERTIES OF VARIOUS NANOSYSTEMS: MOLECULAR DYNAMICS SIMULATIONS AND DENSITY FUNCTIONAL THEORY CALCULATIONS

Sholeh Alaei

Ph.D., Department of Physics

Supervisor: Prof. Dr. Şakir Erkoç

Co-Supervisor: Prof. Dr. Seifollah Jalili

April 2014, 171 pages

In this study, we aim to investigate the structural, magnetic and electronic properties of various nanosystems using molecular dynamics simulation technique and density functional theory calculations. In the first part, iron oxide nanostructures (nanorods, clusters and nanoparticles) were considered. We applied strain, at different temperatures, on nanorods in order to study stability of iron oxide nanorods using molecular dynamics simulation. Furthermore, radial distribution functions of iron oxide nanoparticles at different temperatures using the same mentioned method are calculated. Besides, the electronic and magnetic properties of $(Fe_2O_3)_n$ (n=2-5) clusters were studied using Density Functional Theory. It came out that the most stable structures for n=2, 3 were ferromagnetic and for n=4, 5 were antiferromagnetic. It was found that by increasing 'n' the binding energy ($E_b$) increased, while such an observation was not seen for n=4 and n=5 and the relative energy was equal in these cases. An interesting result was that one of the states for n=4 (n4-1) was a half-metallic anti ferromagnetic, which is important in spintronics applications. The last part of this survey was pursuing the effect of transition metal atoms (Fe-Co-Ni)

adsorptions on magnetic and electronic properties of graphyne nanotubes. Magnetic atom doped graphyne nanotubes show interesting magnetic properties.

Keywords: Iron Oxide Nanorods, Iron Oxide Clusters, Graphyne Nanotubes, Molecular Dynamics, Density Functional Theory

# ÖZ

ÇEŞİTLİ NANOYAPILARIN YAPISAL, ELEKTRONİK VE MANYETİK ÖZELLİKLERİ: MOLEKÜL DİNAMİĞİ BENZETİMLERİ VE YOĞUNLUK FONKSİYONELİ KURAMI HESAPLARI

Sholeh Alaei

Doktora, Fizik Bölümü

Tez Yöneticisi : Prof. Dr. Şakir Erkoç

Ortak Tez Yôneticisi: Prof. Dr. Seifollah Jalili

Nisaan 2014, 171 sayfa

Bu çalışmada muhtelif nanoyapıların yapısal, elektronik ve manyetik özellikleri Molekül Dinamiği benzetişim yöntemi ve Yoğunluk Fonksiyoneli Kuramı hesapları ile yapılmıştır. İlk önce demir oksit nanoyapıların (nanoçubuklar, topaklar ve nanoparçacıklar) yapısal, manyetik ve elektronik özellikleri incelenmiştir. Demir oksit nanoçubukların sağlamlığını incelemek için Molekül Dinamiği kullanarak nanoçubuklara farklı sıcaklıklarda gerilme uygulanmıştır. Ayrıca, farklı sıcaklıklardaki demir oksit nanoparçacıklarının radyal dağılım fonksiyonları hesaplanmıştır. Bunun yanısıra, topakların $(Fe_2O_3)_n$ (n=2-5) elektronik ve manyetik özellikleri yoğunluk fonksiyoneli kuramı kullanılarak incelenmiştir. Hesap sonuçlarına göre en dayanıklı yapılar n=2, 3 için ferromanyetik ve n=4, 5 için antiferromanyetiktir. Topakların göreceli enerjisi n=4 ve n=5 için değişmezken, 'n' arttırıldığında bağlanma enerjisinin ($E_b$) de arttığı görülmüştür. İlgi çekici bir sonuç, n=4 (n4-1) için olan durumların spintronik uygulamalarında önemli olabileceği yarı-metalik antiferromanyetiktir. Bu çalışmanın son bölümü, geçiş metal atomları (Fe-Co-Ni) ile katkılandırılmış graphyne nanotüplerinin manyetik ve elektronik özelliklerinin incelenmesi hakkındadır.

Manyetik atomlar ile katkılandırılan graphyne nanotüpler ilginç manyetik özellikler göstermektedir.

Anahtar Kelimeler: Demir Oksit Nanoçubuk, Demir Oksit Topak, Graphyne Nanotüp, Molekül Dinamiği, Yoğunluk Fonksiyoneli Kuramı.

**To My Loving Family**

## ACKNOWLEDGMENTS

I would like to express my deepest gratitude and thanks to my supervisor, Prof. Dr. Şakir Erkoç, for his patient guidance, inspiration, encouragement, being accessible and willing to help me all the time for giving me the tools to tackle problems. I am much grateful to him for all he has done for me.

It is my great pleasure and privilege to express my heartfelt gratitude to my co-supervisor, Prof. Dr. Seifollah Jalili, for his advice and support and feedback through every stage of this research. I am also grateful to have such a positive role model as my mentor.

Both of my advisers have inspired me by their great research capabilities and desire to accomplish great goals. These are lessons that will benefit me for a lifetime. Thanks to both of them for all of the talks, advice, motivation and for being always ready for listening to me.

Special thanks to Dr. Hande Toffoli for her DFT class and helping me develop the skills to accomplish this dream. She is truly an inspiration and a model for the teacher I wish to become and also a model for my life.

I would like to extend my gratitude to my committee members for their constructive suggestions in my research and help throughout my graduate studies and their contributions to this project.

A very special thanks goes out to my friends and my roommate for their help, friendship, smiling faces and support. Special thanks to Pantea Aurang, Arezo Hoseini, Hamid Reza Shojaei and Ali Taheri for the fun times and their help during the last few years.

Finally and the most importantly I would like to thank my family, my father, my mother, my sister and my brother for the moral support and patience during my study and through my entire life. They have been the joy of my life, without my family, I could never have dreamed this big. THANKS!

## TABLE OF CONTENTS

ABSTRACT ..... V

ÖZ ..... VII

ACKNOWLEDGMENTS ..... X

TABLE OF CONTENTS ..... XI

LIST OF TABLES ..... XIV

LIST OF FIGURES ..... XVI

CHAPTERS

1 INTRODUCTION ..... 1

1.1. ZERO-DIMENSIONAL (0D) NANOMATERIALS ..... 2

1.1.1. Clusters ..... 5

1.2. ONE-DIMENSIONAL (1D) NANOMATERIALS ..... 6

1.3. IRON OXIDES ..... 7

1.4. MAGNETIC PROPERTIES ..... 12

1.4.1. Classification of Magnetic Materials ..... 18

1.4.1.1. Diamagnetism ..... 18

1.4.1.2. Paramagnetism ..... 20

1.4.1.3 Ferromagnetism ..... 21

1.4.1.4 Antiferromagnetism ..... 23

1.4.1.5. Ferrimagnetism ..... 25

1.4.2. Magnetic Behavior of Iron Oxides ..... 26

1.5. GRAPHYNE ..... 29

2 THEORETICAL METHODS ..... 33

2.1. MOLECULAR DYNAMICS METHOD ..... 33

2.1.1. Canonical Ensemble ..... 34

2.1.2. Verlet Algorithm ..... 37
2.1.3. Periodic Boundary Condition (PBC) ..... 38
2.1.4. Property Calculation ..... 39
2.2. DENSITY FUNCTIONAL THEORY ..... 40
2.2.1. Born-Oppenheimer approximation ..... 40
2.2.2. Hartree-Fock (HF) Approximation ..... 43
2.2.3. Density Functional Theory Principals ..... 46
2.2.3.1. Hohenberg-Kohn Theorem ..... 46
2.2.3.2 The Kohn-Sham Approach ..... 49
2.2.3.3. The Local Density Approximation (LDA) ..... 52
2.2.3.4. Generalized Gradient Approximation (GGA) ..... 54
3 SYSTEMS STUDIED ..... 57
3.1. STRUCTURAL PROPERTIES OF B-$Fe_2O_3$ NANORODS UNDER STRAIN: MOLECULAR DYNAMICS SIMULATIONS ..... 57
3.1.1. Introduction ..... 57
3.1.2. Modeling and Simulation ..... 59
3.1.3. Results and Discussion ..... 67
3.2. STRUCTURAL PROPERTIES AND RADIAL DISTRIBUTION FUNCTION OF IRON OXIDE SPHERICAL NANOPARTICLES USING MOLECULAR DYNAMICS SIMULATION ..... 79
3.2.1. Introduction ..... 79
3.2.2. Methods of Simulation ..... 79
3.2.3 Results and Discussion ..... 81
3.3. STUDY OF ELECTRONIC AND MAGNETIC PROPERTIES OF $(Fe_2O_3)_N$ CLUSTERS: USING DENSITY FUNCTIONAL THEORY ..... 96
3.3.1. Introduction ..... 96
3.3.2. Computational Methods ..... 100
3.3.3. Results and Discussion ..... 101
3.3.3.1. $Fe_2O_3$ Molecule (n = 1) ..... 102
3.3.3.2 $(Fe_2O_3)_{n=2}$ Cluster ..... 103

3.3.3.3. $(Fe_2O_3)_{n=3}$ Cluster ..... 108
3.3.3.4. $(Fe_2O_3)_{n=4}$ and $(Fe_2O_3)_{n=5}$ Clusters ..... 113
3.4. STUDY OF THE INFLUENCE OF TRANSITION METAL ATOMS ON ELECTRONIC AND MAGNETIC PROPERTIES OF GRAPHYNE NANOTUBES USING DENSITY FUNCTIONAL THEORY ..... 122
3.4.1. Introduction ..... 122
3.4.2. METHOD OF CALCULATION ..... 125
3.4.3. Results and Discussion ..... 130
3.4.3.1. (2,2) GNT ..... 130
3.4.3.2. (3,0) GNT ..... 133
3.4.3.3. (3,3) and (5,0) GNTs ..... 134
3.4.3.4. Magnetic and Electronic Properties ..... 134
4 CONCLUSIONS ..... 147
REFERENCES ..... 151
CURRICULUM VITAE ..... 169

## LIST OF TABLES

TABLES

Table 1.1 Exchange interactions in iron oxides. Adapted from Ref. [45]. ..... 27

Table 1.2 The distribution of spin magnetic moments for $Fe^{2+}$ and $Fe^{3+}$ ions in a unit cell $Fe_3O_4$. Adapted from Ref. [41]. ..... 29

Table 3. 1 The potential parameters used for PEF1. Adapted from Ref. [109]…..... ...63

Table 3. 2 The potential parameters used for PEF2 [110]. ..... 65

Table 3. 3 Spin states obtained for $Fe_4O_6$ cluster (Refer to Fig. 3.18 for atom numbering). Atomic magnetic moments are represented in Bohr mag/cell [156]. ..... 105

Table 3. 4 Properties of three low-energy spin configuration states obtained for the $Fe_4O_6$ cluster [156]. ..... 107

Table 3. 5 Stable spin configuration states and atomic magnetic moments of each Fe atoms for $Fe_6O_9$ cluster, atom numbering is shown in Fig. 3.21 [156]. ..... 110

Table 3. 6 Properties of three low-energy stable spin configuration states obtained for the $Fe_6O_9$ cluster [149]. ..... 111

Table 3. 7 Properties of three low-energy stable spin configuration states obtained for the $Fe_8O_{12}$ cluster. ..... 117

Table 3. 8 Properties of three low-energy stable spin configuration states obtained for the $Fe_{10}O_{15}$ cluster. ..... 118

Table 3. 9 Properties of four studied graphyne nanotubes (GNTs) ..... 129

Table 3. 10 Summary of results for transition metal adsorption on a (2, 2) GNTs [193]. ..... 132

Table 3. 11 Summary of results for transition metal adsorption on (3,0) graphyne nanotube. ..... 135

Table 3. 12 Results for transition metal adsorption on (3,3) graphyne nanotube ..... 136

Table 3. 13 Results for transition metal adsorption on (5,0) graphyne nanotube ..... 137

Table 3. 14 Properties of graphyne nanotubes with a transition metal (TM) atom adsorbed on the h1 site. $E_b^p$ and $E_b^u$ are binding energies obtained from spin-polarized and spin-unpolarized calculations, respectively. $d_{TM\text{-}GNT}$ is the average distance of the transition metal from six neighboring carbon atoms, $\mu_B$ is the net magnetic moment of the system and $C$ is the charge transferred from the metal to nanotubes ..... 138

## LIST OF FIGURES

FIGURES

Figure 1. 1 Dimensionality classification of nanostructures. Adapted from Ref. [5]. ... 3

Figure 1.2 Classification of Nanomaterials (a) 0D clusters, (b) 1D nanotubes, filaments, and rods, (c) 2D films and layers (d) 3D polycrystals. Adapted from Ref. [6]. ..... 4

Figure 1.3 A model of a part of the bulk hematite structure. Crystallographic directions are shown. Oxygen layers alternate with Fe layers in the [001] direction. Adaptef from Ref. [29]. ..... 9

Figure 1.4 Crystal packing in the structure of $\gamma$-$Fe_2O_3$, the view onto (100). The circles which are shaded represents Fe atoms and white ones represent O atoms. Adapted from Ref. [30] ..... 11

Figure 1.5 Crystal packing in the structure of $\beta$-$Fe_2O_3$, the view onto (110). Fe, shaded circles represent Fe atoms and white ones show O atoms. Adapted from Ref. [23]..... 11

Figure 1.6 An orbiting electron which is equivalent to magnetic dipole moment. Adapted from Ref. [39]. ..... 13

Figure 1.7 Spin magnetic moment precesses about an external magnetic field around z and has a value $\mu_z$ along z. Adapted from Ref. [39]. ..... 14

Figure 1.8 Representation of magnetic dipoles, before and after applying external magnetic field. Adapted from Ref. [41]. ..... 17

Figure 1.9 A typical hysteresis loop for a ferro-or ferrimagnet. Adapted from Ref. [40]..... 17

Figure 1.10 Coercivity and retentivity points of a typical hysteresis loop. Adapted from Ref. [40]. ..... 18

Figure 1.11 A diamagnetic material which is placed in a nonuniform magnetic field. Adapted from Ref. [39]. ..... 20

Figure 1.12 (a) The atomic dipole configuration for a diamagnetic material in the presence and absence of an external magnetic field. Without an external field there is no dipoles, but with a magnetic field, dipoles are induced that are aligned in the opposite direction to the external field. (b) Atomic dipole configuration of a paramagnetic material in the presence and absence of an external magnetic field. Adapted from Ref. [41]. ..... 22

Figure 1.13 Schematic illustration of mutual alignment of atomic dipoles in a ferromagnetic material. Adapted from Ref. [41]. ..... 23

Figure 1.14 Curie-Weiss Law for ferromagnetism. Adapted from Ref. [44]. ..... 23

Figure 1.15 Ordering of magnetic ions in an antiferromagnetic lattice. Adapted from Ref. [41]. ..... 24

Figure 1.16 Typical temperature dependence of susceptibility in an antiferromagnet. Adapted from Ref. [40]. ..... 25

Figure 1.17 Comparison of magnetization and inverse susceptibility in typical ferri- and ferromagnets. Adapted from Ref. [40]. ..... 26

Figure 1.18 Magnetic ordering in the ferromagnetic crystal. The A atoms possess aligned spins in on direction, and the spins of B atoms are aligned in opposite direction. Since the magnetic moment of A and B atoms are not equal so the net magnetization, M, is not zero in the crystal. Adapted from Ref. [39]. ..... 27

Figure 1.19 Schematic diagram of the spin magnetic moments configuration for $Fe^{2+}$ and $Fe^{3+}$ ions in $Fe_3O_4$. Adapted from Ref. [46]. ..... 28

Figure 2. 1 Two dimensional periodic boundary condition. Adapted from Ref. [64].. 40

Figure 3. 1 The unit cell of β-Fe2O3. Atoms in gray are oxygens (O) and in black are irons (Fe)…..60

Figure 3. 2 Comparison between Morse potential and Harmonic oscillator potential. $D0$ is the dissociation energy, which is slightly different from the well depth $De$. Adapted from Ref. [112]. ..... 62

Figure 3. 3 Schematic representation of Lennard–Jones potential function. This graph shows regions of attraction and repulsion. Atoms try to minimize their potential energy are sitting at the bottom of the potential curve. When the atomic separations are to the left of the minimum the atoms repel, otherwise they attract one another. Adapted from Ref. [114]..... 64

Figure 3. 4 Illustration of the strain application ..... 66

Figure 3. 5 The β-$Fe_2O_3$ nanorod under strain with PEF1 at 1 K. Each of pictures are sideviews of nanorods at the represented strain step number..... 68

Figure 3. 6 The β-$Fe_2O_3$ nanorod under strain with PEF1 at 300 K..... 70

Figure 3. 7 The β-$Fe_2O_3$ nanorod under strain with PEF2 at 1 K..... 72

Figure 3. 8 The β-$Fe_2O_3$ nanorod under strain with PEF2 at 300 K..... 74

Figure 3. 9 (Color online) Strain $(\%\Delta L)$ versus strain-energy $(E_s$, in eV$)$ curves..... 78

Figure 3. 10 Space discretization for the evaluation of the radial distribution function (RDF)..... 80

Figure 3. 11 Relaxed structure of spherical nanoparticle with r= 3 Å at T=1K and radial (atomic) distribution function (RDF). Black and red lines are related to distribution function of Fe and O atoms, and the green line displays distribution pattern of all atoms. ..... 82

Figure 3. 12 (a) – (g) Relaxed structures of spherical nanoparticle with r= 3 Å, at temperatures 100 K to 900 K, and the related radial (atomic) distribution functions (RDF). ..... 83

Figure 3. 13 Relaxed structures of spherical nanoparticle with radius 4 Å at temperature 1K to 900 K with interval 100 K. ..... 86

Figure 3. 14 Relaxed structures of spherical nanoparticle with radius 5 Å at temperature 1K to 900 K with interval 100 K. ..... 89

Figure 3. 15 Relaxed structures of spherical nanoparticle with radius 6 Å at temperature 1K to 900 K with interval 100 K. ..... 93

Figure 3. 16 Relaxed structure of the rhombohedral unit cell of hematite. Blue (Gray) color represents iron atoms and red (dark gray) represents oxygen atoms. We will follow the same convention throughout. ..... 102

Figure 3. 17 Relaxed structure for the $(Fe_2O_3)_{n=1}$ cluster. The arrows show the spin polarization of Fe atoms. ..... 103

Figure 3. 18 Initial structure for $(Fe_2O_3)_{n=2}$ cluster (a) and optimized structure for $(Fe_2O_3)_{n=2}$ (b). ..... 104

Figure 3. 19 The values of atomic magnetic moments for Fe atoms of three low-energy spin configuration states [156]. ..... 106

Figure 3. 20 Density of states (DOS) for n2-1 (a), n2-2 (b), and n2-3 (c) $Fe_4O_6$ clusters. Upper and lower panels are for spin-up and spin-down states, respectively. Zero energy indicates the position of the highest occupied level [156]. ..... 109

Figure 3. 21 Relaxed structures for the $(Fe_2O_3)_n$ clusters with $n$ = 3. For each type of the optimized bond lengths (Fe–$O_r$ and Fe–$O_b$), one number is shown. ..... 110

Figure 3. 22 The values of atomic magnetic moments for Fe atoms of the first two low- energy spin configuration states of $Fe_6O_9$ cluster. ..... 111

Figure 3. 23 Density of states (DOS) for n3-1 (a), n3-2 (b), and n3-3 (c) $Fe_6O_9$ clusters. Upper and lower panels are for spin-up and spin-down states, respectively. ..... 113

Figure 3. 24 Optimized structures for the $(Fe_2O_3)_n$ clusters with $n$ = 4 (a) and n=5 (b). For each type of the optimized bond lengths (Fe–$O_r$ and Fe–$O_b$), one number is shown. ..... 115

Figure 3. 25 The values of atomic magnetic moments for Fe atoms of the first low-energy spin configuration states of $Fe_8O_{12}$ cluster. ..... 116

Figure 3. 26 The values of atomic magnetic moments for Fe atoms of the two low-energy spin configuration states of $Fe_{10}O_{15}$ cluster. ..... 117

Figure 3. 27 Density of states (DOS) for n4-1 (a), n4-2 (b), and n4-3 (c) $Fe_8O_{12}$ clusters. Upper and lower panels are for spin-up and spin-down states, respectively. ..... 120

Figure 3. 28 Density of states (DOS) for n5-1 (a) and n5-2 (b) $Fe_{10}O_{15}$ clusters. Upper and lower panels are for spin-up and spin-down states, respectively. ..... 121

Figure 3. 29 The γ-graphyne sheet unit cell (dashed hexagon) and some chiral vectors. Adapted from Refs. [17] and [36]. ..... 126

Figure 3. 30 A 2 × 2 supercell of graphyne sheet ( adsorption sites which are shown in this figure will be explained in the text). ..... 127

Figure 3. 31 Schematic presentations of (2, 2) graphyne nanotube ..... 128

Figure 3. 32 a) optimized transition metal-nanotube complex with the metal adsorbed on h1 site b) Co atom adsorbed on nanotube which has moved to h1 site from its original (values are Co-C bond lengths in Angstrom). Blue and gray balls represent the TM and carbon atoms, respectively [192]. ..... 131

Figure 3. 33 Spin-density isosurfaces for Fe (a) and Co (b) adsorbed (2,2) GNTs. Blue (dark) and yellow (light) regions correspond to positive and negative polarization, respectively. The isodensity value is 0.002 $\mu_B$/Bohr$^3$. ..... 139

Figure 3. 34 Electronic band structures for a bare (2,2) graphyne nanotube (a) and TM-adsorbed (2,2) nanotubes (b-f). Parts (b) to (f) are for TM = Fe (spin-up), Fe (spin-down), Co(spin-up), Co(spin-down), and Ni, respectively. The dashed line at zero energy indicates the position of the highest occupied level. ..... 140

Figure 3. 35 Electronic band structures for a bare (3,0) graphyne nanotube (a) and TM-adsorbed (3,0) nanotubes (b-f). Parts (b) to (f) are for TM = Fe (spin-up),

Fe(spin-down), Co(spin-up), Co(spin-down), and Ni, respectively. The dashed line at zero energy indicates the position of the highest occupied level. ..... 143

Figure 3. 36 Electronic band structures for a bare (3,3) graphyne nanotube (a) and TM-adsorbed (3,3) nanotubes (b-f). Parts (b) to (f) are for TM = Fe (spin-up), Fe (spin-down), Co(spin-up), Co(spin-down), and Ni, respectively. The dashed line at zero energy indicates the position of the highest occupied level. ..... 144

Figure 3. 37 Electronic band structures for a bare (5,0) graphyne nanotube (a) and TM-adsorbed (5,0) nanotubes (b-f). Parts (b) to (f) are for TM = Fe (spin-up), Fe (spin-down), Co(spin-up), Co(spin-down), and Ni, respectively. The dashed line at zero energy indicates the position of the highest occupied level. ..... 145

# CHAPTER 1

# INTRODUCTION

Nanotechnology or nanoscience deals with the production, characterization, synthesis, exploration, utilization and application of nano-sized objects and materials based on them, which are characterized by at least one dimension ranging from subnanometers to several nanometers ($1nm=10^{-9}m$) [1]. Nanotechnology, a broad and interdisciplinary field, covers the incorporation of most of the basic sciences, biology, physics, chemistry, material science, engineering and pharmacology. Exploring the nanoscale and tackling new subjects attached, propel to a further comprehension of materials and their uses and great potential applications, for instance, in electronics, nanomedicine, optics, energy storage, magnetism and material development which is what science and technology is in favor of [2,3]. The peculiarity of the nanoscale is related to being on the border of the atomic and macroscopic world. Nanostructures are like a bridge between atoms or molecules and infinite bulk systems.

Furthermore, nanomaterials have received more attention with the development of nanotechnology during recent decades. They possess large surface area to volume ratio in comparison to bulk forms, and therefore nanomaterials display unrivaled and totally different properties compared to their bulk components. As an example, for a crystal structure which is stable only at high temperatures, when its size reduces to nanometer, it may be stable even at very lower temperatures also, or ferromagnetic materials may lose their ferromagnetism when their sizes diminish to nanometer. Conductivity of materials also changes if their size reduces into nanoscale, for instance a bulk which is a semiconductor converts to an insulator in nanometer range [4].

One type of classification of nanostructures is based on the number of dimensions in nanoscale range. For zero dimensional (0D) nanomaterials, which all dimensions are at nanoscale, an electron is confined in 3D space. Nanoparticles, nanopores, atomic clusters and fullerenes are examples of 0D nanostructures called quantum dots. For one-dimensional (1D) nanomaterials like nanowire, nanorod, nanofiber and nanotubes, electron confinement takes place in 2D, whereas delocalization occurs along the long axis of nanorod/wire/tube. These 1D nanomaterials unfold promising properties since are the 1D quantum wires nanoscopic in diameter but microscopic in length. The conduction electrons in two-dimensional (2D) nanomaterials such as nanofilms and nanocoatings are confined across the thickness while delocalized in the plane of the sheet. In addition, bulk nanomaterials, as well as materials which possess nanocrystalline structures or bundles of nanowires are not confined to the nanoscale in any of directions lie within three-dimensional (3D) nanomaterials [1,2,5]. Figures 1.1 and 1.2 schematically show some examples of this classification of nanostructures [5,6].

In this work, we study nanostructures such as nanorods, nanoparticles and clusters of iron oxide and graphyne nanotubes and their electronic and magnetic properties in various conditions.

### 1.1. Zero-Dimensional (0D) Nanomaterials

As mentioned above about the definition of 0D nanostructures, we can say that zero-dimensional structures, with their marvelous properties, are the smallest building blocks of nanoscience and nanomaterials design [7]. Their small size and high surface to volume ratio and also quantum size effects brings forward unprecedented physical, structural, optical, magnetic and chemical properties. The effects of diminished size are characterized as two types, internal and external effects, as well as quantum and classical effects. The quantum size effects reveal themselves for example in the rise of specific low dimensional quantum states or in a blue shift of luminescence, magneto-

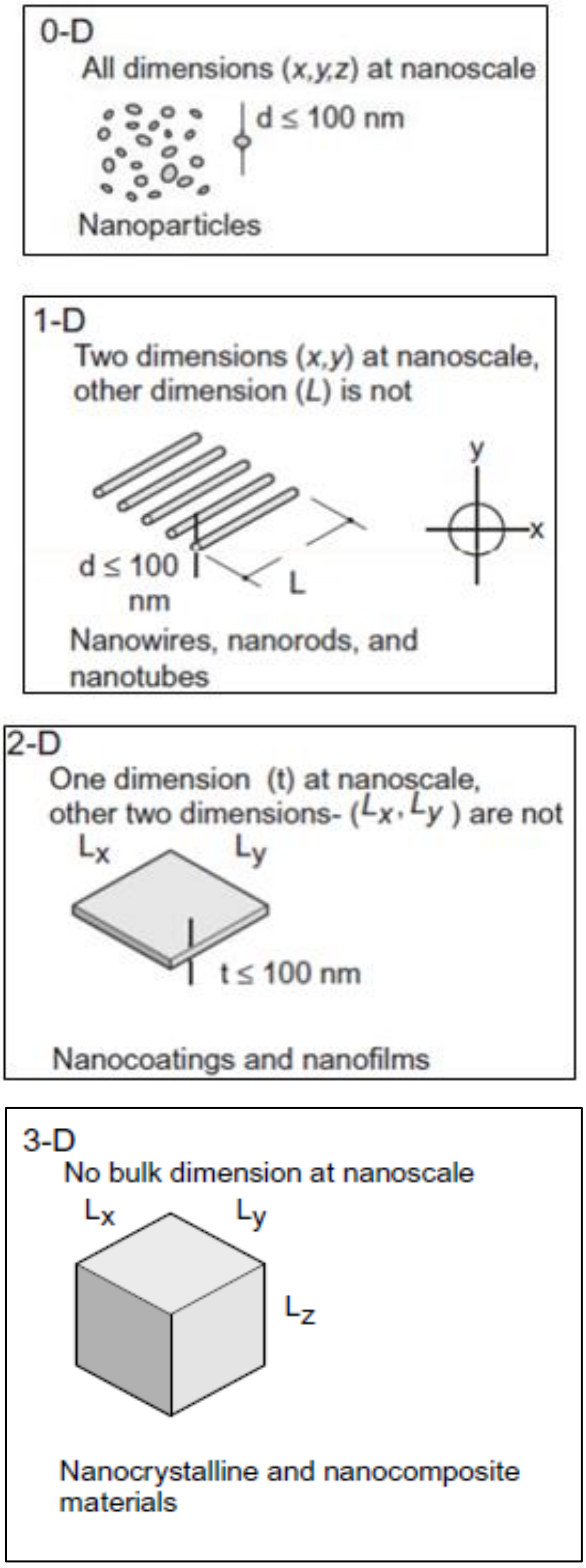


Figure 1. 1 Dimensionality classification of nanostructures. Adapted from Ref. [5].

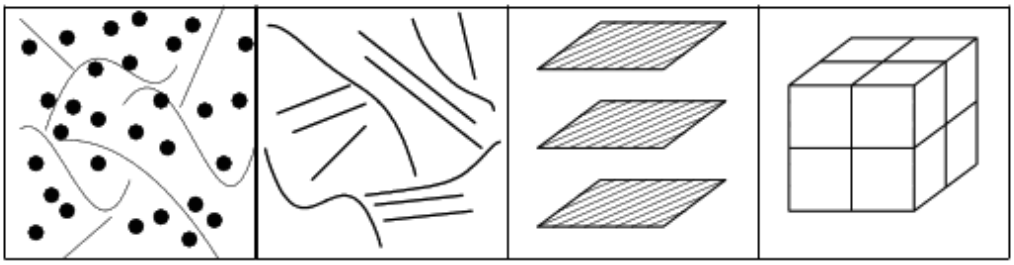


Figure 1. 2 Classification of Nanomaterials (a) 0D clusters, (b) 1D nanotubes, filaments, and rods, (c) 2D films and layers (d) 3D polycrystals. Adapted from Ref. [6].

resistance and other similar properties, while the classical effects become clear in variation of hardness, diffusion, thermal conductivity, plasticity. In turn the internal effects, regardless of external perturbations, include bandgap, melting temperature, luminescence, chemical activity and lattice parameters, the other effects are external ones which occur because of interaction between physical fields and materials whose size has been reduced to such a scale that is comparable with the free length of phonons, screening length and de Broglie wavelength of electrons. Noticing these matters, it is obvious that studying the unusual size-dependent properties in novel nanostructures has attracted high interest in recent decades. Since 0D nanostructures play significant role in building blocks for novel nanotechnology and also from an application point of view, keeping control over the morphology and composition of these structures, realizing and discovering of their various behaviors is necessary. Metals, metal oxides, carbon, silicates, biomolecules and polymers are some examples of nanoparticles. Metallic nanoparticles, due to their significant magnetization are considered for use in many areas rather than metal oxides, but since they are not enough stable against air, they should be used in oxidized form, which reduces their magnetizations. Fe, Ni and Co are samples of metallic nanoparticles [5,8].

### 1.1.1. Clusters

In general, clusters are groups of molecules and atoms whose size is, on average, between single atoms and molecules and bulk matter. One of the classifications of clusters is according to their size which is upon the number of atoms and molecules that constitute the clusters, so clusters can be small, medium-sized and large. The properties of small clusters alter suddenly with the variation in their sizes and shapes. Size variation effect in medium-sized and large clusters is smooth and changes with the number of constituents. The most important issue in the study of clusters is to recognize how atoms gather together in order to form a cluster and how the chemical and physical properties of a cluster change when its structure changes. Large number of atoms and molecules lie on the surface of clusters, since, in comparison with bulks, clusters possess a very large surface to volume [9,10], which is an important factor in surface chemistry for defining their properties. Some of the differences between bulk and clusters arise from the small volume of the potential well which confines the electrons in the clusters. The electrons, in this case, instead of having continuous bands, fill discrete levels. The numbers of atoms or molecules constituting the clusters are of considerable importance since not only the structure but also most of properties of clusters like relative stability, energy level spacing, magnetism, bonding and binding energy acutely depend on them. As an example the larger the number of atomic constituents of clusters are, the larger the number of local minima of the potential energy surface becomes. It should be pointed out that, in addition to the number of atoms in clusters, the type of the atoms and their bonding are also important. Thus, clusters can be classified into cluster molecules, semiconductor clusters, ionic clusters, metal clusters and rare gas clusters. Ionic clusters possess a large electronegativity difference between two elements and atoms are bound with an ionic bond. In semiconductor clusters, the bonds are strong and covalent. Metal clusters are diverse, as an example, the s-block metals delocalized metallic bond while transition metal clusters have many covalent bonds. Cluster molecules are among the more stable clusters and can exist in solid, liquid and gas. Furthermore, different kinds

of interactions of a cluster with electron, atom or other cluster are subject matters which appeared theoretically and experimentally. In addition, the interaction of a cluster with the external field has nonlinear response and is an emerging field of interest. Nanoclusters have been used in so many applications, whose number is swiftly increasing. Interest in using them as catalysis has developed [11] due to their desirable surface to volume ratio. In biological fields, they have received a lot of interest, for instance, gold nanocrystal molecules have been used with short segments of DNA for constructing a basis for finding out more about genetic sequences.

As pointed out before, the starting step for comprehending properties of clusters is recognizing their structure, their size, composition and related energy at stable structure.

One of the challenging subjects in nanoscience is the behavior of magnetism in the reduced dimension and how it approaches the bulk limit. According to the experimental investigations the magnetic behavior is extremely different from the corresponding bulk behavior and in some cases these properties are very unexpected and interesting. In fact, the magnetic property is exclusively sensitive to the size and kind of atoms and particles in a cluster. For instance, some nonmagnetic elements display strong magnetism in this size regime, or magnetization depends on external field non-monotonically. It should be mentioned that the number of atoms in clusters affect directly magnetic moment, i.e. as the size of cluster changes, the magnetic moment varies, but this variation is not smooth and results in interesting local structures. Magnetism in cluster science and in confined systems is a surprising and developing field and includes enormous implications to the emerging novel technology [3,11,14].

### 1.2. One-Dimensional (1D) Nanomaterials

One dimensional nanostructures like nanowires, nanorods may be metallic, semiconducting or insulating with diameter less than 100 nm and different lengths.

They are classified as one-dimensional materials due to the fact that the length to diameter ratio may reach up to 1000. At this scale the quantum mechanical effects become important and considerable; therefore such nanostructures are also called quantum wires. These promising nanostructures can be produced in a large variety of chemical compositions. Metallic: nickel, iron, gold, silver; zinc oxide (ZnO), magnesium oxide (MgO), iron oxide ($Fe_2O_3$), copper oxide and other metal oxides and semiconducting materials.

### 1.3. Iron Oxides

Magnetic properties and the nanomaterials which possess magnetic properties have become the focus of novel materials science by virtue of their various technological applications. Iron oxide nanomaterials, in particular, find broad applications and have attracted attention for their extensive usage in various cases like magnetic recording media, optical devices, cancer treatment, gas sensors and etc. [12-15]. In particular, iron oxide nanoparticles have created a powerful platform in diverse aspects of biomedical applications like magnetic resonance imaging (MRI) and also MRI-guided gene delivery or controlled drug delivery, cell labeling and many other cases [16].

Iron oxides are widespread in nature and are easily synthesized in the laboratories. Up to now, 16 iron oxide compounds have been discovered such as oxides, hydroxides or oxide-hydroxides. The most important and common ones are iron (II, III) oxide, magnetite ($Fe_3O_4$); iron (III) oxide ($Fe_2O_3$) and its various phases i.e. alpha phase, hematite ($\alpha$-$Fe_2O_3$); beta phase ($\beta$- $Fe_2O_3$); gamma phase, maghemite ($\gamma$-$Fe_2O_3$).

From the point of view of fundamental research, iron (III) oxide is a suitable compound in order to investigate the polymorphism, magnetic and structural phase transitions of nanoparticles. Furthermore, as mentioned above, from the viewpoint of experimental and applied studies, iron (III) oxide in all its various forms is one of the most generally used metal oxides with a lot of applications in many different environmental, industrial and biomedical fields. Since iron oxides are components of

several ores, they are used widely for the production of iron and steel and exist in some important archeological and geological earth-samples and some extraterrestrial materials. Iron (III) oxides components, due to their hardness and surface resistivity, catalytic activity, and the other properties such as magnetic, electronic and optical properties are used as catalysts, abrasives, gas sensors, polishing agents, pigments, photoanodes for photoelectrochemical cells or contrast agents in magnetic resonance imaging [17-22].

Small iron oxide particles and nanoparticles display some specific and unique characteristic and features which are different from well-crystallized particles. These iron oxide nanoparticles play an important role in the above mentioned applications including development of novel optical, magnetic and electronic devices, information storage, bioprocessing, magnetocaloric refrigeration, color imaging, magnetic recording media. The advantage of using iron (III) oxide nanoparticles in various fields is due to their chemical stability which is in contrast to the normally used ultrasmall particles of pure metals. Because of interesting application of iron (III) oxide nanoparticles in various fields, different sizes, structures and morphologies of these nanoparticles have been produced by using newly developed methods like laser pyrolysis, oxygen-hydrogen flame pyrolysis, micro-emulsion technique, sol-gel method, diode sputter deposition and etc. [17].

Hematite, alpha phase iron oxide, $\alpha$-$Fe_2O_3$, is the oldest iron oxide and the second most plentiful mineral in rocks and soils with a blood red color. Hematite is a valuable ore and an important pigment. Its structure is similar to corundum with a hexagonal unit cell and is sorely stable. Hematite can be also classified in the rhombohedral system; in this case it has two formula units per cell. For hexagonal, the unit cell parameters are a= 0.5034 nm and c=1.375 nm, but in rhombohedral system, unit cell parameters are a=0.5427 nm and $\alpha$ = 55.3°. Iron (III) ions occupy two thirds of the sites, oxygen ions are accumulated in the [001] direction and there is a vacant site in (001) plane [23]. In Fig. 1.3, a segment of bulk hematite structure is shown.

Hematite is an antiferromagnetic material. Due to the moments of two sublattices in the basal plane direction which do not cancel each other, there is a small magnetic

moment in the mentioned plane. The preparation conditions of the hematite samples affect their magnetic properties. A phase transition in hematite happens at 263K, which is called Morin transition, antiferromagnetic phase turns to a weak ferromagnetic phase at mentioned temperature. At low temperatures, the hematite spins lie in the rhombohedral [111] direction, while they lie in the basal (111) plane in a canted position at high temperatures. The Morin transition temperature is affected by the crystallite size of hematite. Polycrystalline and single hematite display Morin transition. This temperature decreases with reduction in particle size and when the size is smaller than 20nm there will be no such transition in the sample [24-28].

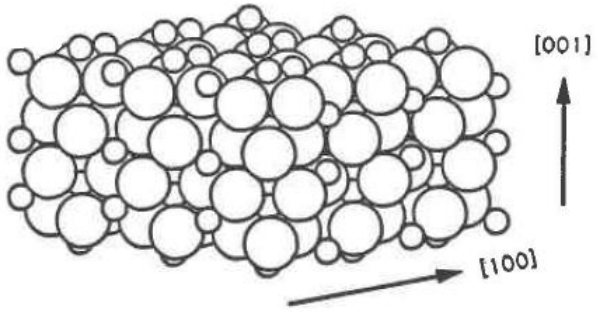


Figure 1. 3 A model of a part of the bulk hematite structure. Crystallographic directions are shown. Oxygen layers alternate with Fe layers in the [001] direction. Adapted from Ref. [29].

Maghemite, $\gamma$-$Fe_2O_3$ is the second most polymorph of iron (III) oxide which occurs in nature. It has an inverse spinel with a cubic unit cell, a=8.351 Å and $P4_132$ space group which is isostructural with magnetite. All of the irons in maghemite are in the trivalent state. In Fig. 1.4 the structure of maghemite is shown. In each unit cell of maghemite, there are 21 1/3 iron (III) ions and 32 $O^{-2}$ ions, cations are in tetrahedral and octahedral positions, 2 1/3 of the unit cell is devoted to vacancies (□) which are in octahedral positions. The vacancy ordering gives rise to the superstructure form of synthetic maghemite which is in relation with crystallite size [30]. As a result of this construction the stoichiometry of maghemite is the general formula of

$Fe_8[Fe_{13.3\square 2.67}]O_{32}$. Maghemite can have various symmetries depending on the degree of vacancy ordering. Completely ordered maghemite possesses a tetragonal symmetries, otherwise it is cubic [31, 32]. At room temperature, maghemite is ferrimagnetic, while if the size of particles decreases to the about 10nm then maghemite will display superparamagnetic property. Furthermore, it transforms to hematite when temperature changes in a specific range, so its thermal instability disables the Curie temperature, $T_c$, determination of magnetic transition for maghemite. The range of the Curie temperature is estimated to be between 820 K to 986 K [30]. Generally, the magnetic structure of maghemite includes two sublattices which each of them correspond to the $Fe^{3+}$ particles that are located on octahedral and tetrahedral sites. Below the temperature $T_c$, the spin direction within each sublattice is parallel, while those of two sublattices are antiparallel. The spinel structure with two sublattices and number of iron ions in each of sublattices and decompensation between them causes ferrimagnetism. Thus, maghemite is a typical representative of ferrimagnetic materials which give high susceptibilities to all samples that it is contained in. Internal structure disorder, interparticle separation, size and agglomeration affect the magnetic properties of maghemite [30]. The ultrasmall maghemite particles display supermagnetism which makes maghemite to be one of the most reached materials for making supermagnetism theory relaxation.

Maghemite nanoparticles are widely used in biomedical applications like DNA purification, drug targeting, hyperthermia, molecular biology and magnetic resonance imaging and also in industrial applications like catalysis and magnetic refrigeration. Beta phase iron oxide, β- $Fe_2O_3$, is a body-centered cubic bixbyite structure with Ia3 space group and two nonequivalent octahedral sites of Fe (III) ions in the crystal lattice which is shown in Fig. 1.5. It is magnetically disordered at room temperature and also it is thermally metastable converting to alpha phase at above 500 °C. It can be obtained by thermal decomposition of iron (III) sulfate or reduction of hematite by carbon or also by dehydroxylation of β-FeOOH at 170°C under high vacuum. The temperature that beta phase presents antiferromagnetic behavior, i.e. the Neel temperature, is in the range 100-119 K which is observed in various researches [17].

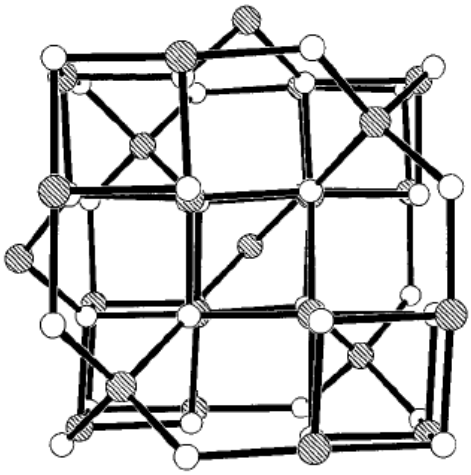

Figure 1. 4 Crystal packing in the structure of γ-$Fe_2O_3$, the view onto (100). The circles which are shaded represents Fe atoms and white ones represent O atoms. Adapted from Ref. [30]

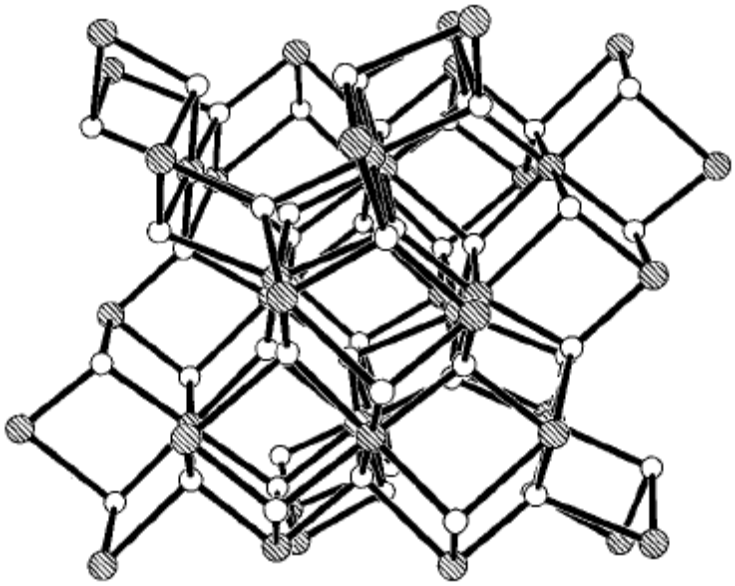

Figure 1. 5 Crystal packing in the structure of β-$Fe_2O_3$, the view onto (110). Fe, shaded circles represent Fe atoms and white ones show O atoms. Adapted from Ref. [23].

The other phase of iron oxide is epsilon iron oxide, ε- $Fe_2O_3$, which is among the rare compounds like beta phase. Orthorhombic ε- $Fe_2O_3$ structure with $Pna2_1$ space group displays many intermediate structural features between α-$Fe_2O_3$ phase and γ-$Fe_2O_3$. This structure is isomorphous with $GaFeO_3$ and $AlFeO_3$. Three nonequivalent anion and also four cation positions exist in this structure. It has been reported that ε- $Fe_2O_3$ transforms to α-$Fe_2O_3$ under heating at 500-750°C which depends on the preparation method. Besides, at temperature 210°C, i.e. Curie temperature, ferrimagnetic properties have been investigated [33-35].

Magnetite, $Fe_3O_4$, is one of the most common iron oxide materials with inverse spinel structure with 32 $O^{2-}$ ions in the face centered cubic unit cell. Its structure is completely different from other iron oxides. Two kinds of iron ions divalent $Fe^{2+}$ and trivalent $Fe^{3+}$, exist in its formula. The positions of these cations is different, eight tetrahedral sites are distributed between $Fe^{2+}$ and $Fe^{3+}$ ions, the trivalent ions are located both in tetrahedral and octahedral positions .

Magnetite shows high magnetization and is a ferrimagnet. Below the Curie temperature (850 K), in the tetrahedral and octahedral positions, the magnetic moments are antiparallel so the material will display ferrimagnetic properties. Around 125 K, its electrical conductivity reduces and there is a semiconductor-insulator phase transition in magnetite. When the orientation of electrons changes to one direction in magnetite, it will behave like a metal, while the electrons aligned in the opposite direction it will behave like an insulator. This property of magnetite is the half-metallicity behavior and due to this property this material is very useful for tunneling magnetoresistance devices [31].

### 1.4. Magnetic Properties

Novel breakthroughs in materials mostly play a great role on the progress of technology and as a result can even influence economies and societies (e.g. the Bronze to Iron Age). Considering the effect of size of materials on their properties, we

conclude that novel nanostructure materials have provided hope for the detection of new phenomena and effects in order to developing novel nanotechnology which have gained great attention and relevance due to great variety of feasible and real applications in multidisciplinary fields like industry, medicine, pharmacy, physics, chemistry and many other fields. Recent improvements in magnetic materials have revolutionized the technology. Magnetic iron oxide nanoparticles have attracted great attention and gained acceptance in various fields of application of nanomaterials by virtue of their particular properties specifically magnetic properties.

Magnetic properties of nanomaterials and nanoparticles are characterized by many factors like magnetic moment of the electrons, permeability and magnetic susceptibility for solids and nanomaterials, and for nanoparticles, chemical composition, the particle size and shape, the type of the crystal lattice, the morphology and different interactions of particles. Any changes in each of these parameters, shape, structure, size and composition, will affect the magnetic properties [36, 37].

Magnetic properties of the materials are determined by the magnetic moments of each of electrons. Orbital and spin motions of each electron influence the macroscopic magnetic properties of materials. Orbital motion or orbital angular momenta is described by the electron spin that is originated along the orbit around the atoms nucleus. Spin moment is defined with the electron spin around its axis [38]. In Fig. 1.6 and 1.7 orbital and spin magnetic moments are presented.

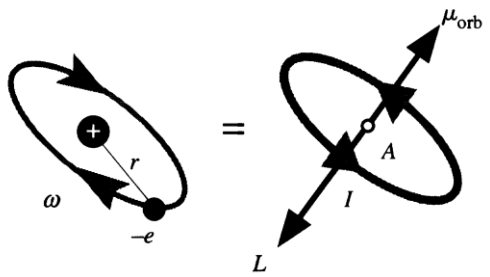


Figure 1. 6 An orbiting electron which is equivalent to magnetic dipole moment. Adapted from Ref. [39].

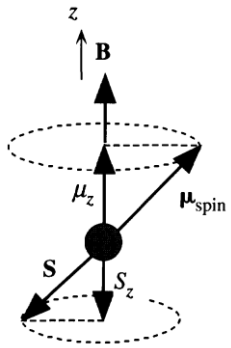


Figure 1. 7 Spin magnetic moment precesses about an external magnetic field around z and has a value $\mu_z$ along z. Adapted from Ref. [39].

When a material is placed in a magnetic field of strength $H$, the intensity of magnetization $M$ is related to $H$ by the magnetic susceptibility κ of the material,

$$M = \kappa H \tag{1.1}$$

The magnetization $M$ is defined as the magnetic moment of the sample per unit volume

$$M = \frac{m}{V} \tag{1.2}$$

$M$ is a property of the material, and depends on the individual magnetic moments of the constituent ions, atoms, or molecules, and on how these dipole moments interact with each other.

The density or flux of the lines of force in a material placed in a magnetic field is named the magnetic induction, $B$, which are related together as follows,

$$B = \mu(H + M) \tag{1.3}$$

where μ is the magnetic permeability, and is defined as the tendency of the magnetic force lines to pass through a medium relative to their tendency to pass thorough a vacuum. Magnetic permeability is defined as,

$$\mu = \mu_0(1+\kappa) \tag{1.4}$$

where $\mu_0$ is the vacuum permeability. The parameter μ is important for recognizing paramagnetic and diamagnetic materials from each other.

The magnetic moment, m, is a parameter that quantifies the magnetic properties of a material but it is not measured directly and can be obtained from the measured molar susceptibility as the following relation,

$$\chi = \mu_0 \frac{Nm^2}{3KT} \tag{1.5}$$

where K is the Boltzmann constant and N is the Avogadro number. The Bohr magneton is the fundamental magnetic moment and is defined as,

$$\beta = \frac{eh}{4\pi m_e c} = 9.27 \times 10^{-24}\ \text{Am}^2 \tag{1.6}$$

where $m_e$ is mass of electron and e is electron charge. Considering the Bohr magneton, the expression (1.5) will reduce to

$$m = 2.83\sqrt{\chi T} \tag{1.7}$$

The magnetic moment usually is expressed in Bohr magnetons. The interaction between orbital moment and the spin moment of electrons, $\mu_s$, generates the magnetic moment. However the contribution of the orbital moment is very small in comparison with spin moment. The magnitude of overall spin moment is defined by considering the number of unpaired electrons of each atom,

$$\mu_s = g \sqrt{S(S+1)} \tag{1.8}$$

where $S$ is the sum of the spin quantum numbers, which is equal to the $\pm\frac{1}{2}$ for each of electrons and $g$ is gyromagnetic ratio, for example $g$ =2 for free electron [30, 39,40].

Magnetic materials have magnetic moments which are represented by the electric dipoles. As seen in Fig. 1.8, magnetic dipole moments are shown as an arrow, which can be thought of as a magnet with north and south poles. Those domains that have different directions are separated by domains walls. Magnetic orientation of each domain is different. Summation of all domain vectors will determine the magnitude of magnetization, for instance, in non-magnetic materials this summation is zero [41].

In the presence of an external field, all the atomic dipoles align themselves with the applied external field. The magnetization will not reduce to zero, when the magnetic field is eliminated or reduces to zero; this means the material is magnetized. In fact ferromagnets and ferrimagnets keep displaying interesting behavior when the magnetic field is reduced to zero and then reversed in direction. The graph of B or M versus H which is traced out is called hysteresis loop. Schematic hysteresis loop of a ferromagnetic material is displayed in Fig. 1.9. As seen in this figure the maximum possible magnetization of a ferromagnetic material is obtained at saturation point ($B_s$). All of the magnetic dipoles are aligned in the same direction of external field at the saturation point [40]. Two important points are seen in the hysteresis loop (Fig. 1.10), coercivity and retentivity. The first one is the point of the reverse field which is needed for lowering the induction to zero, and the second one is the measure of the residual flux density which is corresponds to the saturation induction of a magnetic material, in fact, this point displays the material's ability to retain some amount of residual magnetic field when the magnetizing force is removed after saturation.

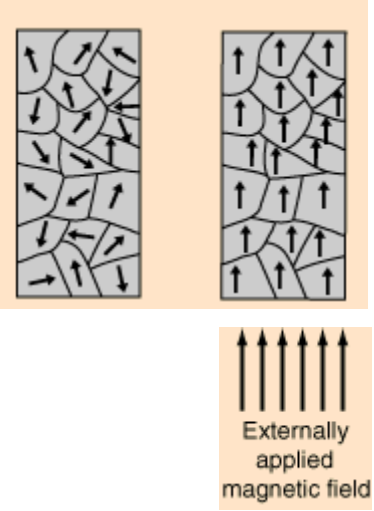


Figure 1. 8 Representation of magnetic dipoles, before and after applying external magnetic field. Adapted from Ref. [41].

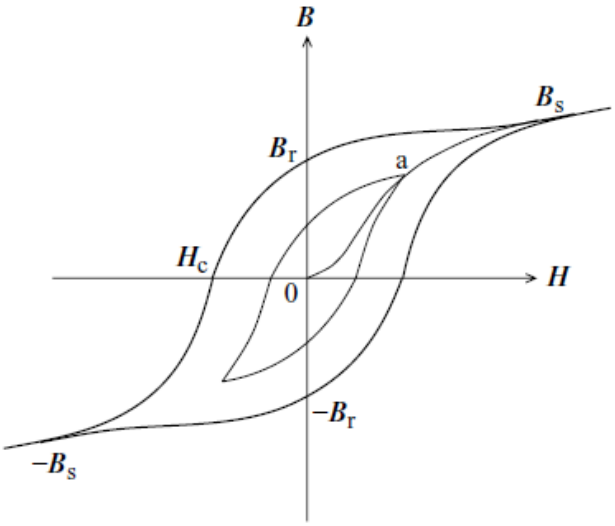


Figure 1. 9 A typical hysteresis loop for a ferro-or ferrimagnet. Adapted from Ref. [40].

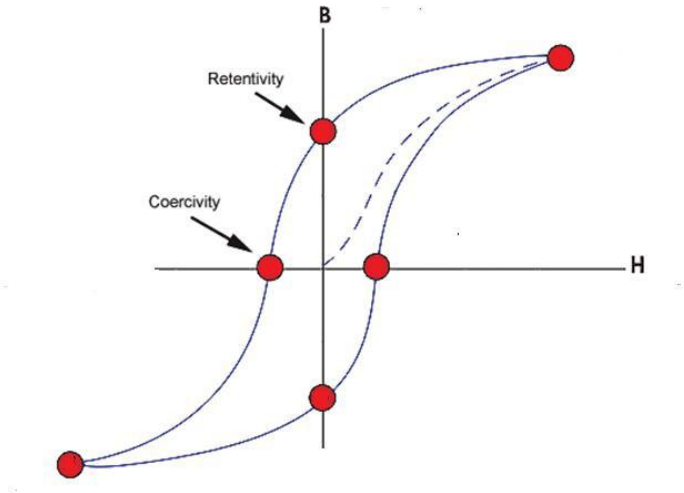


Figure 1. 10 Coercivity and retentivity points of a typical hysteresis loop. Adapted from Ref. [40].

### 1.4.1. Classification of Magnetic Materials

#### 1.4.1.1. Diamagnetism

As mentioned above, the electron spin and orbital angular momentum are two contributions of atoms magnetic moments. The other factor that affects magnetic moment of atoms is the change in orbital motion of electrons under an external magnetic field. Any change in orbital motion when an external field applied is known as diamagnetic effect, and it happens in all atoms, even in those atoms with filled electron shells. Since diamagnetism is a weak phenomenon so only those atoms that have no net magnetic moment are classified as diamagnetic. In other materials the diamagnetism is dominated by much stronger interactions like paramagnetism or ferromagnetism. Diamagnetic materials do not have a stable magnetic moment, thus they do not have wide range applications like other magnetic materials. Magnetic susceptibility of diamagnetic material is negative and that is, the magnetization

decreases as the magnetic field is increased. The diamagnetic susceptibility is given by the following relation,

$$\chi = -\frac{NZe^2}{6m_e c^2} \langle r^2 \rangle_{av} \tag{1.9}$$

This relation is dimensionless and there is no explicit temperature dependence. In eq. (1.9), N is the number of atoms per unit volume, Z is the atomic number, c is the speed of light, $m_e$ is the mass of electron and r is orbital radius [40]. The magnitude of diamagnetism susceptibility is very small; about $10^{-6}$ per unit volume. A recent application of diamagnetism is the magnetic-field-induced alignment of liquid crystals. If a strong magnetic field is applied, alignment of liquid crystals can be induced in which the diamagnetic susceptibility is anisotropic. Inasmuch as a diamagnetic material tries to exclude magnetic flux, the liquid crystal will tune itself such that the axis that possesses most negative diamagnetic susceptibility will be perpendicular to the magnetic field. The diamagnetic susceptibility is adjustable in liquid crystals by controlling the amount of macroscopic alignment [40, 42, 43]. Some examples of diamagnetic materials are organic materials e.g. many polymers, some ionic solids like alkalihalides, some metals such as Cu and Ag, and materials with closed shells atoms. Superconductors are among perfect diamagnetic materials with $\chi$=-1 [39]. Iron oxides illustrate additional types of magnetism. When a diamagnetic material is placed in an external magnetic field, the applied field and the magnetization vector in the material will be in opposite directions, in fact the diamagnetic material tries to expel the applied magnetic field from material; this will interpret the cause of negative value of susceptibility. When the external applied magnetic field is nonuniform, the magnetization of the material will be in the opposite direction of B then the material experiences a net force toward smaller fields as it is shown in Fig. 1.11. This cause the diamagnetic material stays away from a permanent magnet.

### 1.4.1.2. Paramagnetism

Paramagnetism occurs in materials which possess net magnetic moment, i.e. magnetic moment of ionic, atomic and molecular species are not zero. These magnetic moments are coupled to each other weakly and thus the thermal energy makes casual alignment of the magnetic moments. In other words, in paramagnetic materials, each atom possesses a permanent dipole moment by virtue of incomplete cancellation of spin of

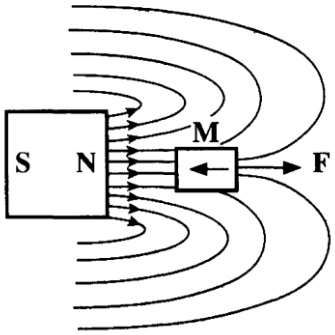


Figure 1. 11 A diamagnetic material which is placed in a nonuniform magnetic field. Adapted from Ref. [39].

electrons or orbital magnetic moments, but these magnetic moments are random. Thus application of a magnetic field causes the moments to align parallel to the field since the atomic dipoles are free to rotate, but only a small fraction of moments are diverted into the field direction, so paramagnetism occurs when they preferably align in the presence of an external field, this is displayed in Fig. 1.12b . The magnetic susceptibility is small and positive between $10^{-3}$ to $10^{-5}$, furthermore; its value depends on temperature. Its behavior is explained by Curie- Weiss law,

$$\chi_M = \frac{C_M}{T - T_C} \tag{1.10}$$

where $T_C$ is Curie temperature , $C_M$ is Curie constant and T is temperature. According to relation (1.10), temperature increases as $\chi_M$ decreases. The reason for this decrease is in the opposition of stronger thermal vibrations to the increment of alignment of magnetic moments when temperature rises.

Since both diamagnetic and paramagnetic materials, only in the presence of an external field, expose magnetization; so they are assumed to be nonmagnetic. The flux density $B$ within both of them is approximately identical as it would be in a vacuum. In figure 1.12 (a) and 1.12 (b), a comparison of diamagnetic and paramagnetic materials in the external magnetic field are presented [41].

#### 1.4.1.3 Ferromagnetism

Ferromagnetic materials such as transition metals cobalt, iron and nickel possess large and permanent magnetization even in the absence of an external magnetic field. Electron spin and orbital moments, both contribute to this behavior, i.e., the parallel alignment of electron spins and uncancelled electron spins and small contribution of orbital magnetic moment are responsible for this property. Even in the absence of external field, coupling interactions produce net spin magnetic moments of neighbor atoms to align with each other in a ferromagnetic materials, it is illustrated in Fig. 1.13 schematically. The source of these forces is not entirely known, but it is predicted to happen because of the electronic structure of metals. The regions in the crystal which these mutual spin alignments exist are called domains. These kind of materials possess overall net magnetic moment, positive and large susceptibility ($10^{-2}$ to $10^{6}$) and also large magnetic permeability. Increasing temperature will reduce the ordered arrangment of spins. This is due to thermal fluctuations of the singular magnetic moments. Temperature increasing also decreases susceptibility. This temperature dependence does not obey the Curie- Weiss law.

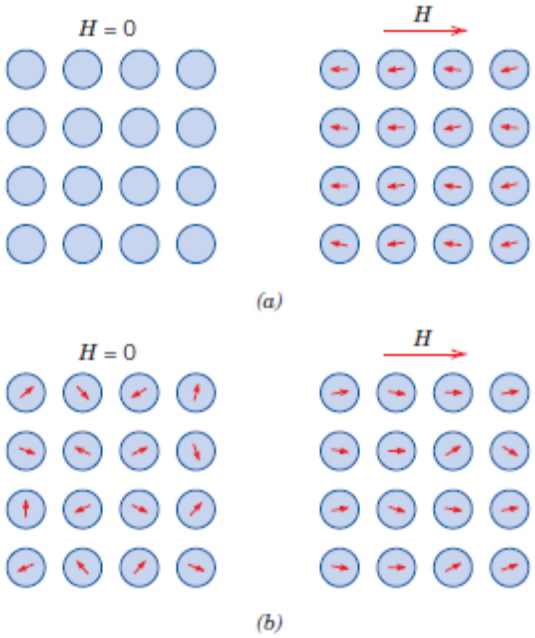


Figure 1. 12 (a) The atomic dipole configuration for a diamagnetic material in the presence and absence of an external magnetic field. Without an external field there is no dipoles, but with a magnetic field, dipoles are induced that are aligned in the opposite direction to the external field. (b) Atomic dipole configuration of a paramagnetic material in the presence and absence of an external magnetic field. Adapted from Ref. [41].

As mentioned before, there is a transition temperature termed the Curie temperature ($T_C$) which is specific for ferromagnetic and ferrimagnetic materials [30,41,44]. Below this temperature material is ferromagnetic, above that it will behave like paramagnetic materials (See Fig 1.14). In a ferromagnetic material, when all the magnetic dipoles are mutually aligned with the applied external field, the maximum magnetization or saturation magnetization, $M_s$, occurs. The corresponding flux density is called saturation flux density $B_s$. Both  Product of number of atoms and the net magnetic moment of each of atoms will produce the saturation magnetization.

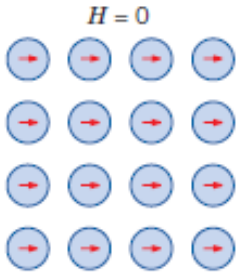


Figure 1. 13 Schematic illustration of mutual alignment of atomic dipoles in a ferromagnetic material. Adapted from Ref. [41].

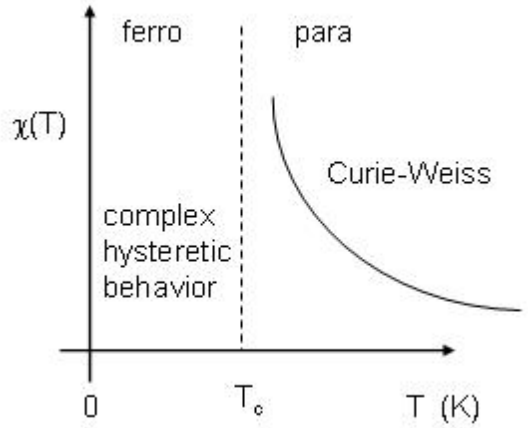


Figure 1. 14 Curie-Weiss Law for ferromagnetism. Adapted from Ref. [44].

The graph of B versus H, or hysteresis loop for ferri and ferromagnetic materials have been shown in Fig. 1.9 schematically.

#### 1.4.1.4 Antiferromagnetism

The phenomenon of magnetic moment coupling between neighbor atoms in antiparallel alignment or electron spins of equal magnetic moments alignment in an

antiparallel (opposite) direction in a material is termed antiferromagnetism. These materials can be thought as containing two identical and interpenetrating sublattices of magnetic ions, as shown in Fig. 1.15.

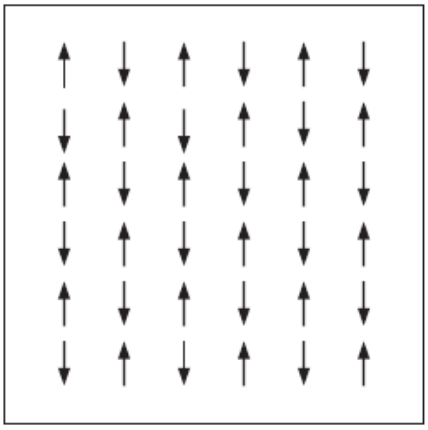

Figure 1. 15 Ordering of magnetic ions in an antiferromagnetic lattice. Adapted from Ref. [41].

Below the specific temperature called the Neel temperature, one set of magnetic ions is spontaneously magnetized while the other set is magnetized in the opposite direction but the same amount. As a consequence, antiferromagnetic materials have no net spontaneous magnetization and in the presence of external field, their answer is similar to paramagnetic materials at a fixed temperature. Such materials have positive permeability and small positive susceptibility which is temperature dependence above the Neel temperature, i.e. enhancing temperature will result in rise in susceptibility, since the antiparallel ordering is disrupted, while below the Neel temperature it reduces when temperature decreases as it is displayed in Fig. 1.16 [30,40]. Above the Neel temperature the antiferromagnetic material changes to paramagnetic material.

### 1.4.1.5. Ferrimagnetism

Ferrimagnetic materials exhibit permanent magnetization which from macroscopic view, the materials are similar to ferromagnets below the Curie temperature, the only difference lies in the origin of the net magnetic moments. But in Fig. 1.17, the form of typical ferrimagnetic magnetization curve is completely different from the ferromagnetic curve.

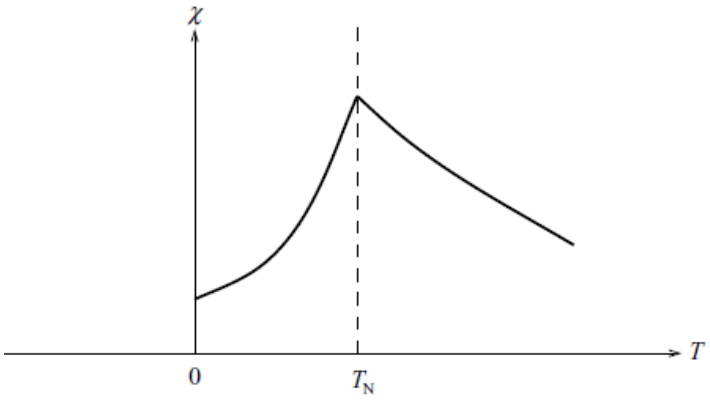


Figure 1. 16 Typical temperature dependence of susceptibility in an antiferromagnet. Adapted from Ref. [40].

In addition, these materials just like antiferromagnetic ones include some interpenetrating sublattices, within which, the spin alignments are antiparallel. As it is illustrated in Fig. 1.18, the values of spin moments are not equal so these kinds of materials possess a net magnetic moment even in the absence of external magnetic field. As it is clear in Fig 1.18, spin directions of A atoms are the same, but spin of B atoms are aligned in opposite direction. Since the magnetic moments A atoms are greater than B ones, so the net magnetic moment is nonzero. Ferrimagnetic materials like ceramics are typically nonconducting, so they are among good candidates for

high-frequency electronics applications. Cubic ferrites display ferrimagnetism. These materials are indicated by the chemical formula $MFe_2O_4$, M implies any metallic element. The prototype ferrite is $Fe_3O_4$. There is a net spin magnetic moment for both $Fe^{2+}$ and $Fe^{3+}$ ions, and the $O^{2-}$ ions are neutral magnetically. Between Fe atoms, there are antiparallel spin coupling interactions which is identical to antiferromagnetism. However, the net ferrimagnetic moment occurs from the incomplete cancellation of spin moments.

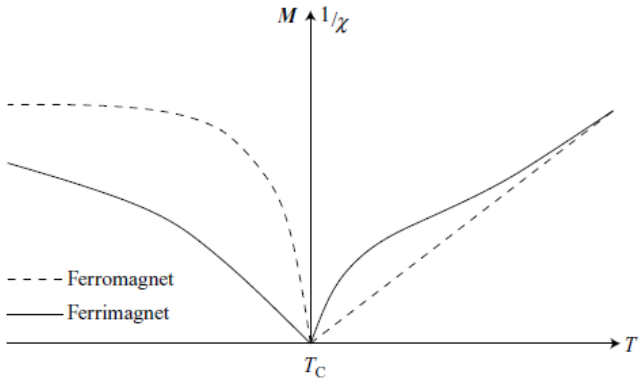


Figure 1. 17 Comparison of magnetization and inverse susceptibility in typical ferri- and ferromagnets. Adapted from Ref. [40].

### 1.4.2. Magnetic Behavior of Iron Oxides

In a solid, the interaction between iron atoms cause parallel or antiparallel spins alignments. In iron oxides each iron atom is surrounded by $O^{2-}$ ions, thus the exchange happens via the intervening ligand, i.e. there will be interactions between unpaired electrons in the $e_g$ orbitals of $Fe^{3+}$ ions and electrons in the p orbital of $O^{2-}$ ions. In this situation coupling of electrons of cation and ligand will occur since they are close enough together, thus a chain coupling effect in the crystal is accomplished.

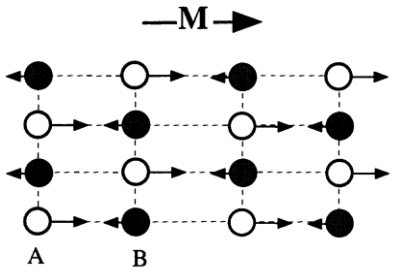


Figure 1. 18 Magnetic ordering in the ferromagnetic crystal. The A atoms possess aligned spins in on direction, and the spins of B atoms are aligned in opposite direction. Since the magnetic moment of A and B atoms are not equal so the net magnetization, M, is not zero in the crystal. Adapted from Ref. [39].

The exchange constants depend on the Fe-O bond length and bond angles. In Table 1.1 the different types of exchange reactions in iron oxides and dependence of their interactions on the bond length and bond angles are compared. For instance, for Fe2+, when the bond angles are 120-180, the exchange interactions are strong [45].

Table 1.1 Exchange interactions in iron oxides. Adapted from Ref. [45].

| **Ion pair** | **Fe-O-Fe bond angle** | **Type of interaction** |
|---|---|---|
| **$Fe^{3+}$ - $Fe^{3+}$** | 90° | Weak antiferromagnetic |
| | 120° | Strong antiferromagnetic |
| **$Fe^{2+}$ - $Fe^{2+}$** | 90° | Weak antiferromagnetic |
| | 120-180° | Strong antiferromagnetic |

Following the scenario of ferrites, we consider cubic ferrites whose crystal structure is inverse spinel. There are two types of positions for iron cations. For one type, the

coordination number is 4 in tetrahedral coordination and each of iron ions is surrounded by four oxygen neighbors. The coordination number is 6 for other iron cation which is placed at octahedral coordination. In this structure half of the $Fe^{3+}$ ions are placed in octahedral and half of the others in tetrahedral positions, while all $Fe^{2+}$ ions are situated in octahedral positions. The arrangement of the spin moments of iron ions is very important; the $Fe^{3+}$ ions in the octahedral positions are aligned parallel to each other, provided they are aligned in antiparallel directions for the tetrahedral positions. In the Fig 1.19 and Table 1.2 the various configuration of spin moments of iron cations are shown [30, 41, 46].

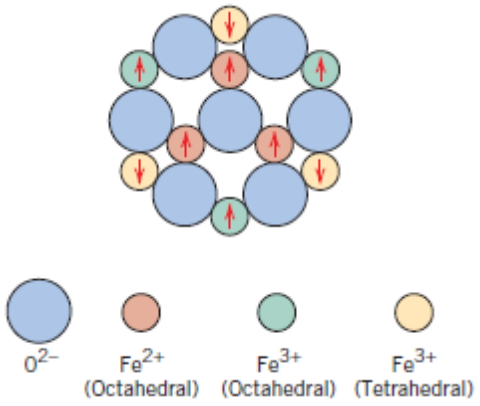


Figure 1. 19 Schematic diagram of the spin magnetic moments configuration for $Fe^{2+}$ and $Fe^{3+}$ ions in $Fe_3O_4$. Adapted from Ref. [46].

The spin moments of all $Fe^{3+}$ ions cancel each other, so they will have no contribution to the net magnetization in the solid. The summation of the parallel moments of $Fe^{2+}$ ions which are aligned in the same direction will not be zero, as a result the total moment of $Fe^{2+}$ ions have main contribution in net magnetization of solid.

Table 1.2 The distribution of spin magnetic moments for $Fe^{2+}$ and $Fe^{3+}$ ions in a unit cell $Fe_3O_4$. Adapted from Ref. [41].

| *Cation* | *Octahedral Lattice Site* | *Tetrahedral Lattice Site* | *Net Magnetic Moment* |
|---|---|---|---|
| $Fe^{3+}$ | ↑ ↑ ↑ ↑<br>↑ ↑ ↑ ↑ | ↓ ↓ ↓ ↓<br>↓ ↓ ↓ ↓ | Complete cancellation |
| $Fe^{2+}$ | ↑ ↑ ↑ ↑<br>↑ ↑ ↑ ↑ | — | ↑ ↑ ↑ ↑<br>↑ ↑ ↑ ↑ |

## 1.5. Graphyne

The atoms of the chemical element carbon can be bonded together many different ways. These different ways of bonding of atoms are known as allotropes of this element. Diamond, graphite, graphene and graphyne are examples of carbon allotropes.

They all have very different chemical and physical properties. Among all carbon allotropes, only two exist freely in nature: diamond and graphite. The others are non-natural and they have been predicted or have been already synthesized in the laboratory [47].

Figure 1.20 (a) and (b) show a schematic view of carbon atom and the energy bands of its atomic orbitals [48]. The "2s" and "2p" orbitals have very similar energies, -19.20 eV and -11.79 eV. This allows electrons from different carbon atoms to overlap and pair with each other to form hybridized atomic orbitals, for example, sp, $sp^2$ and $sp^3$ hybrid orbitals like graphynes (GYs) and Graphdiynes (GDYs).

Graphyne is a two dimensional allotrope of carbon predicted by Baughman in 1987 [49]. It is a one atom thick layer of carbon network and it has mixed hybridization, i.e.

it has carbon atoms only in sp and $sp^2$ hybridization state. The sp hybrid orbital is a mixture of one "2s" and one "2p" orbitals and in $sp^2$ hybridization the 2s orbital is mixed with only two of the three available 2p orbitals. Graphyne has a structure similar to the graphene but instead of only $sp^2$ there are also sp carbon atoms.

As it is clear in Fig 1.21, the hexagonal rings in graphyne which are formed by $sp^2$ hybridized carbon atoms are spliced by acetylenic linkages $(-C \equiv C-)$ instead of some $= C = C =$ bonds, encompassing pores that are larger than densely packed honeycomb lattice in graphene [50,51].

Whereas these carbon ($sp+sp^2$) sheets possess high level π-conjunctions and acetylenic bonds which associated with sp-hybridized atoms, represent some uncommon electronic properties, high temperature stability, nonlinear optical susceptibility, conductivity and mechanical properties similar to graphite. Duo to these peculiar properties, these kinds of materials are considered as promising materials for utilization in next generation of nanoelectronics, energy storage applications, and hydrogen storage. Hence, tuning of these materials is of great importance for future applications. There are many different types of graphyne. For example, the graphyne allotropes α , β and γ graphynes, have the same hexagonal symmetry as graphene. As a consequence they have very similar electronic and vibrational properties to graphene.

Figure 1.21 shows a schematic presentation of the structure of graphyne, α- graphyne, β- graphyne and γ-graphyne. On the same figure one can see that the hexagonal carbon rings in graphyne are joined by the so called acetylenic linkage. Experimentally graphyne sheets have not been synthesized yet, but the other family member, graphdiyne, with diacetylenic linkages between hexagons has been synthesized on copper surface [47,53].

This thesis is divided into five chapters. In the second chapter, the theoretical methods, Molecular dynamics and density functional theories, which are used in the investigations of the studied systems, have been explained. In the third chapter, the results of the molecular dynamics simulation for the studies systems (iron oxide nanorod and nanoparticles) will be presented. In the chapter four, the results of

applying density functional theory for the iron oxide clusters and Graphyne nanotubes will be given. And the last chapter presents a brief conclusion and summary of all mentioned results.

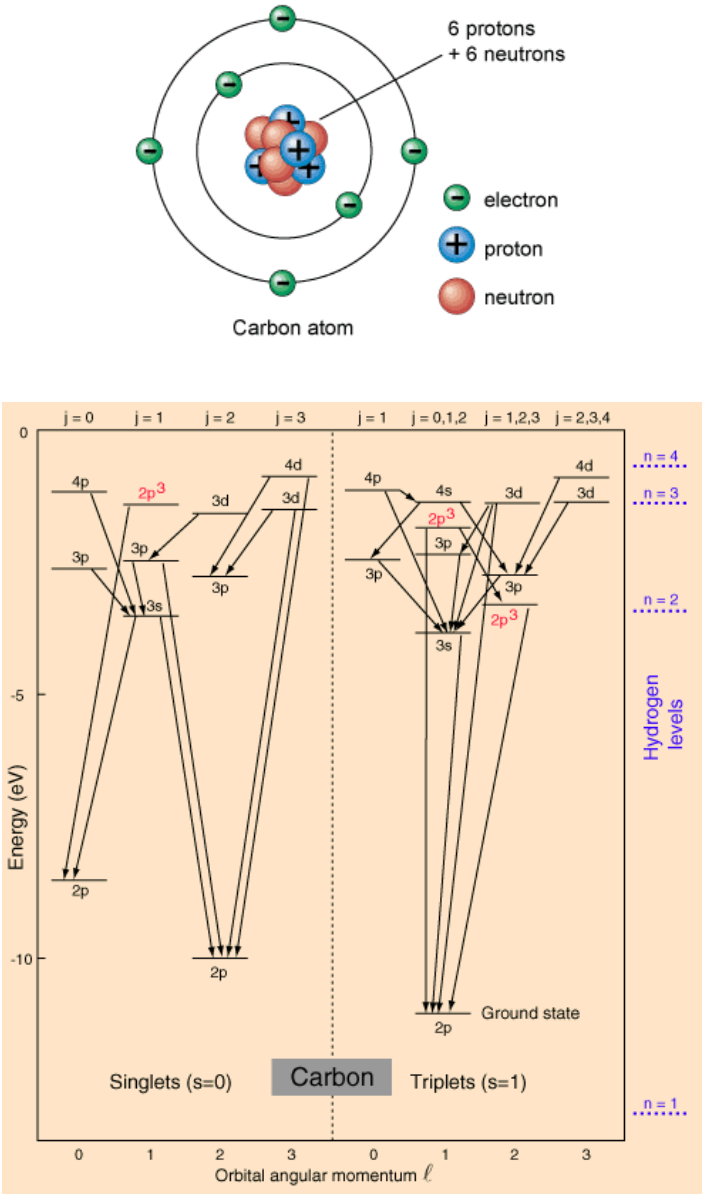


Figure 1.20 Schematic diagram of Carbon (a), Carbon energy levels (b). Adapted from Ref. [48]

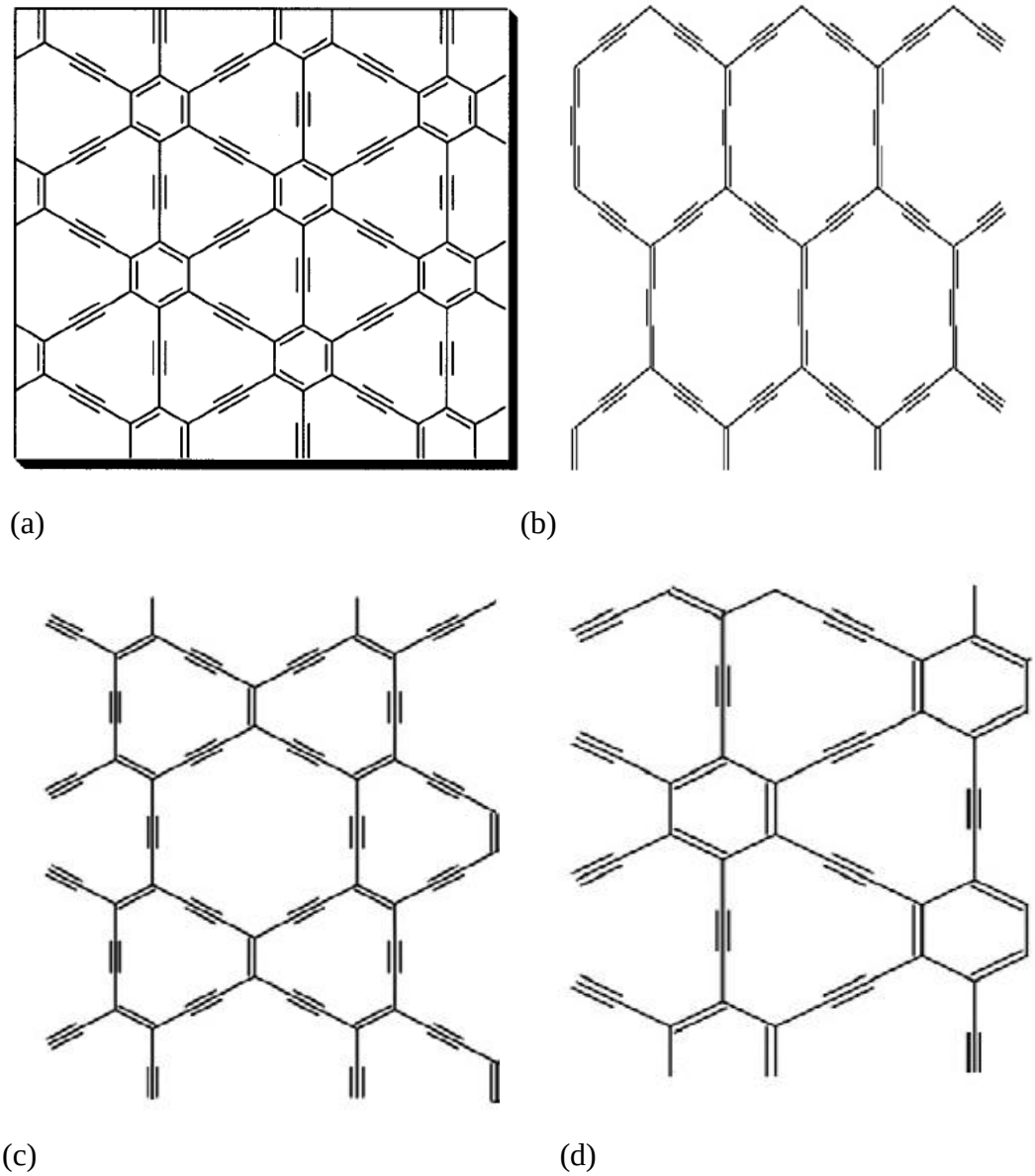


Figure 1.21 Schematic presentations of graphyne (a) α-graphyne (b), β-graphyne (c) and γ-graphyne (d). Adapted from Ref. [49,52]

# CHAPTER 2

# THEORETICAL METHODS

## 2.1. Molecular Dynamics Method

Molecular Dynamics (MD) simulation method is designed to explain atomic motions as a function of time. The goal of MD simulation is to predict the macroscopic behavior of the system under study which is consequence of microscopic interactions. Hence, a molecular dynamic simulation can be employed for assessing material behavior which occurs at lower length scales that cannot be extrapolated from experimental data.

Molecular dynamics method takes Newton's equations of motion as a basis for the atoms which interact by applying forces on each other. Based on the interaction model and with the help of these fundamental laws, the MD simulation determines the atoms trajectories, i.e. computes future positions of atoms or molecules of studied system; in a simple term, MD is a method of particle tracking. Besides, the forces which act on atoms and also energies of particles in the system will be specified [54-56]. In MD simulation the system is propagated through the phase space.

Accordingly, a molecular dynamics simulation comprises the following parts: at first, one should find a model which explains the interaction of the particles or atoms constituting the system. This interaction is determined by the interatomic potential energy functions (PEFs). Using the suitable interatomic potential, appropriate initial and boundary conditions, the numerical integration of the atoms equation of motion, i.e. Newton's equations is performed. In MD simulations, the approach for solving the Newton's equations of motion is equivalent to that of the macroworld, using the

calculated forces, we can find acceleration. The last step is extracting proper and good results from the raw atomic trajectory information.

### 2.1.1. Canonical Ensemble

Considering a simulated system which includes large number ($10^2$ - $10^8$) of atoms, we see that so many microstates which correspond to the each of macrostates exist. However, for predicting macroscopic quantities and observables and also noticing the degrees of freedom of each single atom, it is needed to solve several differential equations which are time-consuming and long calculations. For easing this complexity, ensemble theory is applied. The collection of all microstates which define and replicate the characteristic of the whole system called an ensemble. Using ensembles, we can reduce the information which is needed to describe the system and finding an observable by applying some restrictions on the observables of the system under study.

For running the dynamics simulation in the system, a statistical ensemble should be selected. Generally, there are three main ensembles:

- Microcanonical ensemble (NVE); which number of atoms, volume and energy are constant.
- Canonical ensemble (NVT); which describes a system with constant number of atoms and constant volume and temperature.
- Grand canonical ensemble (μVT); which the number of atoms in the system is not fixed, energy and number of particles can exchange which results in fixed chemical potential and temperature.

In this study for investigating the stability of nanorods at different temperatures, the system has been kept at thermal equilibrium with the surroundings. Number of atoms N of the system are isolated from the surroundings i.e. are constant. They are contained at constant volume V and interact with each other through the potential energy function (PEF) or U. The canonical ensemble (NVT) satisfies these conditions

and we apply it in our simulation. A typical MD simulation on the basis of NVT ensemble consists of the following steps: initialization that is obtaining the initial coordinates, $r_i$, and initial velocities, $v_i$, using Maxwell-Boltzmann distribution. Besides, in this step, all simulation parameters such as cut-off distance, potential function parameters, time-step and equilibration steps are set. In equilibration and production steps, which are essentially the same, except that, in production step, properties of concern are found. The forces are calculated using potential energy function, then solving MD equations of motions, the time evolution of coordinates, velocities and kinetic energies are obtained. All procedures of calculation are repeated till the MD steps are expired. Reliability of simulation results depends on the accuracy of potential energy function which can be precisely obtained from calculations which are based on quantum mechanics. Suppose the potential energy function for N number of atoms is written as

$$U\ R\ = U(r_1, r_2, \dots, r_N) \tag{2.1}$$

The energy of specific phase space state of a system is described through the Hamiltonian

$$H = \frac{1}{2}\ \ _i \frac{1}{m} p_i^2 + \ \ _{i \neq j \neq k} U(r_{i,j,k}) \tag{2.2}$$

where the first term on the right hand side is the kinetic energy and the second term is potential energy which is related to the interaction between particles. The phase space state is the spatial orientation of the molecules ($r_{i,j,k}$) and the momentum ($p_i$). Owing to the constraint on the internal potential and temperature, the phase space is not completely independent. Using statistical mechanics during MD simulation will establish the possibility of formulation of the solutions of differential equations of motions and so finding the macroscopic and microscopic properties. The forces which act on atoms are calculated as follows:

$$m_i \frac{d^2 r_i}{dt^2} = F_i = -\nabla_i U \qquad \text{i=1,2, …, N} \qquad (2.3)$$

where $m_i, r_i$ and $F_i$ are the mass, position and force vector of atom i, respectively. This classical form of the motion equation is a true approximation of the Schrödinger equation in the case that the atoms are not too small and the temperature of system is comparable with the gap of quantum energy levels associated with the dynamics. In fact, two approximations govern the classical motion equations for describing the atoms. The first one is Born-Oppenheimer approximation [57] which is based on the postulate that the electronic state couples to nuclei motion adiabatically. The second approximation is that the motion of nucleus is far removed from the Heisenberg uncertainty lower bound: $\Delta E \Delta t \gg \hbar \ 2$. If we consider the kinetic energy as $\Delta E = \frac{1}{2} k_B T$ and $\Delta t = 1 \ \omega$, where $\omega$ defines characteristic vibrational frequency, we get $k_B T \ \ \hbar\omega \gg 1$. This relation in solids means that the temperature should be remarkably greater than the Debye temperature. Actually for crystalline solids, results of MD simulation for heat capacities show large deviations from experimental data. For correcting this error, various schemes have been proposed like the Wigner-Kirkwood [58] expansion or path integral molecular dynamics [59]. The key and crucial point in MD simulation is evaluating the right-hand side of equation 2.3, which consumes most of the computational time in simulation process. For instance, there are special algorithms for Coulomb interactions in order to break them into two contributions which both of them can be computed in separate ways efficiently: a smooth, field-like interaction and short-ranged interactions such as Lennard-Jones potential [60].

In this study, for solving the equation 2.2 which is a system of 3N coupled second-order differential equations, first we have to discretize the time, i.e. we specify $r(t)$ at a series of time instances $t_n$. Commonly, the time axis is discretized uniformly, $t_n = n\Delta t$, where $\Delta t$ called as time step. Various simulation algorithms are used for integrating the equation of motion and finding the $r_n(t)$ , for i=1,2,…[61], and force for which both of them are the most time-consuming steps in MD simulation.

Numerical methods for numerical integration of equation of motion are categorized into two groups: Verlet Type Algorithms which consists of the Verlet Algorithm, Velocity Verlet Algorithm and Leap-Frog Algorithm. The second group is Predictor Corrector Algorithms (Nordsieck-Gear Algorithm). Verlet method [62] is among the important numerical algorithms which were produced for MD simulation.

### 2.1.2. Verlet Algorithm

Verlet algorithm allows for a relatively larger time step and uses a smaller number of arrays. This method can be directly used to solve any form of equation of motions numerically. The Verlet algorithm starts by approximating $d^2r(t)\ \ dt^2$ as

$$\frac{d^2r(t)}{dt^2} \approx \frac{r\ t+\Delta t\ -2r\ t\ +r(t-\Delta t)}{\Delta t^2} \tag{2.4}$$

Thus

$$\frac{r\ t+\Delta t\ -2r\ t\ +r(t-\Delta t)}{\Delta t^2} = -\frac{1}{m}\frac{dU(r(t))}{dr} \tag{2.5}$$

$$r\ t+\Delta t\ = 2r\ t\ - r\ t-\Delta t\ - \Delta t^2.\frac{1}{m}\frac{dU(r(t))}{dr} \tag{2.6}$$

If we know $r\ t-\Delta t$ and $r\ t$ , we can find $r\ t+\Delta t$ . That is to say, if we have information about the values of $r\ 0$ and $r\ \Delta t$ , we can solve the equation for all $r(t_n)$ for n=2,3,4,…. Although this is enough for computing the whole trajectory of the atoms, it does not determine the velocities of the atoms which are demanded for calculating various physical quantities as a function of time. For computing the velocities, we use

$$v\ t\ \equiv \frac{dr}{dt} = \frac{r\ t+\Delta t\ -r(t-\Delta t)}{2\Delta t} \tag{2.7}$$

These velocities will give the kinetic energies of each of atoms which adjust the temperature of the heat bath [62-64].

In this study the simple scaling thermostat [65] has been used in the MD simulations to control the temperature of the system studied. Using the total energy conservation of a dimer

$$E = \frac{1}{2}mv^2 \tag{2.8}$$

and rewriting this equality as the following,

$$\frac{1}{2}m(\frac{\Delta r}{\Delta t})^2 = E \tag{2.9}$$

And considering $\Delta r$ as $r_0$ and $E$ as $\epsilon_0$, $\Delta t$ can be find as,

$$\Delta t = \sqrt{\frac{mr_0^2}{2\epsilon_0}} \tag{2.10}$$

Actually, in practice molecular dynamics time step *DT*, is commonly defined as $DT = \frac{\Delta t}{100}$ [65].

### 2.1.3. Periodic Boundary Condition (PBC)

Molecular dynamics simulation occurs in a simulation box. The size of the simulation box is defined by boundary conditions. There are two main types of boundary conditions, isolated boundary condition (IBC) and periodic boundary condition (PBC). The first one is suitable for studying clusters and molecules and the second one is suited for studying bulk solids and liquids. In some systems like slab or wire

configurations both of them together can be used. In isolated boundary condition, the system which includes N particles is surrounded by vacuum, i.e. the particles in the systems interact among themselves. They have no interaction with the outside except they may respond to some well-defined external forcing. Periodic boundary condition, the one which we have applied in our study, is one of the most common boundary conditions that is used because it demonstrates an infinite number of atoms performing the simulation in a single unit cell. Introducing periodic boundary condition is essential in order to use comparatively a few numbers of molecules to simulate properties of bulk. If not, molecules which are on the surface experience different forces from molecules in the bulk. Periodic boundary condition is applicable along one, two and three directions of the simulation cell. Boundary conditions may be fixed or free ones. Applying periodic boundary conditions will eliminate the edge effect due to actual physical walls. In periodic boundary condition the simulation box is repeated throughout the space to form an infinite lattice. According to the minimum image convention as the molecule abandons the central box, one of its images enters to the box through the opposite face [55, 66,67].

### 2.1.4. Property Calculation

Statistical averages over raw trajectories yield various physical properties which are nearly divided into four groups:

1. Structural characterization, such as dynamic structure factor, radial distribution function and etc.
2. Equation of state, like phase diagrams, free-energy functions and static response functions such as thermal expansion coefficient, etc.
3. Transport which includes thermal conductivity, viscosity, diffusivity, correlation functions and etc.
4. Non-equilibrium response, the examples which are related to this property include pattern formation, plastic deformation and etc.

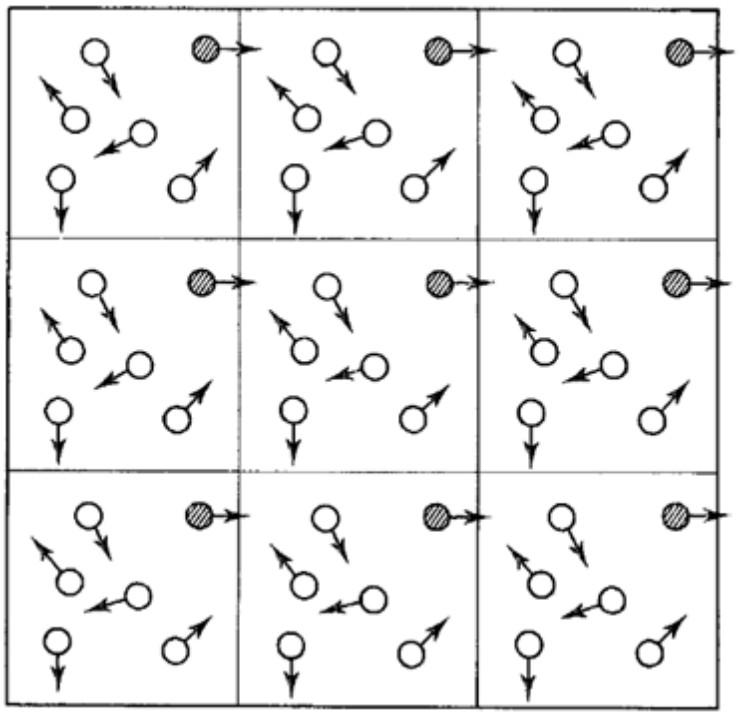

Figure 2. 1 Two dimensional periodic boundary condition. Adapted from Ref. [64].

In this simulation each of atoms are assigned randomly with an initial velocity, while the velocities of all atoms pursue Boltzmann's distribution. For various simulations, the temperature and total energy converged to their preset values. The procedure and the bath (energy, particle bath and temperature) for controlling the thermodynamics physical quantities is called thermostat. The most common thermostat scheme is called the Nosé -Hoover thermostat [68].

## 2.2. Density Functional Theory

### 2.2.1. Born-Oppenheimer approximation

The common Schrödinger wave equation is only usable for the simple systems. In practice, for understanding various properties of materials, investigating and obtaining

an insight into properties of systems of interacting electrons and atomic nuclei, atoms, molecules and solid matter is needed. Due to the strong interaction of the electrons and nuclei of materials which compose a strong interacting many-body system and contrary to the immaculate appearance of the Schrödinger wave equation of N electrons, since, in this case, it depends on the 3N coordinates, so solving it, directly, for the system of interest is acutely impractical. The time independent Schrödinger equation is defined by

$$H\psi_i\ r_1, r_2, \dots, r_N, R_1, R_2, \dots, R_M = E_i\psi_i\ r_1, r_2, \dots, r_N, R_1, R_2, \dots, R_M \qquad (2.11)$$

where $H$, $\psi_i$and $E_i$ are the Hamiltonian energy operator, wave function and energy of a system with N electrons and M nuclei, respectively. $R$'s and $r$'s represent the coordinates of nuclei and electrons. The many-body Hamiltonian can be written as

$$H = -\sum_{i}^{N}\frac{\hbar^2}{2m_e}\nabla_i^2 - \sum_{I}^{M}\frac{\hbar^2}{2M_I}\nabla_I^2 + V(r,R) \qquad (2.12)$$

where the indices i and I denote the electrons and nuclei. The first and second terms represent the electronic and ionic kinetic energy operators and the last term is the potential energy term which is describes as follows

$$V\ r,R = \frac{1}{4\pi\varepsilon_0}\left[\frac{1}{2}\sum_{i\neq j\neq 1}^{N}\frac{e^2}{r_i - r_j} - \sum_{i}^{N}\sum_{I}^{M}\frac{Z_I e^2}{R_I - r_i} + \frac{1}{2}\sum_{I\neq J}\frac{Z_I Z_J e^2}{R_I - R_J}\right] \qquad (2.13)$$

where the first term is the Coulomb potential from electron-electron interaction, the second term is potential energy from electron and nucleus interaction and the last one represents the nucleus-nucleus interaction. The solutions for the mentioned equation i.e. calculating the eigenfunctions and eigenvalues of this complex Hamiltonian is only possible after applying some approximations. Electrons are tiny masses, and thus there is a considerable mass difference between a nucleus and an electron. Using this fact,

Born and Oppenheimer [69] simplified the Schrödinger equation, supposing that electrons are moving in a field of the fixed nuclei. Therefore, the time scales of the electronic motions and nuclear motions differ from each other. Employing Born-Oppenheimer approximation and applying the atomic unit conventions ($m_e = \hbar = e = \frac{1}{4\pi\varepsilon_0} = 1$), the Hamiltonian can be written in a more simple form as

$$H = -\frac{1}{2}\sum_{i}^{N}\nabla_i^2 - \sum_{i}^{N}\sum_{I}^{M}\frac{Z_I}{R_I - r_i} + \frac{1}{2}\sum_{i\neq j\neq 1}^{N}\frac{1}{r_i - r_j} \tag{2.14}$$

The first and second terms constitute one-electron operator and the third one is two-electron operator,

$$h_1(r_i) = -\frac{1}{2}\nabla_i^2 - \sum_{I}^{M}\frac{Z_I}{R_I - r_i}$$

$$h_2(r_i, r_j) = \frac{1}{r_i - r_j}$$

$$H_e = \sum_{i}^{N} h_1(r_i) + \frac{1}{2}\sum_{i\neq j\neq 1}^{N} h_2(r_i, r_j) \tag{2.15}$$

Due to the assumption of fixed nuclei, kinetic energy of the nuclei vanishes. Besides, since the nuclei stay constant, so the term which is related to the repulsive interactions among them disappears. The resulting Hamiltonian is called electronic Hamiltonian. As regards the simplification of Hamiltonian, the electronic time-independent Schrödinger equation results in:

$$H_e\psi_e(r_1, r_2, \ldots, r_N) = E_e\psi_e(r_1, r_2, \ldots, r_N) \tag{2.16}$$

### 2.2.2. Hartree -Fock (HF) Approximation

The most challenging problem in electronic structure theory is searching for an approximate solution for equation (2.15). One such solution is suggested by the Hartree method [70]. According to this method, in order to bring the equation down to a tractable level, we assume that the N-electron system, which each of them do occupy N orbitals, becomes such a system of truly noninteracting electrons where each individual electron is moving in a mean field of the rest. As a result of this variational approach, one can assume that the wave function of the n-electron system can be approximated as the product of the individual orbitals ($\emptyset_i$):

$$\emptyset\ r_1, r_2, \dots, r_N\ = \emptyset_1\ r_1\ .\emptyset_2\ r_2\ \dots \emptyset_N(r_N) \tag{2.17}$$

Besides the important role of this method for all first-principles methods, it has some shortcomings. It does not pursue fundamental principles of quantum mechanics: the Pauli's exclusion principle and antisymmetry property, Furthermore, Hartree method ignores exchange and correlation effects. This method has been enhanced to higher perfection by Fock [71], which satisfies both the Pauli's exclusion principle and antisymmetry condition [72]. To simplify the upcoming math, we will change our notation for orbitals, from a spatial orbital, $\emptyset(r)$, to a generalized one, $\emptyset(x)$ which includes both spatial orbital and either α or β spin function.

According to Hartree-Fock (HF) approximation, the wave function of N-electron is approximated as a combination of independent one-electron wave functions in the form of Slater determinant

$$\emptyset\ x_1, x_2, \dots, x_N\ = \frac{1}{\sqrt{N!}} \begin{vmatrix} \emptyset_1\ x_1 & \emptyset_2\ x_1 & \cdots & \emptyset_N\ x_1 \\ \emptyset_1\ x_2 & \emptyset_2\ x_2 & \cdots & \emptyset_N\ x_2 \\ \vdots & \vdots & \ddots & \vdots \\ \emptyset_1\ x_N & \emptyset_2\ x_N & \cdots & \emptyset_N\ x_N \end{vmatrix} \tag{2.18}$$

Using the Slater determinant and calculating expectation value of Hamiltonian, the energy value of N-electron system is given by

$$E_{HF} = \emptyset\ H_e\ \emptyset = \sum_i^N \emptyset_i\ h_1\ \emptyset_i + \frac{1}{2} \sum_{i,j}^N [\ \emptyset_i\emptyset_j\ h_2\ \emptyset_i\emptyset_j - \emptyset_j\emptyset_i\ h_2\ \emptyset_i\emptyset_j\ ] \quad (2.19)$$

For finding the best set of orthogonal $\emptyset_i$ orbitals which minimize the ground state energy $E_{HF}$, we apply variational porinciple.

$$\emptyset_i\ x \rightarrow \emptyset_i\ x + \delta\emptyset_i\ x \quad \Rightarrow \quad \delta\ \emptyset\ H_e\ \emptyset = 0 \quad (2.20)$$

We assumed that the orbitals are orthonormal, However, it is necessary to ensure that if they will remain orthonormal under this variational procedure. In this regard, we need to minimize the Hartree-Fock energy expression with respect to changes in one-body and two-body terms using Lagrange multipliers method as follows;

$$\delta F = \delta \left[ \emptyset\ H_e\ \emptyset - \sum_{i,j} \lambda_{ij}\ \emptyset_i\ \emptyset_j - \delta_{ij} \right] = 0 \quad (2.21)$$

Through this minimization condition and doing some calculations, we finally arrive at the Hartree-Fock equations describing the orbitals:

$$h_1\emptyset_i\ x_1 + \sum_j \{ \int \emptyset_j^*\ x_2\ h_2\ \emptyset_j\ x_2\ \emptyset_i\ x_1\ dx_2 - \int \emptyset_j^*\ x_2\ h_2\ \emptyset_j\ x_1\ \emptyset_i\ x_2\ dx_2 \}$$
$$= \sum_j \lambda_{ij}\ \emptyset_j(x_1) \quad (2.22)$$

The second term in the above equation which is called Coulomb operator expresses the Coulomb interaction between two charge distributions,

$$J_j\ x_1 \quad = \quad \emptyset_j^*(x_2)h_2\emptyset_j(x_2)dx_2 \tag{2.23}$$

The last term in the left-hand side of equation (2.22) does not have a simple classical analog. It is the result of the antisymmetry requirement of the N-electron wave function. It looks like the Coulomb term, besides that it exchanges spin orbitals $\emptyset_i$ and $\emptyset_j$, therefore it is labeled as the exchange term which can be written as the exchange operator as follows:

$$K_j\ x_1\ \emptyset_i\ x_1\ = [\ \ \emptyset_j^*\ \ x_2\ \ h_2\emptyset_i\ \ x_2\ \ dx_2]\emptyset_i(x_1) \tag{2.24}$$

Using these Coulomb and exchange operators, Hartree-Fock equations significantly become more compact;

$$[h_1 + \quad _j(J_j - K_j)]\emptyset_i = \quad _j\,\lambda_{ij}\,\emptyset_j \tag{2.25}$$

Now, we can define the Fock-operator as,

$$F = h_1 + \quad \sum_{i=1}^{N}(J_i - K_i) \tag{2.26}$$

and finally, the Hartree-Fock equations will be

$$F\emptyset_i = \quad \sum_{j=1}^{N}\lambda_{ij}\emptyset_j \tag{2.27}$$

Substituting Lagrange multipliers definition in equation (2.17)

$$\lambda_{ij} = \delta_{i,j}\varepsilon_i \tag{2.28}$$

We will achieve

$$F\emptyset_i = \varepsilon_i\emptyset_i \tag{2.29}$$

Considering the above mentioned equations, it is more obvious that the Hartree-Fock equations are eigenvalue equations. Although, this method simplified the Schrödinger equation since these equations are integro-differential, coupled and also non-linear ones, still finding a direct solution is impossible. In this regard, for solving the Hartree-Fock equation, resorting to a self-consistent method is needed.

### 2.2.3. Density Functional Theory Principals

Various kinds of methods have been assigned to tackle the obstacles of solving the electronic many-body system equations. A breakthrough was accomplished when Hohenberg and Kohn [73] offered two theorems including electron density and energy functionals. Kohn and Sham [74] augmented these theorems by developing an extraordinary scheme named density functional theory (DFT). The idea behind the DFT is to replacing the many-body wave function by electron density. Indeed, the original basis of DFT can be traced back to the late of 1920s [75]. Thomas and Fermi provided a functional theory to explain the uniform electron gas. They constructed an energy functional which used the electron density as the variable and could simplify the equation decreasing it from 3N dimensions to 3 dimensions. But since they had neglected the exchange and correlation between electrons, their result was not precise enough. Even after, Dirac [76] extended this model by adding the electron exchange energy, the electron correlation effect was totally disregarded. Although, these approximations had some deficiencies but it inaugurated a crucial platform for the later development of DFT.

#### 2.2.3.1. Hohenberg-Kohn Theorem

Electronic densit performs a definite role in electronic calculations. Nevertheless, it wasn’t verified till, in 1964, Hohenberg and Kohn proved it presenting two theorems and finally gave sound foundation for the determination of electron density as the major player in DFT. These theorems therefore fulfilled the links between

Hamiltonian, wave function, external energy and electron density. The first theorem states that the ground-state electron density $n(r)$ solely determines the external potential $v_{ext}(r)$. Suppose the ground state of two N-electron systems which are defined by two different external potentials $v_1(r)$ and $v_2(r)$, so two different Hamiltonians correspond to different externals potentials,

$$H_1 = T + U + \quad {}_i v_1 \ r_i \qquad ; \qquad H_2 = T + U + \quad {}_i v_2 \ (r_i) \tag{2.30}$$

where

$$T = \ -\frac{1}{2} \quad {}_i^N \nabla_i^2 \qquad ; \qquad U = \frac{1}{2} \quad {}_{i \neq j} \frac{1}{r_i - r_j}$$

Different Hamiltonians vary only when their external potentials are different so the related Schrödinger equations of mentioned Hamiltonians will be:

$$\begin{aligned} H_1 \psi_1 &= E_1 \psi_1 \\ H_2 \psi_2 &= E_2 \psi_2 \end{aligned} \tag{2.31}$$

If these two different external potentials produce the same ground-state electron density,

$$n \ r_i \ = N \quad \psi^*(r_1, r_2, \dots, r_N) \psi \ r_1, r_2, \dots, r_N \ dr_2 dr_3 \dots dr_N \tag{2.32}$$

Now the energy will be:

$$\begin{aligned} E_1 = \ & \psi_1 \ H_1 \ \psi_1 \ < \ \psi_2 \ H_1 \ \psi_2 \\ = \ & \psi_2 \ H_2 \ \psi_2 \ + \ \psi_2 \ H_1 - H_2 \ \psi_2 \\ = \ & E_2 + \quad drn(r) \ v_1 \ r \ - v_2 \ r \ . \end{aligned} \tag{2.33}$$

Likewise it can be illustrated that

$$E_2 \leq E_1 \quad drn(r) \ v_1 \ r \ - v_2 \ r \tag{2.34}$$

If we sum the above inequalities

$$E_1 + E_2 < E_2 + E_1 \tag{2.35}$$

which this is a contraction. Therefore, it is obvious that our assumption about considering an identical density for two various external potentials is incorrect. The conclusion is as clear as this: a given electron density corresponds to only one external potential and since the external potential is defined, so the only insight of the electronic density at a certain external potential will determine the Hamiltonian, total energy and thus the ground-state wave function. This conclusion is the base of DFT calculations. Inasmuch as the electron density $n(r)$ determines the energy, so the ground state energy can be written as a functional form of density as follows:

$$\begin{aligned} E_e &= T\ n\ r\ \ + v_{ext}\ n\ r\ \ + v_{ee}\ n\ r \\ &= T[n(r)] + \ \ n\ r\ \ v_{ext}\ r\ dr + v_{ee}\ n\ r \end{aligned} \tag{2.36}$$

where T is kinetic energy, $v_{ee}\ r$ is the Coulomb potential from electron interactions and $v_{ext}\ r$ is the potential of external field which is generated by the nuclei

$$v_{ext}\ r\ \ = \ \ \sum_{i=1}^{M} \frac{-Z_i}{R_i - r} \tag{2.37}$$

In equation (2.36), the term $T\ n\ r\ \ + v_{ee}\ n\ r\ \ = F_{HK}[n\ r\ ]$ is famous for Hohenberg-Kohn functional and it doesn't have any dependency on external potential, i.e. $F_{HK}[n\ r\ ]$ is a universal functional of $n\ r$ . Even though, the ground state energy is estimated through $n\ r$ and the many-body wave function might be determined, the ultimate equation still includes an unknown $F_{HK}[n\ r\ ]$, $F_{HK}[n\ r\ ]$ is needed to be found in order to make DFT practical.

Considering the mentioned term, the energy functional will be defined as,

$$E_e = \int n\ r\ v_{ext}\ r\ dr + F_{HK}\ n\ r \qquad (2.38)$$

The Hohenberg-Kohn's second theorem, using variational principal, recognized a way to figure out the upper-bound of the ground state energy of a system. At a given $v_{ext}\ r$ , if the energy of system is minimized as much as it is possible with modifying electron density, then the minimum of energy well will be reached. The electron density which minimizes the energy of system is ground-state electron density.

As mentioned above, howbeit the Hohenberg-Kohn theorems presented the electron density as the basic quantity which defines the electronic structure and could simplify the many-body problem, but they only give the proof to the existence of a universal density functional and do not present any clues in order to construct it.

### 2.2.3.2 The Kohn-Sham Approach

In 1965, Walter Kohn and Lu J Sham [74] proposed a method which was a vital step for making Hohenberg-Kohn theorems practical for real calculations of electronic structure. In this regard, they proposed to substitute the original interacting many-body problem with an auxiliary system of non-interacting particles which each of them experience the external potential energy function $v_s\ r_i$ . The potential $v_s\ r_i$ is functional of density and satisfies the ground-state electron density $n_s\ r\ = n_0\ r$ , i.e. the ground state density of this auxiliary system is the same as the ground state density of the original one. For this N-particle fictitious system, the ground state charge density is specified as a sum over single-particle orbitals (the KS orbitals),

$$n_s(r) = n\ r\ = \sum_i \left| \emptyset_i^{KS}(r) \right|^2 \qquad (2.39)$$

where the index $i$ runs over the single-particle states and $\emptyset_i^{KS}(r)$ is an eigenfunction of the one-electron Kohn-Sham Hamiltonian $h_i^{KS}$,

$$H = \sum_{i=1}^{N} h_i^{KS} = -\frac{1}{2} \sum_{i=1}^{N} \nabla_i^2 + \sum_{i=1}^{N} v_s(r_i) \tag{2.40}$$

In order to find the energy functional for this system we have to find the true kinetic energy, so we define the term $\Delta T$ as,

$$\Delta T\ n\ = T\ n\ - T_s[n] \tag{2.41}$$

which is the difference between the true kinetic energy of the real system and the fictitious non-interacting electrons system. The kinetic energy term lacks the correlation which is related to the fact that there is no precise electron-electron interaction for the systems of non-interacting electrons. Similar to this way, the change for the electron-electron repulsion energy $\Delta v_{ee}$ can be defined as,

$$\Delta v_{ee}\ n\ = v_{ee}\ n\ - \frac{1}{2} \int \frac{n(r_1)n(r_2)}{r_1 - r_2}\, dr_1 dr_2 \tag{2.42}$$

which according to Kohn-Sham statement in their paper [67], the $v_{ee}\ n$ vanishes for the non-interacting fictitious system. In the above equation, the second term represents the classic Coulomb repulsion among electrons. Hereupon, rewriting equation (2.38), the energy functional can be expressed as,

$$E_e\ n\ = \int n\ r\ v_{ext}\ r\ dr + T_s\ n\ + \frac{1}{2} \int \frac{n(r_1)n(r_2)}{r_1 - r_2} dr_1 dr_2 + \Delta T\ n\ + \Delta v_{ee}[n] \tag{2.43}$$

The first three terms simply can be found if one knows the electron density. The functionals $\Delta T\ n$ and $\Delta v_{ee}[n]$ together define exchange-correlation (xc) energy functional.

$$E_{xc}\ n\ = \Delta T\ n\ + \Delta v_{ee}[n] \tag{2.44}$$

Exchange-correlation energy is small and contains the information which is accounts for the Pauli principle, the dynamical correlations due to the Coulomb repulsion, and also is related to the contributions of corrections to the both the kinetic energy of independent electrons and self-interaction which is caused by the Coulomb potential. This energy is very complicated and its exact form in unknown. The most challenging issue in the Kohn-Sham approach is finding the expression of the exchange-correlation potential.

Applying definition of kinetic energy functional and exchange-correlation energy, the energy functional of the reference system can be written as,

$$E_e\ n\ =\ \ n\ r\ \ v_{ext}\ r\ dr - \frac{1}{2}\ \ \sum_{i=1}^{N} \emptyset_i\ \nabla_i^2\ \emptyset_i\ \ + \frac{1}{2}\ \ \ \frac{n(r_1)n(r_2)}{r_1 - r_2} dr_1 dr_2 + E_{xc}[n] \quad (2.45)$$

Using Hohenberg-Kohn variational principle, we can minimize the energy functional $E_e\ n$ in equation (2.45) by varying the electron density constraint to $=\ \ n(r)dr$ , so the ground state energy will be found. Equivalently, we can vary Kohn-Sham orbitals $\emptyset_i^{KS}(r)$ instead of varying electron density. Hence, the Schrödinger-like equation will be,

$$[-\frac{1}{2}\nabla^2 + v_{ext}\ r\ \ +\ \ \ \frac{n\ r'}{r - r'} dr' + v_{xc}(r)]\emptyset_i = \epsilon_i \emptyset_i \quad (2.46)$$

The above equation is known as Kohn-Sham equation [74]. The exchange-correlation potential $v_{xc}$ is constructed as the functional derivative of the exchange-correlation energy:

$$v_{xc} = \frac{\delta E_{xc}[n\ r\ ]}{\delta n(r\ )} \quad (2.47)$$

The effective potential $v_{eff}$ is defined as,

$$v_{eff}\ r\ \ = v_{ext}\ r\ \ +\ \ \ \frac{n\ r'}{r - r'} dr' + \frac{\delta E_{xc}\ n\ r}{\delta n\ r} \quad (2.48)$$

As a result, the KS equation can be written as,

$$H_{KS}\emptyset_i\ r\ =\ -\frac{1}{2}\nabla^2 + v_{eff}\ r\quad \emptyset_i = \varepsilon_i\emptyset_i(r) \tag{2.49}$$

The Kohn-Sham (KS) equations are highly non-linear, pseudo-eigenvalue equations and have a specific characteristic duo to the dependency of $v_{eff}$ on the charge density which is the unknown parameter. These equations can be solved by iterative calculations forming a self-consistent cycle, i.e. one should make an initial guess for the charge density, then using this density, finds effective potential and finally calculates the KS orbitals which are the fed back into Hamiltonian. These iterative calculations will continue up to self-consistency is achieved.

### 2.2.3.3. The Local Density Approximation (LDA)

Finding exact solutions for the KS equations and many-body problem depends on finding the explicit expression for exchange-correlation energy functional. Though, in the lack of this case, one has to approximate the exchange-correlation energy, so will be able to solve KS equations (2.49) to within accuracy of the initial guess. Various kind of approximate functionals have been proposed for exchange and correlation energy.

One of the common approximations is the local density approximation (LDA) which assumes that the functional can be approximated by a function of local density $n(r)$, i.e. the energy density that a homogenous electron gas may have at every point in the space and may change from point to point.

If $n(r)$ varies slowly with r, the exchange-correlation energy is given by

$$E_{xc}^{LDA}\ n\ =\quad n\ r\ \varepsilon_{xc}^{LDA}(n\ r\ )dr \tag{2.50}$$

$\varepsilon_{xc}^{LDA}[n]$ is the exchange plus correlation energy per electron of a homogeneous electron gas with density $n$. Therefore in this approximation the exchange-correlation

energy and potential are substituted by the corresponding expressions for the homogeneous electron gas, which has a uniform density in its ground state. Within this approach, the exchange-correlation potential is defined as the functional derivative of $E_{xc}$ as,

$$v_{xc} = \frac{\delta E_{xc}^{LDA}}{\delta n(r)} = \varepsilon_{xc}(n(r)) + n(r)\frac{\partial \varepsilon_{xc}(n)}{\partial n} \tag{2.51}$$

The exchange part of $E_{xc}$energy of the homogenous electron gas can be calculated analytically, using Dirac/Slater Exchange energy of electron gas [77],

$$\varepsilon_x\ n\ r\ \ = -\frac{3}{4}[\frac{3}{\pi} n\ r\ ]^{1/3} \tag{2.52}$$

$$\Rightarrow E_x^{LDA}\ n\ = -\frac{3}{4}\ \frac{3}{\pi}^{\ 1\ 3}\ \ dr\ n^{4\ 3}(r) \tag{2.53}$$

And the exchange potential is given as,

$$v_x = \frac{4}{3}\varepsilon_x(n\ r\ ) \tag{2.54}$$

As mentioned before, exchange emerges from the Pauli principle and is precisely determined from the HF theory [71], Provided that the source of correlations is the motion of electrons, which is not independent and this term can be found for some limiting cases using the numerical results of Quantum Monte Carlo (QMC) [78] calculations for the homogenous electron gas. Some of the commonly used LDA functionals are Perdew-Zunger [79], Vosko-Wilk-Nusair [80] and M. Teter-Pade [81]. The Perdew-Zunger is one of the most parameterized approximations which was obtained by fitting the QMC results of Ceperley and Alder [78] and is given by:

$$\begin{aligned} \varepsilon_{xc}^{LDA}\ r_s\ &= \varepsilon_x\ r_s\ + \varepsilon_c(r_s) \\ \varepsilon_x\ r_s\ &= -\frac{0.916}{r_s} \end{aligned} \tag{2.55}$$

$$\varepsilon_c\ r_s\ = -\frac{0.2846}{1+1.0529\ \sqrt{r_s}+0.3334 r_s}, \qquad r_s > 1 \tag{2.56}$$

$$\varepsilon_c\ r_s\ = -0.096 + 0.032 \ln\ r_s\ +\ 0.004 \ln\ r_s\ - 0.0232\ r_s, \qquad r_s < 1 \tag{2.57}$$

where the parameter $r_s = [\frac{3}{4\pi\rho}]^{1\ 3}$ is the radius of sphere which contains the electrons.

LDA was applied for different kinds of systems and worked well for the systems which density is quite smooth such as simple and bulk metals. Furthermore, one of the surprising cases is good results of LDA even in inhomogeneous cases like covalently bonded materials, atoms and transition metals. Also it has been used widely for estimating structural and vibrational properties. There are some drawbacks in LDA functionals and it may not be suitable enough for describing some systems or reproducing binding energies, band gaps and band lengths. Besides it is weak in describing transition metals or strongly correlated systems, such as transition metal oxides.

#### 2.2.3.4. Generalized Gradient Approximation (GGA)

Charge density of real systems varies from point to point since these systems are normally not homogeneous. In this regard, LDA results, for the real systems, deviate from the real value significantly. In order to emend this deviation and procreate more accurate exchange-correlation functionals, the gradient of the charge density can be used. Concerning this matter and for generating more accurate exchange-correlation functionals, generalized gradient approximation (GGA) captures both the local and semi-local information, i.e. the charge density and its gradient at a certain point. So, GGA should bring better results forward with the general formula which uses density gradient as an extra variable:

$$E_{xc}^{GGA}\ n\ r\ \ =\ \ n(r)\ \varepsilon_{xc}^{GGA}\ n\ r\ ,\ \nabla n\ r\ \ \ dr \tag{2.58}$$

Several GGA's have been suggested during years, the most popular functionals which is used for exchange part of exchange-correlation functional $E_x^{GGA}$ are Perdew-Wang 1991 functional (PW91) [82] and Becke's 1988 exchange functional [83]. Duo to reasonable accuracy of PW91, it is applicable for a wide range of materials. Using the homogenous electron gas data, it is based on the restrictions of exchange-correlation holes and known physics. For the correlation part widely used functionals are Becke correlation functional, the Lee-Yang-Parr correlation functional (LYP) [84], Perdew-Zunger (PZ81) [79] and so on. Any kind of proposed exchange and correlation functionals can be merged together. Mixing different weights of exchange and correlation functionals begets the hybrid functionals such as B3LYP [85], the most popular hybrid functional in molecular chemistry. This is a three-parameter functional which is fitted to ionization potentials, atomization energies and etc. The B3LYP is able to explain systems with long-range interaction or with rapid variations in electron density and is appropriate for calculating bond energies, band gaps and chemical transition-state barriers.

# CHAPTER 3

# SYSTEMS STUDIED

In this chapter, structural, magnetic and electronic properties of various studied systems using two different methods, molecular dynamics and density functional theory are presented. In the first part, structural properties and also stability of iron oxide nanorods are analyzed using molecular dynamics simulation technique. Iron oxide nanorods are relaxed at 1 K° and 300 K° temperatures under the period boundary conditions. Then, in order to study the stability of these nanorods, 5% (slow strain mode) of constant strain has been applied to the simulated nanorods at 1 K and 300 K temperatures. In the second part, following the same method, structural properties and radial distribution function (RDF) of iron oxide nanoparticles at various temperatures (1K- 900K) have been investigated. In the last two parts, we shall discuss the structure, electronic and magnetic properties of iron oxide clusters, $(Fe_2O_3)_n$ (n=1, .., 5). To investigate this, we have used the density functional approach. All related results will outline in the following part. Furthermore, Graphyne 1D nanostructures and their properties, due to their outstanding applications, are of great importance, which have been discussed in this chapter.

## 3.1. Structural Properties of β-$Fe_2O_3$ Nanorods Under Strain: Molecular Dynamics Simulations

### 3.1.1. Introduction

The mechanical, electrical and magnetic properties of one- Dimensional (1D) nanostructures, due to their peculiar structure, morphology and their potential

applications in technology, science and development of nanodevices, have been researched intensively within years. Generally, 1D nanostructures comprise nanorods, nanowires, nanotubes, nanobelts and quantum wires etc. which are greatly different from their corresponding bulk materials because of the large surface-to-volume ratio, that may result in displaying some applications premier to their bulk counterparts [86,87]. It is accepted that 1D nanostructures play significant role as building blocks and interconnect units in constructing the electronic, electromechanical, optoelectronic, and complex nanodevices in a controlled way. Furthermore, some prosperous applications of these products have been observed in biomedicine, biological sensors and magnetic data storage [88-90]. Considering some applications of 1D nanoscale products as basic structure for future nanotechnology, we conclude that comprehending their various properties in various conditions is required.

Among the 1D nanostructures, nanorods (NRs) received notable attention since their potential application as building blocks for microelectromechanical systems (MEMS), display technologies, cancer therapy, waveguides, lasers and etc. have been proved. Semiconductor based NRs like ZnO ones, are utilizable in light emitting devices and in the fabrication of nanoscale transistors. ZnO NRs are used in nanoresonators in field effect transistors for detecting biological and chemical species [91-93]. Furthermore, metallic nanorods which are basic element for many nanostructures, have exposed their unique properties and promising applications in the fields of super-long waveguiding [94], biosensing [95] and many other fields [96-98]. Apart from the mentioned properties and various applications of 1D nanomaterials, numerous researches have been dedicated to the magnetic properties of these nanostructures due to their high potential for a wide-range of applications in the fields of spintronics devices, data recording devices and optoelectronics [99, 100]. Iron oxide nanoparticles can be a good example, since they have been so widely used in many fields in biomedical application [101,102], electrochromic devices [103], ferrofluids, catalysis and etc. [104]. Iron oxide nanorods, specifically, drew intense interest owing to their unique structural one-dimensionality and the magnetic properties which are controlled generally by surface effects and partly by particle-support interactions [105]. Applying

these NRs into the design of nanodevices and using them in nanotechnology, as aforesaid, demands a complete understanding and evaluation of their properties, structures and behaviors under different conditions like their response to the effect of thermal gradients, strain or compression. Taking all these into consideration, a profound characteristic for almost all applications of magnetic nanoparticles, no matter what their structures are, is stability, which we will expose it for discussion during this study.

As mentioned before, iron oxides exist in various structures; there are sixteen known iron oxides and oxyhydroxides [106]. The most common crystalline phases which they exhibit are α-$Fe_2O_3$ called hematite which is antiferromagnetic, the cubic spinel γ-$Fe_2O_3$ (maghemite) is ferromagnetic, $Fe_3O_4$ (magnetite), $Fe_{1-x}O$ (wustite), β-$Fe_2O_3$ and ε-$Fe_2O_3$ phases [101,107]. The two latter have cubic bixbyite and orthorhombic structure, respectively and β-$Fe_2O_3$ is paramagnetic. Due to numerous appealing structural, magnetic and electronic structural properties, iron oxide, $Fe_2O_3$, nanoparticles, are of peculiar importance.

Iron oxide nanoparticles (NPs) especially magnetic nanoparticles are used in a number of applications. As the magnetic properties of this class of NPs are size dependent and temperature, narrow particle size distributions are critical for an understanding of their magnetic behavior and interactions specifically in biological systems.

This study, in the first following part, attempts to address the effect of uniaxial strain on the structural properties and stability of β-$Fe_2O_3$ nanorods under various temperatures and atomic potentials using molecular dynamics (MD) simulation.

### 3.1.2. Modeling and Simulation

We generate [0 0 1]-oriented β-$Fe_2O_3$ nanorod from bulk of β-$Fe_2O_3$. The lattice constant of cubic unit cell of β-$Fe_2O_3$ is $a_0 = 9.393$ Å [108], which the nanorods are constructed by repeating this unit cell along [0 0 1] direction three times. Periodic boundary condition is applied in the stretching direction .i.e. Z direction or [0 0 1]

direction, while x and y-axes are left free. Figure 3.1 presents the related cubic unit cell.

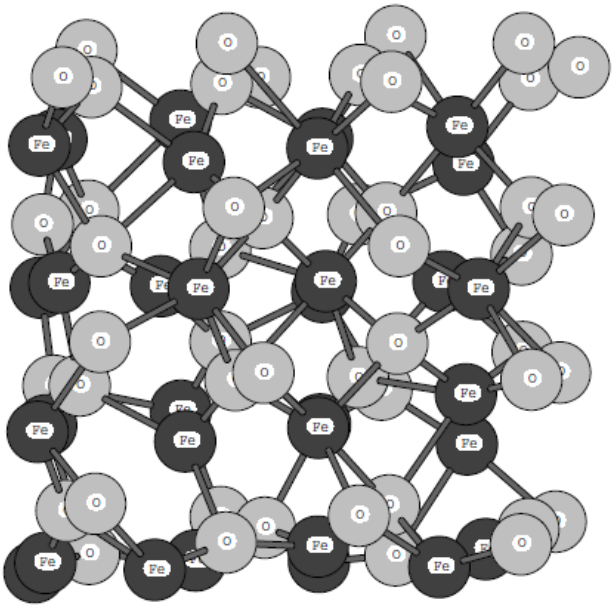


Figure 3. 1 The unit cell of β-Fe2O3. Atoms in gray are oxygens (O) and in black are irons (Fe).

MD simulations have been performed, while the interatomic forces were modeled using two different potential energy functions, PEF1 [109] and PEF2 [110], which will be explained in details in the following.

The first potential energy function, PEF1, which has been employed for simulating iron oxide nanorods, is a self-consistent pairwise interatomic potential which is developed applying empirical fitting on structural parameters and elastic constants of binary oxides using free energy minimization at P=1 atm and T=300K [109].

The analytical form of this potential energy function is composed of three terms as follows:

$$U^{1}\ r\ = \frac{Z_i Z_j e^2}{r} + D_{ij}\quad 1 - \exp(-a_{ij}\ r - r_0\ )^{2} - 1\ + \frac{c_{ij}}{r^{12}} \qquad (3.1)$$

where the first term is a) long-range Coulomb potential, the parameter ‘r’ represents the distance between atoms i and j, b) the second term is a short-range Morse function and , c) the third term is related to repulsive force between any two atoms. The Morse potential function which is an exact solution for Schrödinger equation; represents the motions of the nuclei in a diatomic molecule [111] or in other words it is frequently used in modeling bonded interactions in covalent systems in which the Coulomb term is subtracted [109] and explains energy bond stretching or compression. Three parameters are needed for calculating this potential. In this term, $D_{ij}$ or $D_e$ is well depth (defined relative to the dissociated atoms) or defines the bond dissociation energy, $a_{ij}$ is a function of the slope of the potential energy well (the smaller $a$ is, the larger the well), and the physical meaning of $r_0$ is the equilibrium bond distance. By subtracting the zero point energy E (0) from the depth of the well, the dissociation energy of the bond is assessed. Parameter, a, is calculated using this relation,

$$a = \omega \sqrt{\mu / 2D_e} \tag{3.2}$$

where μ is the reduced mass and $\omega$ is related to the bond stretching frequency by,

$$\omega = \sqrt{k / m} \tag{3.3}$$

where $k$ is the force constant of the band which can be detected by Taylor expansion of the Morse potential around $r = r_0$ to the second derivative of the potential energy function. In Figure 3.2, for more understanding, the comparison between the Morse potential (blue) and harmonic oscillator potential (green) is presented.

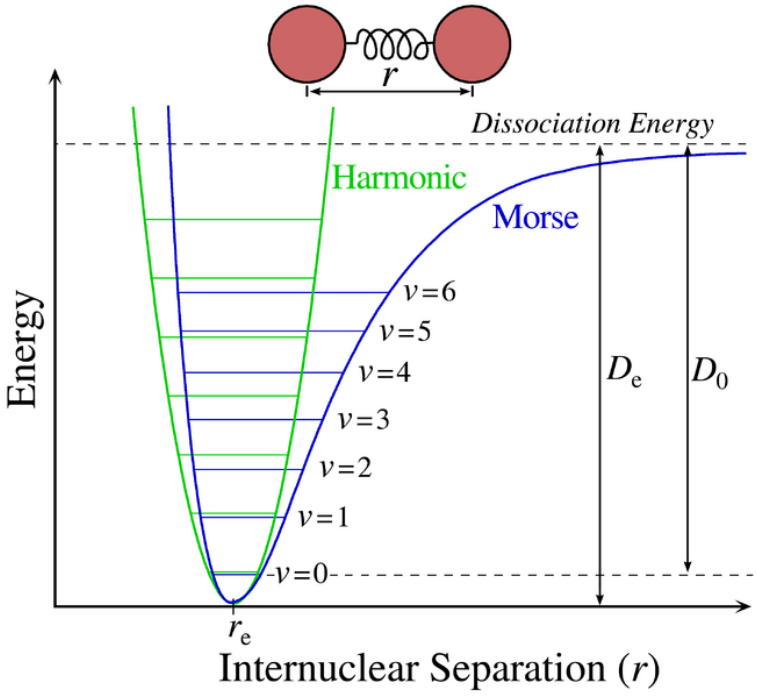


Figure 3. 2 Comparison between Morse potential and Harmonic oscillator potential. $\boldsymbol{D_0}$ is the dissociation energy, which is slightly different from the well depth $\boldsymbol{D_e}$. Adapted from Ref. [112].

As it is clear in Fig. 3.2, as the energy comes close to the dissociation energy, the Morse potential level spacing decreases, in contrast to the harmonic oscillator potential, which the space between energy levels are nearly identical. Most bands digress very little in length from their equilibrium values, thus for modeling bond stretching energy, the harmonic oscillator has been used.

The potential parameters of PEF1 which is related to β-$Fe_2O_3$ are listed in Table 3.1. As mentioned, all potentials have been derived using the relaxed fitting combined with Gibbs free energy minimization at $T$ =300 K and $P$ =1 atm [109].

Table 3. 1 The potential parameters used for PEF1. Adapted from Ref. [109].

| **Pair** | $D_{ij}$ **(eV)** | $a_{ij}$ **(Å$^{-2}$)** | $r_0$ **(Å)** | $c_{ij}$ **(eV·Å$^{12}$)** |
|---|---|---|---|---|
| **$Fe^{+1.8}$-$O^{-1.2}$** | 0.418981 | 1.620376 | 2.382183 | 2.0 |
| **$O^{1.2}$-$O^{1.2}$** | 0.042395 | 1.379316 | 3.618701 | 22.0 |

The second potential energy function, PEF2, which all calculations were based upon; is combination of Lennard-Jones [113] and Coulomb potentials. Both of them are used for representing the two-body interactions [25]:

$$U_{ij}^{\ 2}\ \ r\ \ = 4\varepsilon_{ij}\ \ \frac{\sigma_{ij}}{r}^{\ 12} - \ \frac{\sigma_{ij}}{r}^{\ 6} + \frac{1}{4\pi\varepsilon_0}\frac{q_i q_j}{r} \tag{3.4}$$

The first term is Lennard-Jones potential which is a physical model for approximating two-body interactions, i.e. the interaction between a pair of neutral atoms or molecules. This potential is shown schematically in Fig. 3.3. In the above relation, 'r' is the distance between atoms i and j, $\varepsilon_{ij} = \ \overline{\varepsilon_i \varepsilon_j}$ is the depth (i.e. the minimum) of potential well and '$\sigma$' is the finite distance at which the inter-particle potential is zero and can be written as $\sigma_{ij} = \frac{1}{2}\ (\sigma_i + \sigma_j)$.

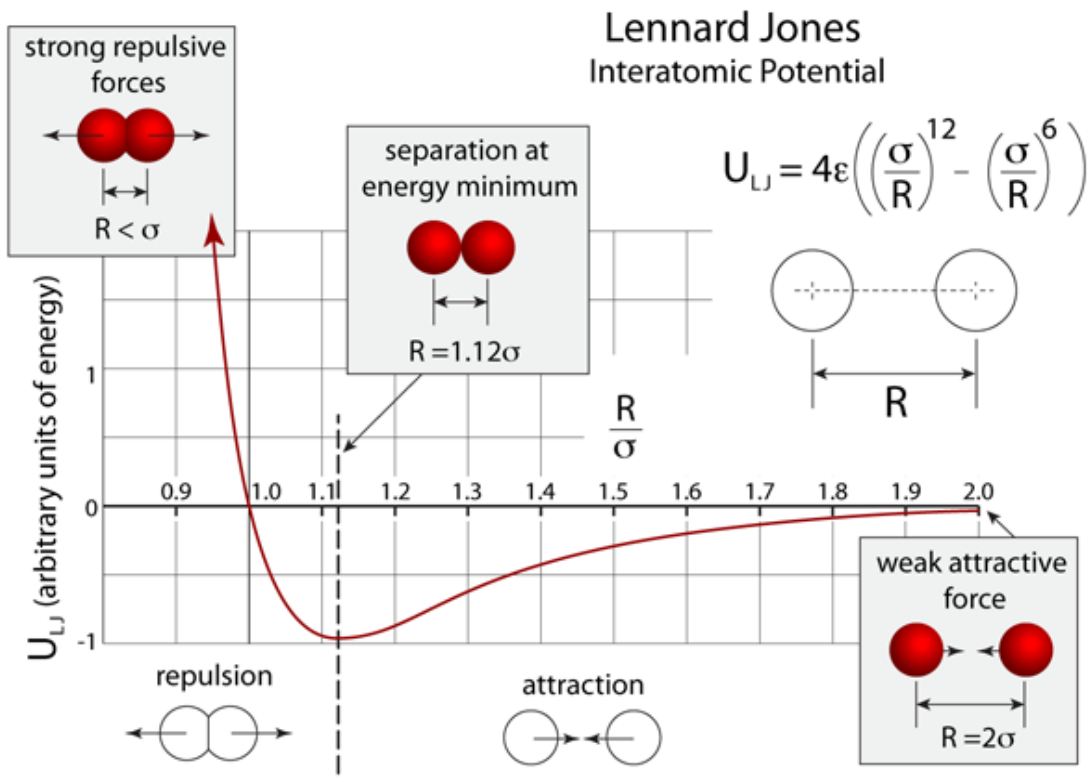


Figure 3. 3 Schematic representation of Lennard–Jones potential function. This graph shows regions of attraction and repulsion. Atoms try to minimize their potential energy are sitting at the bottom of the potential curve. When the atomic separations are to the left of the minimum the atoms repel, otherwise they attract one another. Adapted from Ref. [114].

The $r^{-12}$ describes repulsion due to overlapping of electron orbitals which is related to Pauli exclusion at short ranges. The $r^{-6}$ term describes attraction at long ranges and can be derived classically noticing how two spheres which are charged, induce dipole-dipole interactions into each other. As it is seen in Fig. 3.3 when the atoms are further apart, the attractive force is overcoming; however, the repulsive force becomes dominant when they get too close.

The second term in relation (3.4) is related to Coulomb potential, $q_i$ represents the charge on ion i. Related parameters of PEF2 for β-$Fe_2O_3$ are presented in Table 3.2.

Table 3. 2 The potential parameters used for PEF2 [110].

| **Pair** | $q$ **(\|$e$\|)** | $\varepsilon$ **(eV)** | $\sigma$ **(Å)** |
|---|---|---|---|
| **Fe-Fe** | +1.5 | $1.5546\times10^{-3}$ | 1.7 |
| **O-O** | -1.0 | $1.6841\times10^{-3}$ | 3.6 |
| **Fe-O** | – | $1.6181\times10^{-3}$ | 2.65 |

In this study we desire to observe the dependence of the physical and structural properties of β-$Fe_2O_3$ nanorods on these two employed potential energy functions (PEFs) and also to explore the temperature gradient and stretch effect on the stability of nanorods. In this regards, the equation of motions of atoms are solved by considering Verlet algorithm under microcanonical ensemble. The temperature of the systems is preserved constant at a given temperature with direct rescaling of velocities. The MD one time step is taken to be $10^{-15}$ s. Starting up at very low temperature, 1K, we let the initial model of nanorod under study is relaxed until a thermal equilibrium is established. Then, the temperature is increased to 300K and relaxation has been reached again. Using a MD code which is developed by our group that considers two mentioned PEFs, MD simulations have been performed at two temperatures 1K and 300K. For reaching to thermal equilibrium, under different conditions, the total number of time-steps varies between 300,000 to 2,000,000 steps. When the total energy of the system reaches to a smooth region for a significantly long time, the system is assumed to be at equilibrium.

After relaxing the system at both temperatures and each of PEFs, in order to investigate the structural and strain behavior of nanorods, we start stretching nanorods uniaxially. The stretching of nanorods is done along the [001] direction, i.e. the z-coordinates of each of the atoms is multiplied by a factor 1.05, which gives rise to a nanorod stretched by 5% along the z-direction. In Fig. 3.4, the initial and final length

of the stretched β-$Fe_2O_3$ nanorod for one step of strain application is shown. The percentage change, $\%\Delta L$, in the length of the nanorod is defined as,

$$\%\Delta L = 100 \times (L_i - L_0)/L_0 \tag{3.5}$$

where $L_i$ is the length of the nanorod at the $i^{th}$ stretching step and $L_0$ is the initial length of nanorod. The notation is self-explanatory.

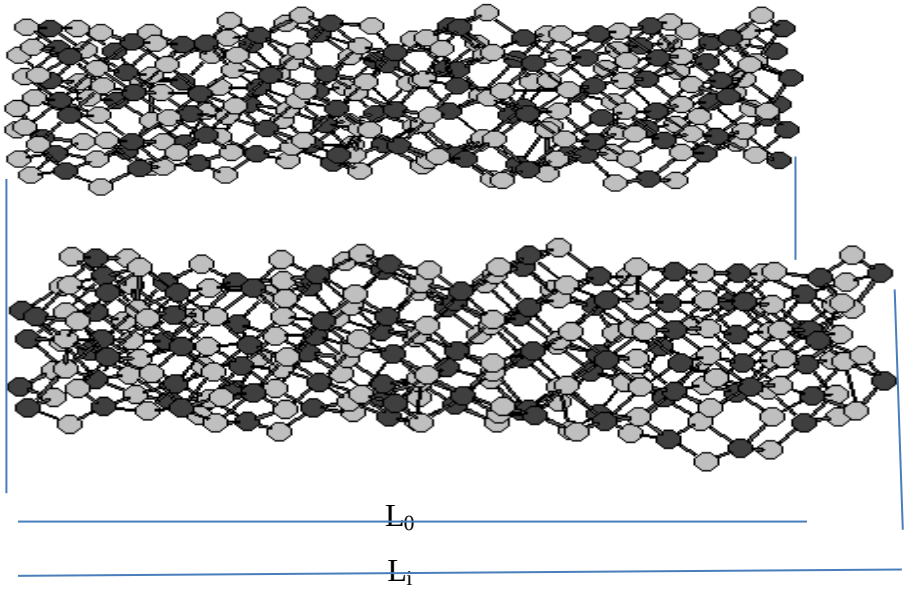


Figure 3. 4 Illustration of the strain application

In every step, after stretching, we let the system reach equilibrium again. This process (stretch-and-relax) has been followed till the system considered distorts. Distortion is explained as a deviation from the initial model like separation of atoms or geometrical deviation which alters the entire structure. Here, in our case, having strained and stretched in several steps, the nanorod is broken, i.e. the distance between any atoms in the breaking region transgresses a predetermined value. This value is 2.5 Å in the

present study. The total number of stretch-and-relax cycles before nanorod is broken is perceived to depend on both the PEFs and temperature.

### 3.1.3. Results and Discussion

Every $Fe_2O_3$ nanorod includes 240 atoms totally that 96 of which are Fe and 144 are O atoms. The structures of the β-$Fe_2O_3$ nanorods after energetic relaxation and strain application which have been simulated with two different PEFs and at 1K and 300K are presented separately in Figures 3.5 to 3.8, respectively. Each number at the right hand side of nanorods indicates the corresponding strain step. At first, the β-$Fe_2O_3$ nanorod which is simulated with PEF1 at 1K has been studied. During the simulation, in order to investigate the influence of the strain along the [001] direction; different snapshots of nanorods have been taken which are all presented in Fig. 3.5.

Within the first four pictures, the nanorod appears to preserve its overall structure under strain and seems still intact, whereas the side view at step 5 demonstrates that the effect of the applied strain seems to be somehow noticeable and nanorod begins to lose its symmetric structure. As the strain application furthers, the bonds between nanorods atoms start to outspread, so that as it is obvious in Fig. 3.5, two breaking parts are seen in picture 7 and the structure changes continue till picture 12, in this step, the whole nanorod has been totally torn off into three different pieces. The non-smooth deformation of the β-$Fe_2O_3$ nanorods, which has occurred in an irregular manner is the most considerable finding in this structure under PEF1 and at T=1K. As the nanorod is being stretched, its shape has been distorted significantly, and having been broken the three fragments are not a well-formed nanorod anymore.

In order to delve more into the effect of the temperature on the stability of the β-$Fe_2O_3$ nanorods under strain, an equivalent simulation with PEF1 at the room temperature, T=300K, has also been conducted. The results seem to be somewhat different from the same structure at 1K. Figure 3.6 displays the snapshots of the β-$Fe_2O_3$ nanorod taken at the same time like those of Fig 3.5. At this temperature, the nanorod keeps its shape

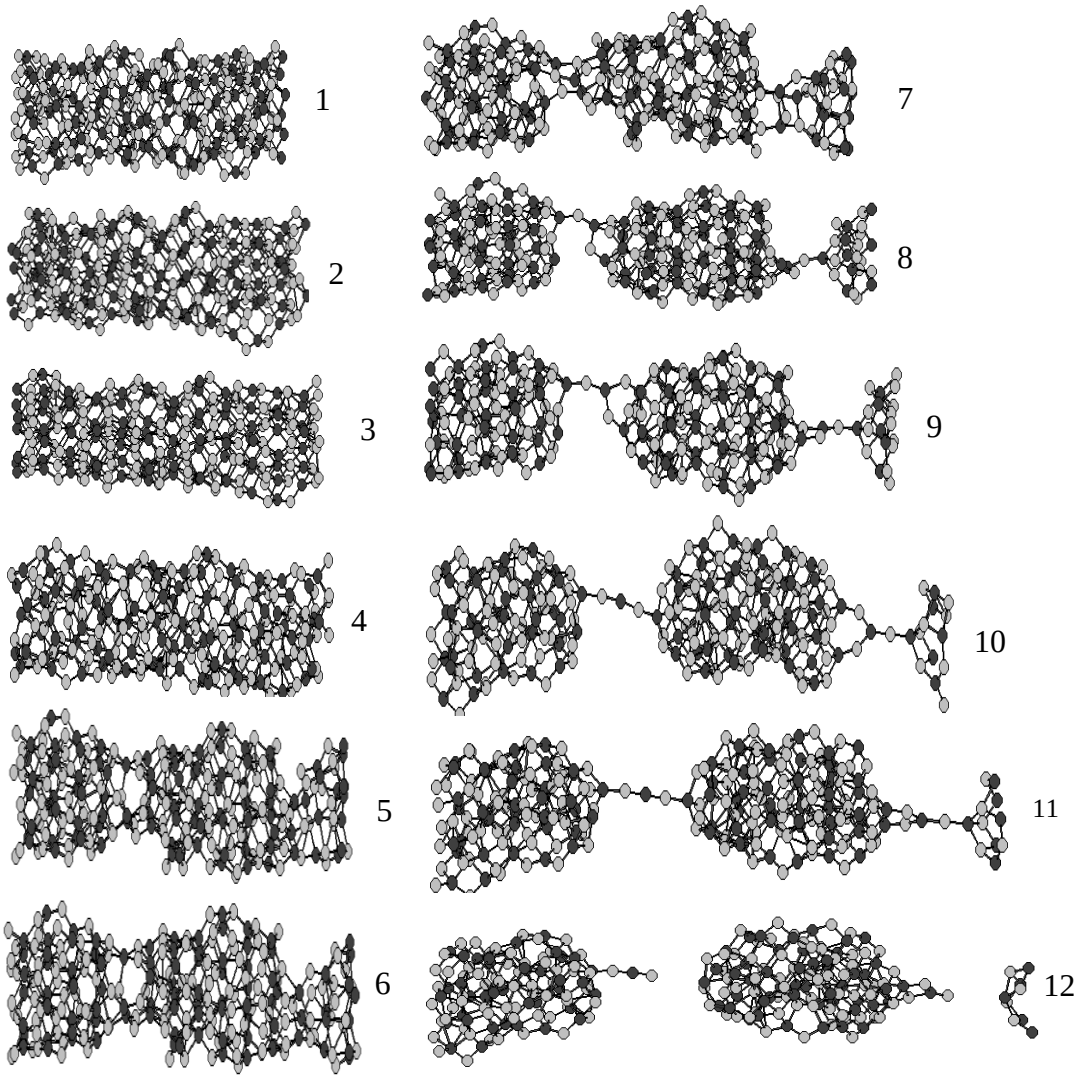


Figure 3. 5 The β-$Fe_2O_3$ nanorod under strain with PEF1 at 1 K. Each of pictures are sideviews of nanorods at the represented strain step number.

stand still within the first four pictures, i.e. there is no remarkable transformation till the step 4. The loss of well-formedness shape of the nanorod is obvious in picture 5 with only one breaking region but later on it behaves as though it would be broken into three different pieces. However, it has been separated into just two fairly equal-sized pieces at the end. All this has been presented in pictures 11 and 12 in Fig.3.6. What is once more noticeable is the little resemblance of the final fragments in

comparison with the unstretched nanorod form. Furthermore, according to the Fig. 3.6, the diameter of the nanorod starts up to decrease in the midpoint at step 5, where the elongation also displays its effect on the nanorod. This reduction in the thickness of nanorod or in the diameter of the subject material which is caused by the irrelevant localization of the tensile stress in a particular region is called necking point [115]. This reduction in the diameter and constituting necking points continues till the end of steps but the only difference is that in each of steps 5, 11 and 12 there is only one necking point, while in steps 6 to 10, two necking points have been appeared near the both ends of the nanorods not at midpoint. By comparing Figures 3.5 and 3.6, it is clear that at T=1K the nanorod seems to be more rigid; firstly it seems that it would be separated into three pieces with two breaking regions and finally this happens (Fig. 3.5). Nevertheless, at 300K, the nanorod pretends to be irresolute about its fragmentation due to the non-fixed number and places of breaking areas ( see Fig.3. 6). It could be tentatively said that the nanorod as a whole changes its form in an irregular manner. This relatively alternation demonstrates that temperature augmentation possess considerable role for this model. All these changes should be inevitable because of the increased temperature that has reduced the rigidity of the nanorod to a fairly great extent by giving kinetic energy to the atoms of the nanorod. In other words, temperature has made the nanorod to gain more flexibility. Obviously, temperature plays a paramount role on the stability and stretching characteristics of the $\beta$-$Fe_2O_3$ nanorods. It has been noted that it takes the same amount of time for the nanorod to break totally at temperatures of 1K and 300K; however, the end results are not identical.

Having presented the results of simulations conducted with PEF1, it is time to consider the changes with PEF2. In the second part of our study of $\beta$-$Fe_2O_3$ nanorods, both the initially purposed geometry that is figured out to be stable at lower temperatures, and the relaxed geometries at two temperatures 1K and 300K are studied for comparison stability of nanorods and making decision whether the structure is viable or not, or how much is the stability of the structure. A series of pictures displaying the simulation results of the same structure which have been performed at

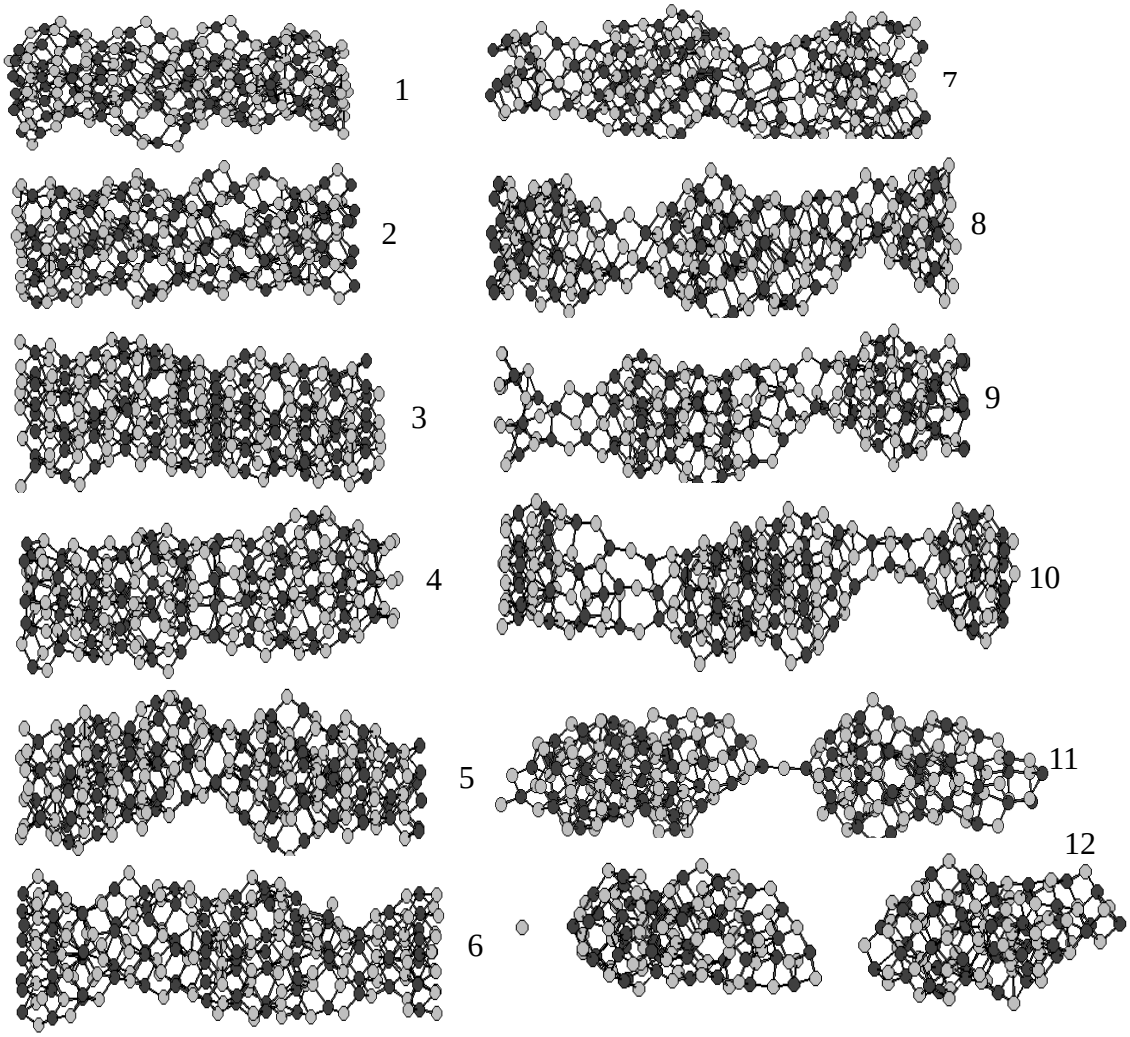


Figure 3. 6 The β-$Fe_2O_3$ nanorod under strain with PEF1 at 300 K.

1K are presented in Fig. 3.7. Studying these results shown in Fig. 3.7, the first matter which is noticeable is that the fragmentation mechanism with PEF2 looks like wholly different from that of PEF1 in Figure 3.5. After stretching, there seems to be some atomic ring-chain structures in the breaking areas of the nanorod in Fig. 3.7, while the corresponding feature in Fig. 3.5 is with only some atomic chains and formation of necking point in breaking area. Other differences between Figures 3.5 and 3.7 are also

substantive: the nanorod under strain is broken after 12 times units with PEF1, although it is in one piece with just a rather distorted shape, but it is distorted within 16 times units with PEF2 in Fig. 3.7. When we consider the simulation results of PEF1 at 1K and PEF2 at the same temperature in Fig. 3.5 and Fig. 3.7 altogether, we encounter with almost different pattern of deformation of nanorods. It is clear from these figures that although minor changes occur in the nanorod structure right after the strain application, but at the $7^{th}$ time unit with PEF2, the nanorod starts to deform but before that it keeps its overall shape; however, the nanorod tends to distort at the $5^{th}$ time unit with PEF1. It is clear that there is a relationship between MD simulations and the kind of PEF utilized, i.e. the outcomes of MD simulations are related to the type of PEF being used, as might be predicted. Each PEF displays the β-$Fe_2O_3$ nanorod under strain is in its own unique manner; that is, various PEFs would yield different properties for the very similar material. More comparison of Figures 3.5 and 3.7 would indicate the starting point of the structure deformation at the $5^{th}$ time unit utilizing PEF1, while the nanorod remains intact till the $6^{th}$ time unit and after that the first deformation starts at the $7^{th}$ time unit with PEF2. All in all, β-$Fe_2O_3$ nanorod found to be more stable against stretching using PEF2 rather than PEF1.

Following this scenario and for more comprehension on the relation between the PEFs and temperature effect on the stability of β-$Fe_2O_3$ nanorods, again the MD simulation has been conducted for these nanorods under strain at 300K with PEF2, which the related results are presented in Fig. 3.8. This Figure includes 21 snapshots in whole that 12(16) of which have been taken at the same time as that of Figures 3.5 and 3.6 (Fig. 3.7). Our simulation results revealed that, this time there is an earlier time for structure deformation at about the $3^{rd}$ time unit. Unlike the previous cases, the deformation process takes place more slowly; diameter of nanorod begins to reduce in the midpoint at step 7 and continues to step 9, then the diameter reduction point moves to the left and right end.

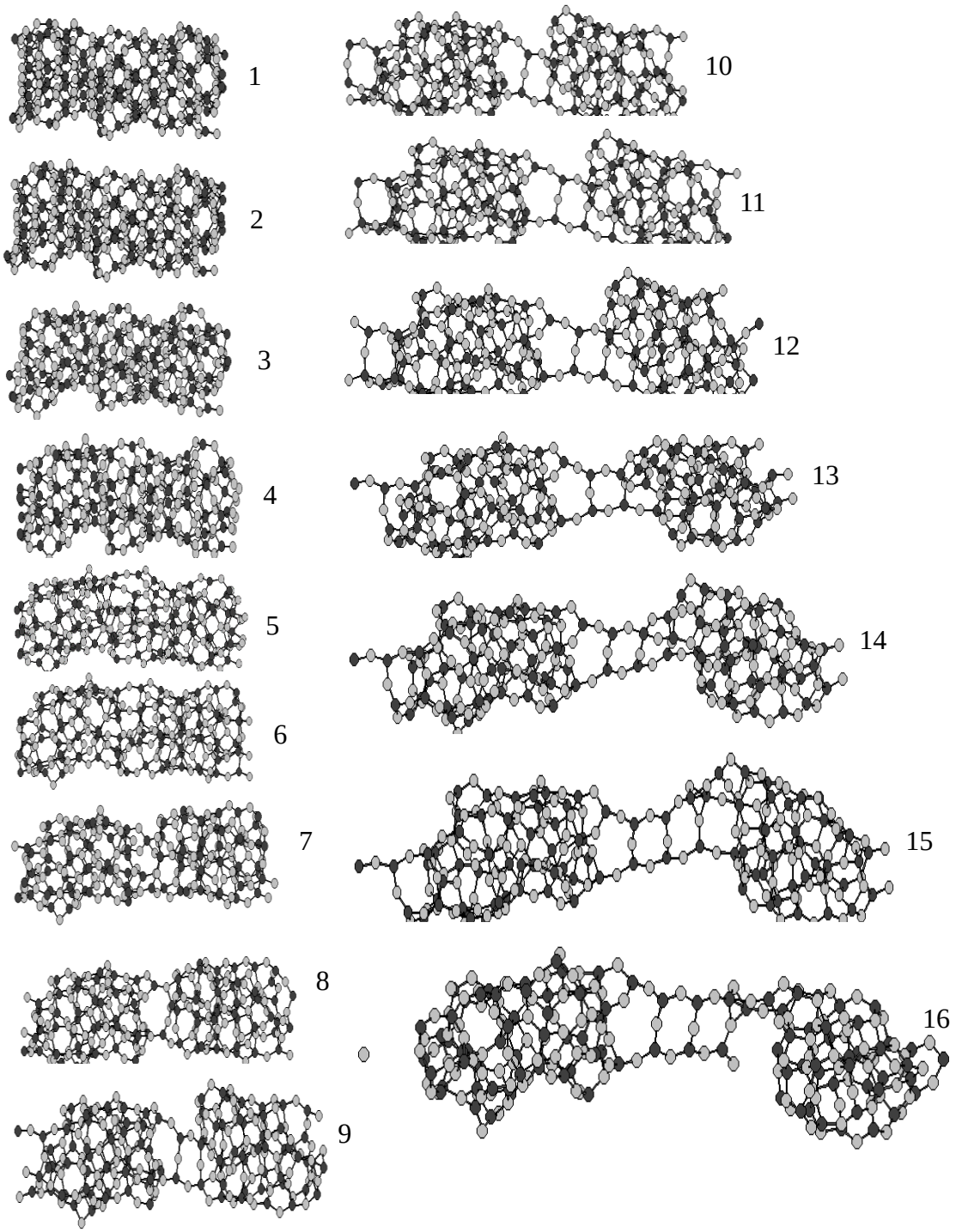


Figure 3. 7 The β-$Fe_2O_3$ nanorod under strain with PEF2 at 1 K.

Nanorod keeps its structure without completely fragmentation, finally the breaking occurs at the middle point of nanorod and the full distortion happens at the 21$^{st}$ time unit, the time that nanorod broken into two different pieces with different sizes. Considering Figures 3.7 and 3.8, it becomes indicative that the fragmentation process of the β-$Fe_2O_3$ nanorod is more demanding at 300K than at 1K with PEF2. The more of the kinetic energy just because of the higher temperature has led to the more flexibility of the nanorod. Unpredictably, the breaking areas are not static during the stretching process. This becomes more obvious when comparing pictures 20 and 21 of Fig. 3.8: they are actually really anomalous. As it is seen, the simulation of the same structure carried out at the room temperature exhibit somewhat different consequences as seen from Fig. 3.8. Consequently, the most important point is that the nanorod at 1K seems to be more rigid rather than at 300K. Putting away the longer process of deformation, all the characteristics gained with PEF2 are nearly the same as those obtained with PEF1 tackled above. In general, the comparison of the obtained outcomes from different PEFs leads to the conclusion that the β-$Fe_2O_3$ nanorod simulated with PEF2 indicates more stability at 300K.

Figure 3.9 shows the strain ($\%\Delta L$) versus strain-energy ($E_s$) curves which presents the energetic behavior of the β-$Fe_2O_3$ nanorod under strain with two different types of PEFs and two temperatures 1K and 300K. As mentioned before, the strain is defined as difference in length in percentage, namely ($\%\Delta L$). In our study, the amount of potential energy stand in atoms which is needed for atoms rearrangements undergoing a known strain magnitude might be defined as strain- energy $E_s$ which is yielded due to the moment of atoms prior to complete breaking. In other words, it is defined as the difference between the total potential energy of the systems, $E_i$, which is under strain, in the i$^{th}$ time-step, and the energy $E_0$ before the implementing strain: $E_s = E_i - E_0$, where $i = 0,1,2,3,\ldots..$strain. More importantly, the general norm seen in these curves sounds meaningful, as it is expected, the more the degree of strain, the more the strain-energy $E_s$, would be. As it is obvious in Fig. 3.9 $\%\Delta L = 10$, the proportion of increase in $E_s$, to strain is roughly linear. Howbeit, the constants for PEF1 and PEF2

are not identical, they seem nearly the same, specially graphs which are related to PEF1 at 1K and 300K, it is hold true for PEF2 also.

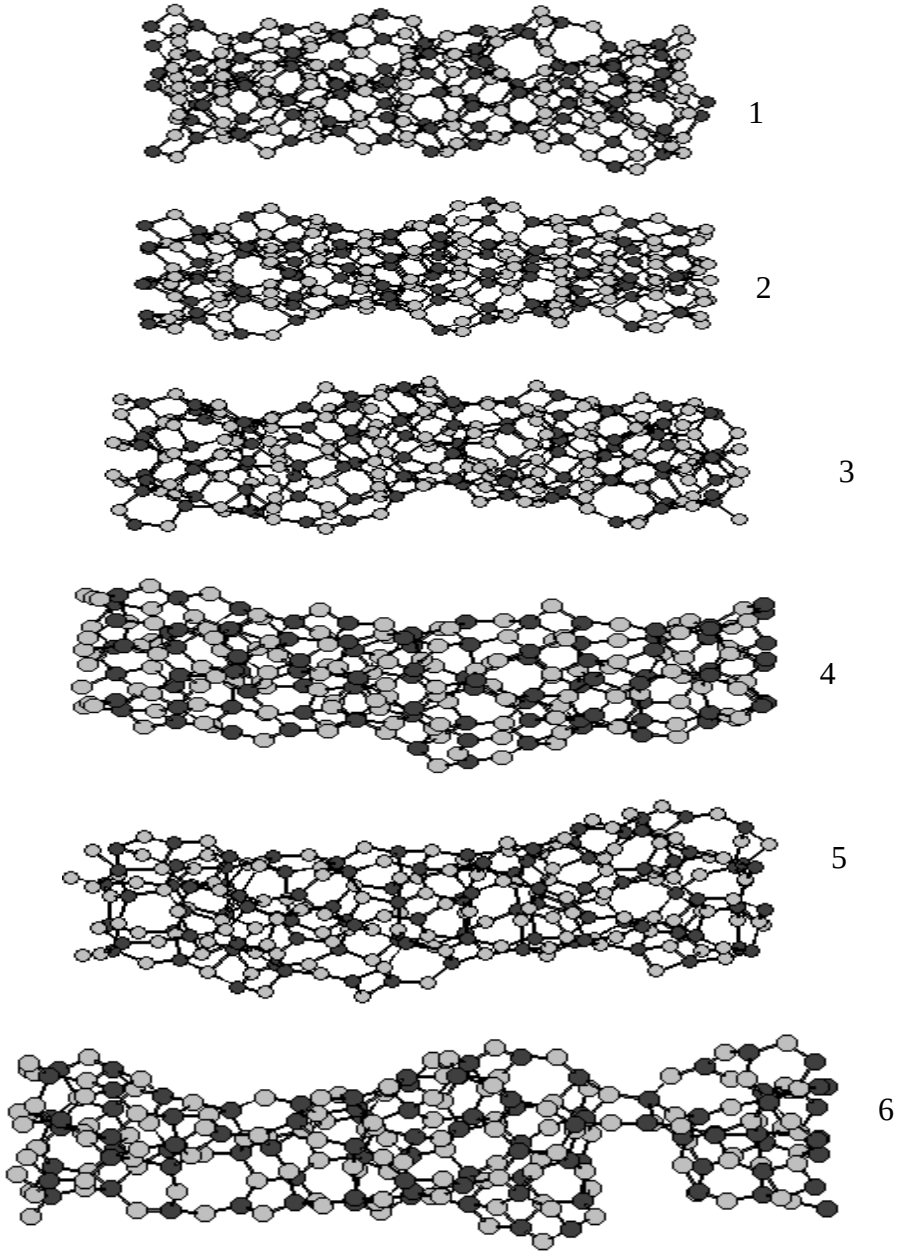


Figure 3. 8 The β-$Fe_2O_3$ nanorod under strain with PEF2 at 300 K.

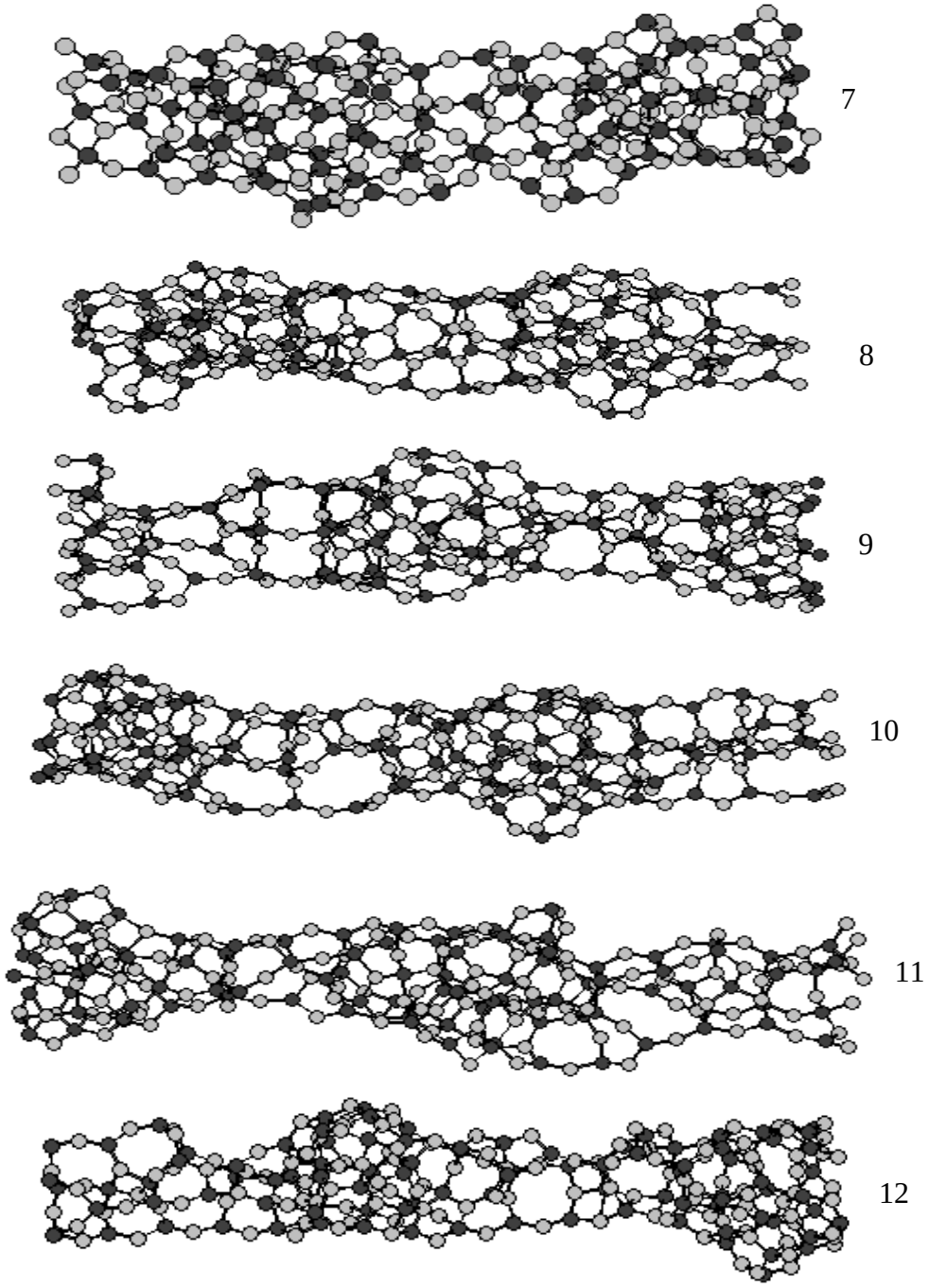


Figure 3.8 (continued)

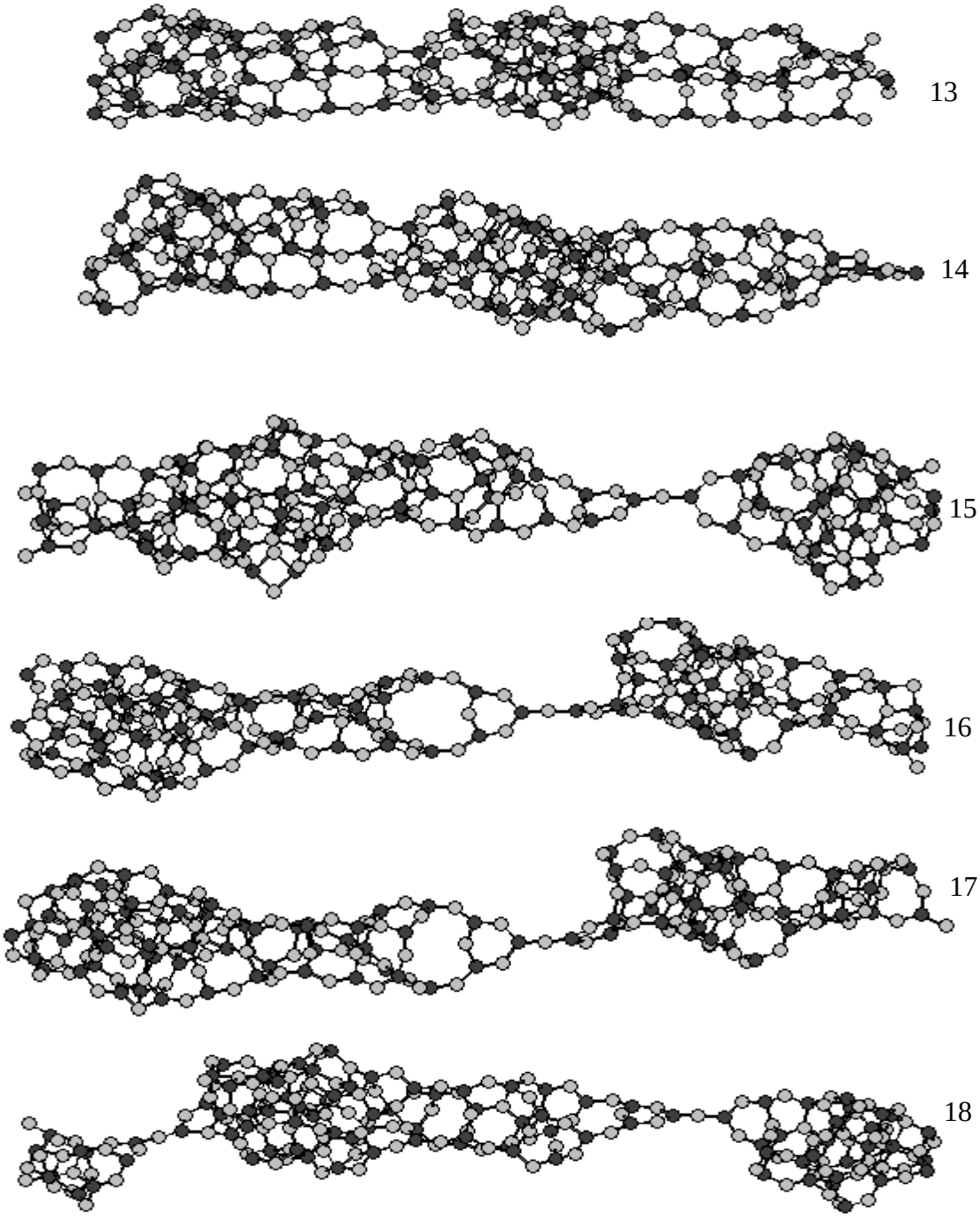


Figure 3.8 (continued)

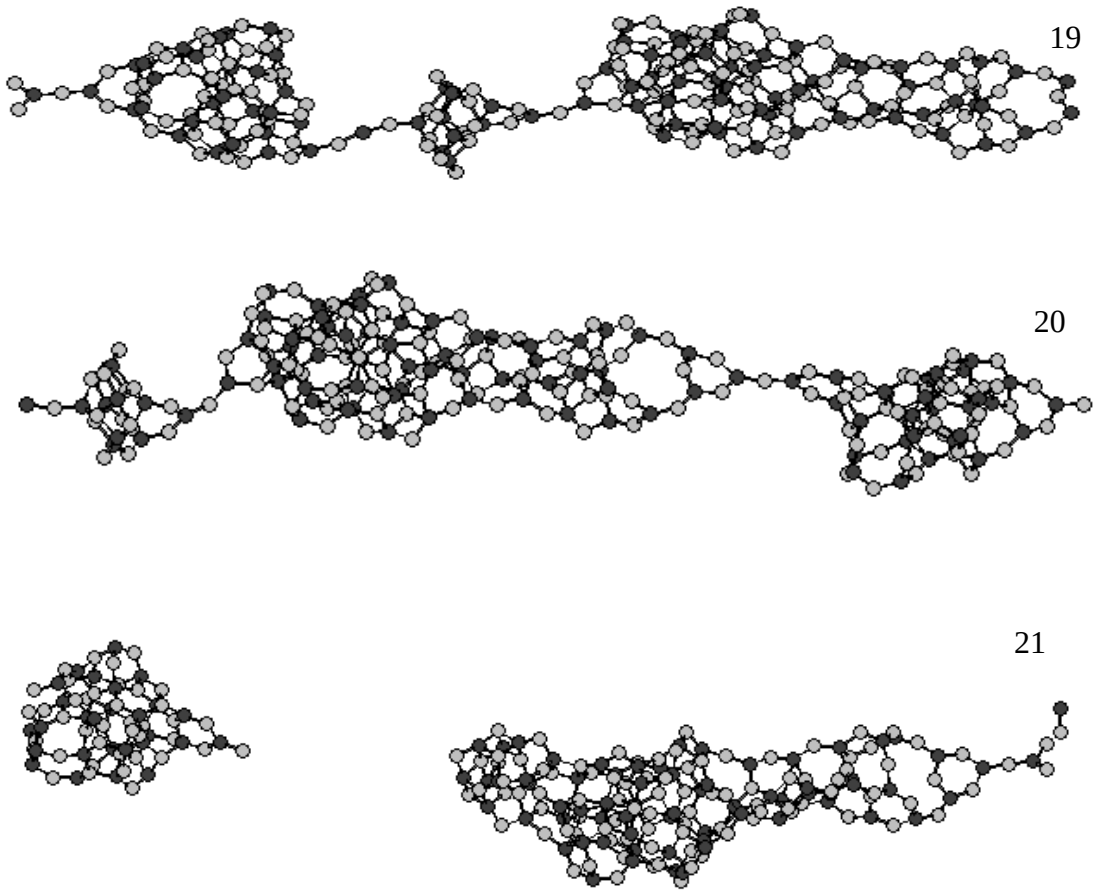


Figure 3.8 (continued)

From the Fig. 3.9, we see that the for the values of $\%\Delta L < 10$, with the PEF1, the strain-energy $E_s$ curves at 300K and also with PEF2 at 1K are negative; however, it is almost zero for PEF1 at 1K.

Contrary to these three foresaid cases, the trend is somewhat different for PEF2 at 300K. In general, we may note that at the outset of MD simulation, this nanorod was not in a perfect relaxed state, it might say that opposite to the externally applied strain, the nanorod was "pre-compressed" in the [001] direction and also in two other directions. The most helpful result gained here is that at first, when the strain is applied in the [001] direction, the nanorod comes to its unstressed state, which causes

the relevant strain-energy decreases to negative values, just after this step, the actual stretching begins. For clarifying the cause of this special characteristic and behavior of nanorod , in studied conditions, we might declare that it is related to the fact that the simulated β-$Fe_2O_3$ nanorods have been created from repeating a unit cell along the [001] direction three times and this unit cell was cut out of the iron oxide bulk. In ordinary condition, a unit cell in bulk matter is in its naturally stressed or compressed state. As we have done in this study, whenever we employ a unit cell in order to make a 1D nanorod, it is not astonishing that the so-obtained nanorod to be primarily in a pre-compressed state. Hence, at the inception of a simulation, the first reaction of the nanorod may be undergoing relaxation. However, all these are pure conjectures. Although all these are mere surmises, they plausibly account for the nearly intact nanorods seen at the initial stages of simulations, depicted in Figures 2-5.

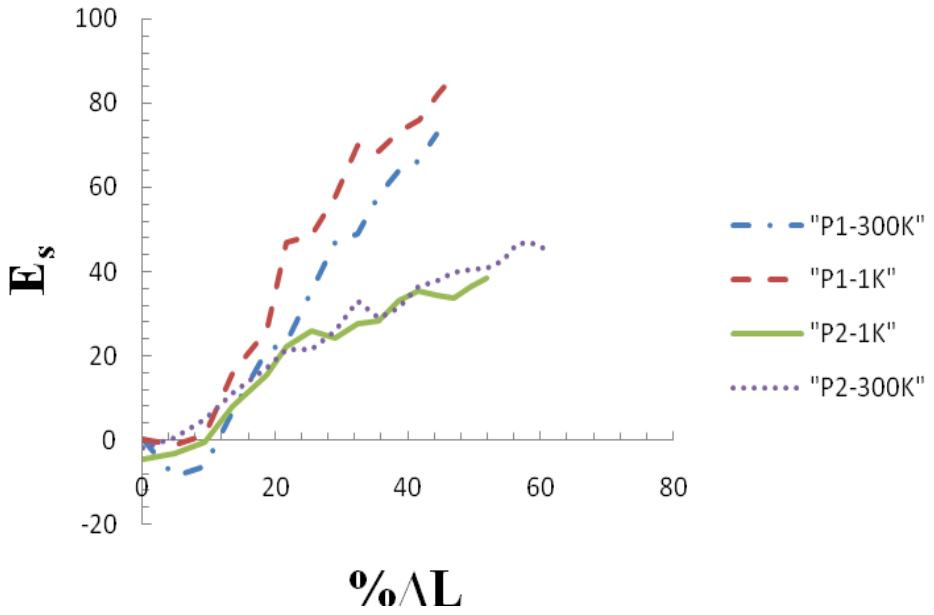


Figure 3. 9 (Color online) Strain $(\%\Delta L)$ versus strain-energy $(E_s$, in eV$)$ curves.

## 3.2. Structural Properties and Radial Distribution Function of Iron Oxide Spherical Nanoparticles Using Molecular Dynamics Simulation

### 3.2.1. Introduction

In the second part of this research study, we have carried out molecular dynamics simulation studies of spherical nanoparticles. Different sizes of nanoparticles have been simulated in order to substantiate better understanding of structural properties of these nanoparticles at different temperatures. Radial distribution functions are perhaps the most common tool to analyze the structure of any condensed phase. In this regard, Radial (atomic) distribution [116-119] function which is an important structural characteristic for a system of particles like molecules, atoms, colloids and etc. have been developed for all samples, temperature has been increased step by step and radial atomic distribution function for spheres within 3, 4, 5 and 6 Å radius of nanoparticles have been studied.

### 3.2.2. Methods of Simulation

As mentioned, specifying the initial positions of configuration of atoms is the first step for treating the system with molecular dynamics method. The mentioned unit cell in the first part of this chapter is used for generating iron oxide spherical nanoparticles. A FORTRAN script has been used for generating and optimizing spherical nanoparticles. Radius of nanoparticles, thus the number of atoms constituent each of spherical nanoparticles varied. Four different spherical nanoparticles with radius 3, 4, 5 and 6 Å were optimized.

The first empirical many-body potential energy function (PEF1) which we have used in part 3.1 is used in the molecular dynamic simulation of iron oxide spherical nanoparticles. Using PEF1, the motion equations using the Verlet algorithm and canonical ensemble NVT are solved. The temperature scaling is considered at every

MD step, the particle initial velocities are defined from Maxwell distribution and every time step is supposed to be $10^{-15}$ s. The iron oxide nanoparticles simulation with specific radius started at low temperature, 1K, and by a predetermined step size 100 K, the temperature enhanced till the nanoparticle started to deform. Deformation condition is defined as the collapse of the initial structure, or breaking of atoms. At every temperature rise, the system is relaxed and molecular dynamic simulation runs of various steps till system reaches to equilibrium.

Considering a homogeneous distribution of the atoms/molecules in space, the RDF represents the probability to find an atom in a shell dr at the distance r of another atom chosen as a reference point [116-119], as it is shown in Fig. 3.10 schematically.

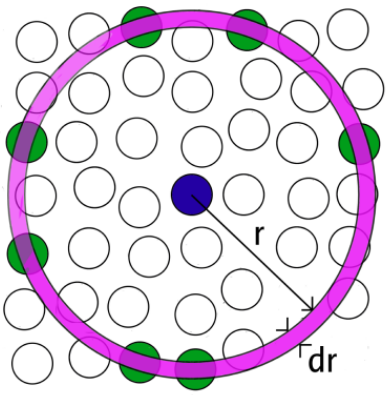


Figure 3. 10 Space discretization for the evaluation of the radial distribution function (RDF).

In the construction of the radial distribution function for our samples, we developed spherical nanoparticles of $Fe_2O_3$ bulk for four nanoparticle models with various radiuses.

After this initialization stage of modeling spherical nanoparticles, we calculated the center of mass (CM) of each sphere. Then we transferred the origin to the CM, and in

the next step we found the distances of each of atoms with respect to the new generated origin. Comparing these results, we sorted these values in descending order to determining the first nearest neighbor, the second nearest neighbors and so on and made a radial density profile of the two constituent atoms as a function of distance from the center of mass of the particles. This process is followed by applying Gaussian broadening on the sorted distances. Now the radial distribution function profiles are ready for spherical nanoparticles within 3, 4, 5 and 6 Å radiuses.

This radial distribution function can be used to verify the structure evolution of $Fe_2O_3$ spherical nanoparticles during the temperature augmentation process. In this regard, we increased temperature step by step and studied the graphs of atomic radial distribution versus radius of nanoparticles. Since each $Fe_2O_3$ nanoparticle consists of two kinds of atoms oxygen and iron, in each case, there are three radial distribution functions in this system, for iron atoms, oxygen atoms and for whole nanoparticle, which turn out to have almost different character.

### 3.2.3 Results and Discussion

The initial structure and the relaxed ones of various spherical nanoparticles at various temperatures and also the related RDFs are displayed in the Figs 3.11- 3.15. As it is clear in Fig. 3.11, the nanoparticle with radius equal to 3 Å consists of 11 atoms in total, with 6 oxygen atoms and 5 iron atoms. The initial temperature is 1K and the radial (atomic) distribution function graphs for Fe, O atoms and also both of them is presented. As mentioned before, radial (atomic) distribution function provides distribution pattern of particles or atoms in Fe-O system.

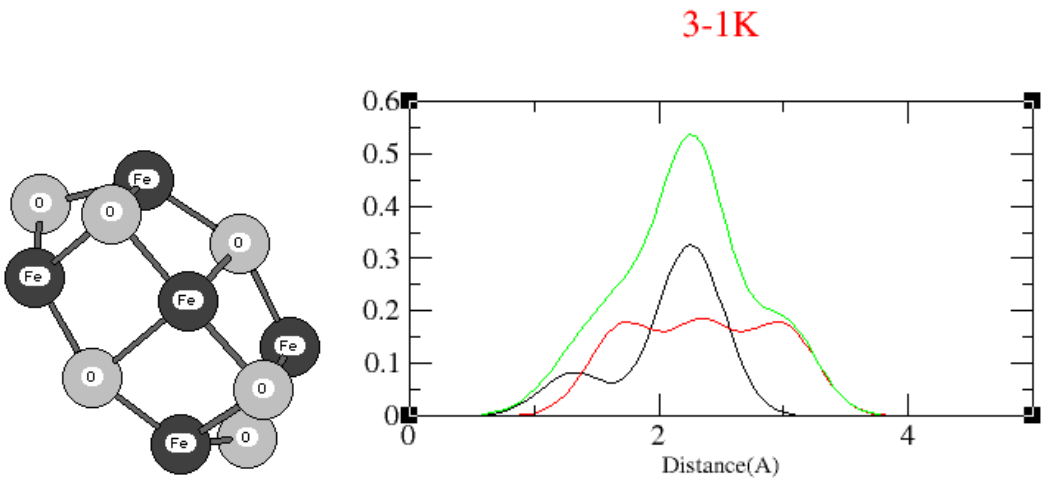


Figure 3. 11 Relaxed structure of spherical nanoparticle with r= 3 Å at T=1K and radial (atomic) distribution function (RDF). Black and red lines are related to distribution function of Fe and O atoms, and the green line displays distribution pattern of all atoms.

For studying the heat treatment of nanoparticles and effect of temperature on the distribution of atoms temperature is increased from 1K to 900K by 100K interval. Figures 3.12 (a) – (g) illustrated the relaxed structures of nanoparticles with radius 3 Å and related radial distribution functions at 100 K, 200 K, 300K, 400K, 500K, 600K and 900 K.

As it is seen in Figs 3.11 and 3.12, at r= 3 Å , iron oxide spherical nanoparticles keeps its cage structure up to 400K, its bonds begin to break at 500 K, but after this step again, in 600 K and 900 K, it seems that nanoparticle tries to not lose its initial structure completely. The atomic distribution graphs for Fe and O atoms, separately; are also presented in Figs 3-10 and 3-11 for r= 3 Å at different temperatures. From these graphs, we comprehend that particles slowly move to farther distances from CM,

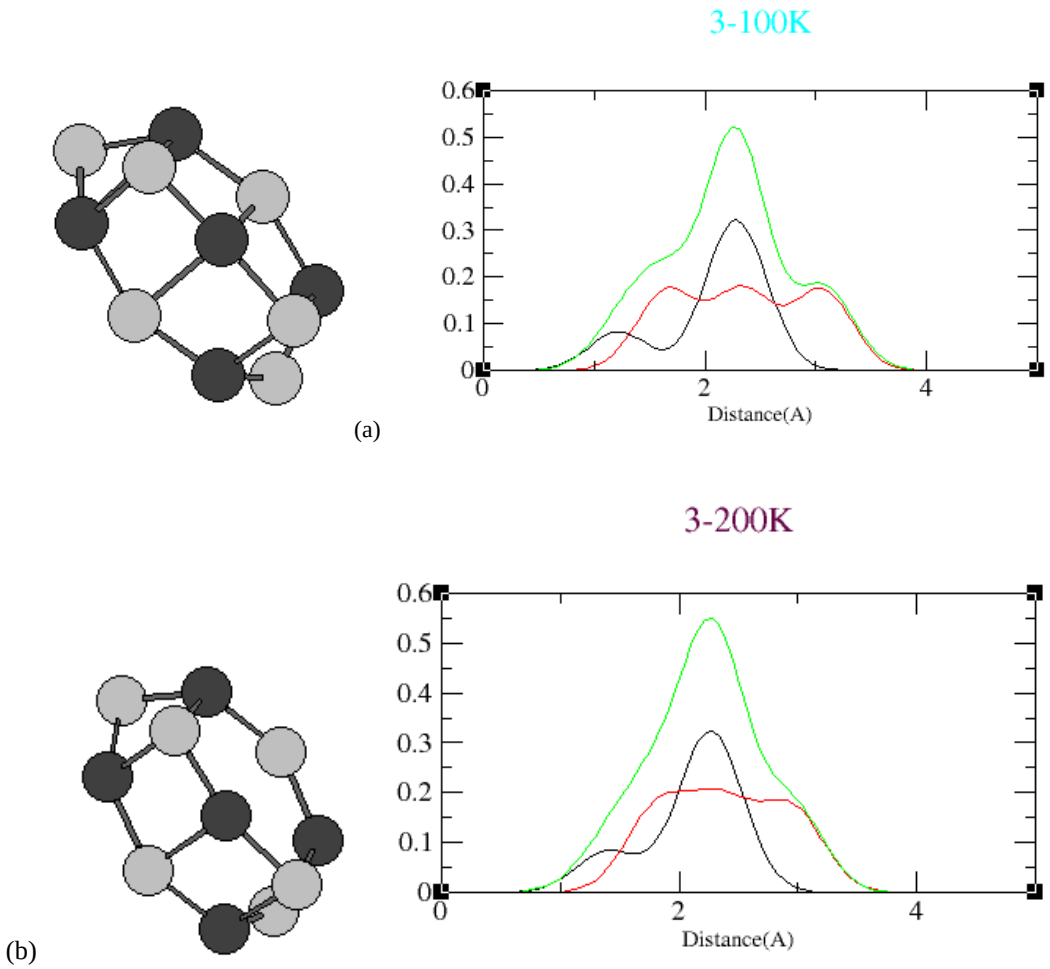


Figure 3. 12 (a) – (g) Relaxed structures of spherical nanoparticle with r= 3 Å, at temperatures 100 K to 900 K, and the related radial (atomic) distribution functions (RDF).

(c)

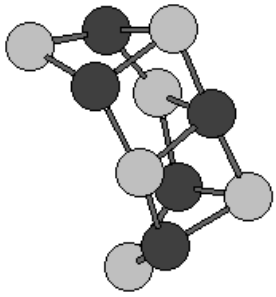

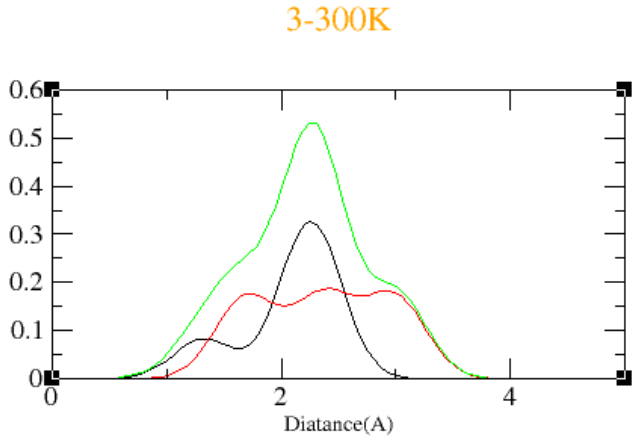


(d)

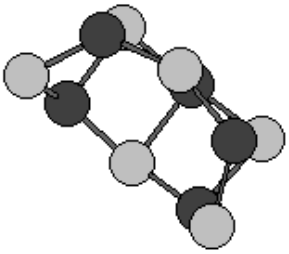

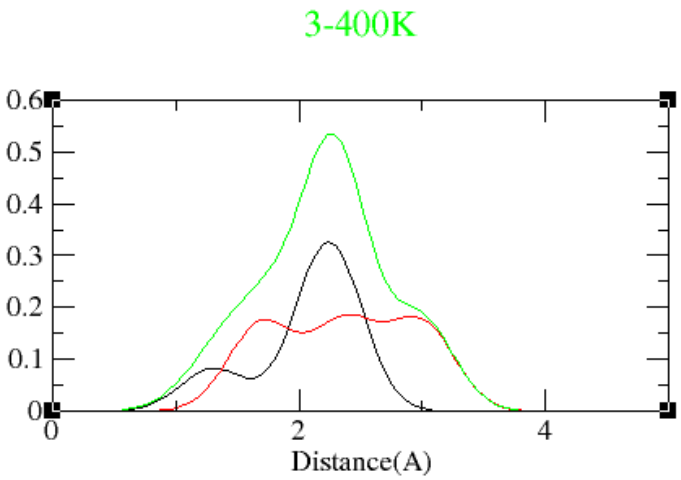


(e)

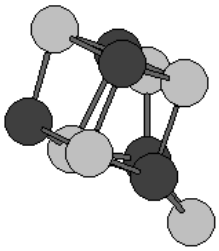

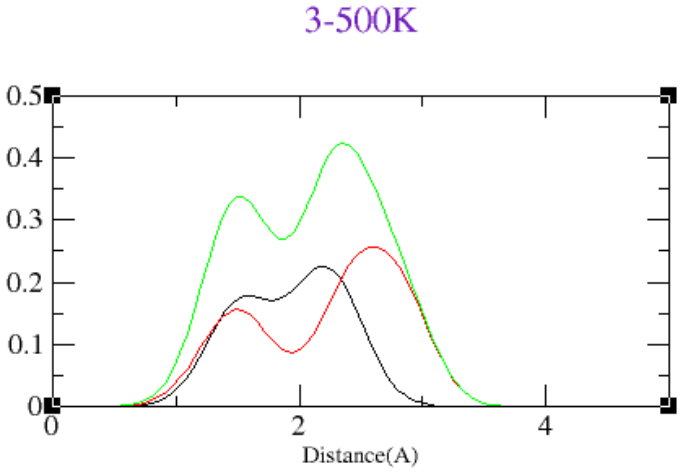


Figure 3.12 (continued)

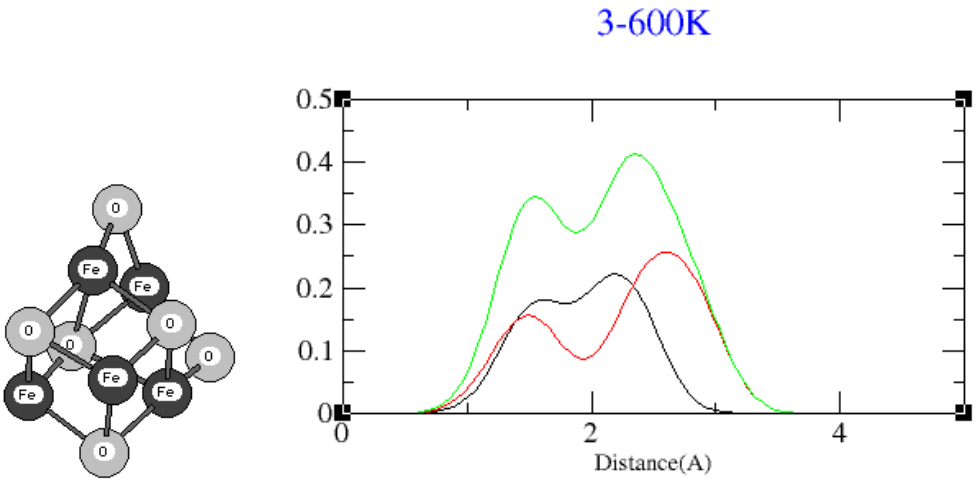


(f)

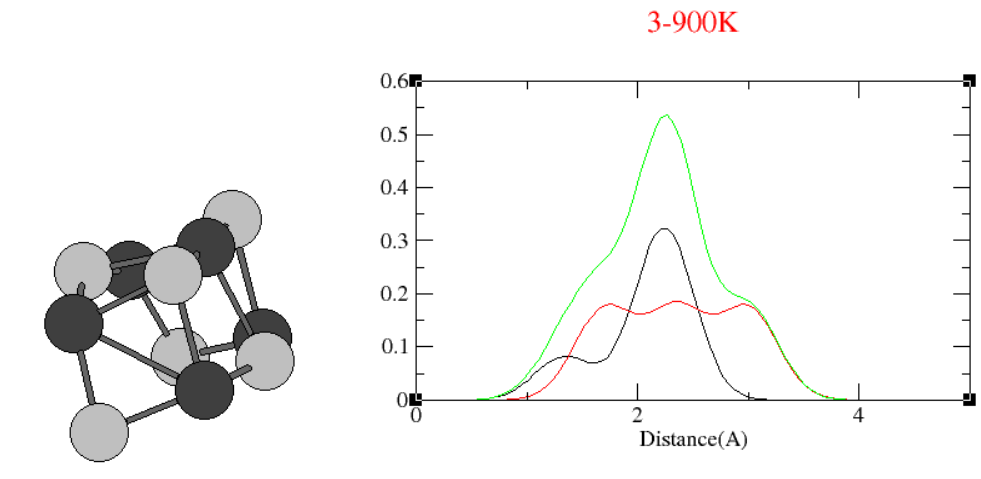


(g)

Figure 3.12 (continued)

and nanoparticle deformation gradually happens during temperature augmentation. At T=500 K and T= 600 K in the total curves (the green ones), instead of one peak, two peaks at different position are observed which illustrates that Fe and O atoms distribute in two different shells with respect to CM.

In Fig. 3.13, effect of temperature on the nanoparticles with r= 4 Å and radial or atomic distribution functions are presented. There is no significant deformation in this

nanoparticle and the structure is stable up to elevated temperature. Radial distribution functions for all simulation steps during temperature increment are similar.

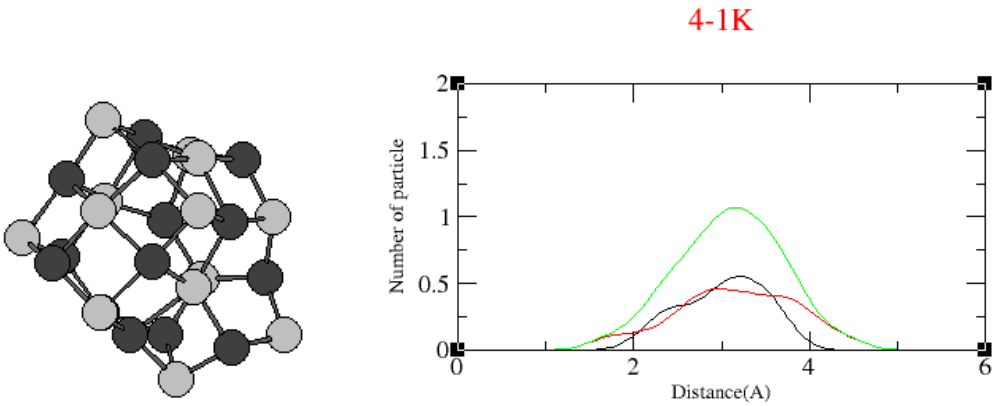


(a)

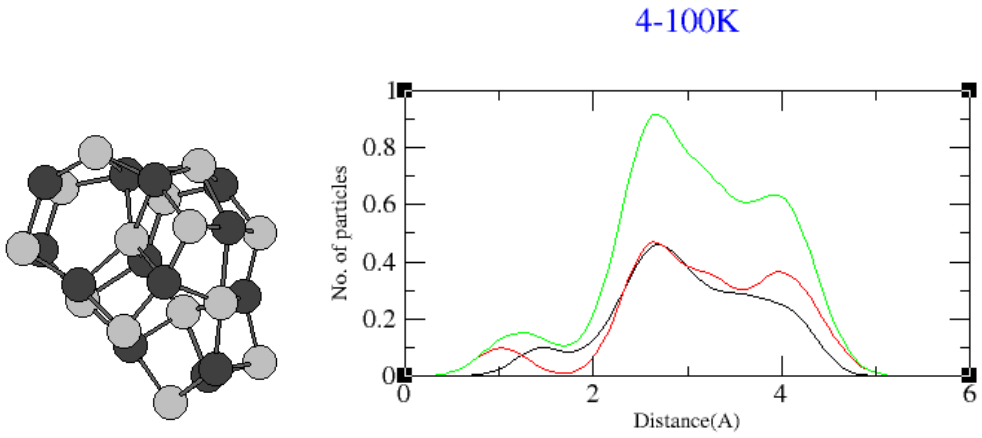


(b)

Figure 3. 13 Relaxed structures of spherical nanoparticle with radius 4 Å at temperature 1K to 900 K with interval 100 K.

(c)

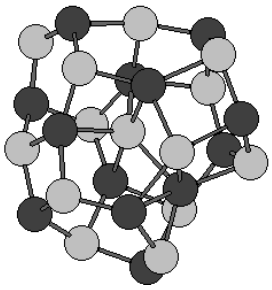

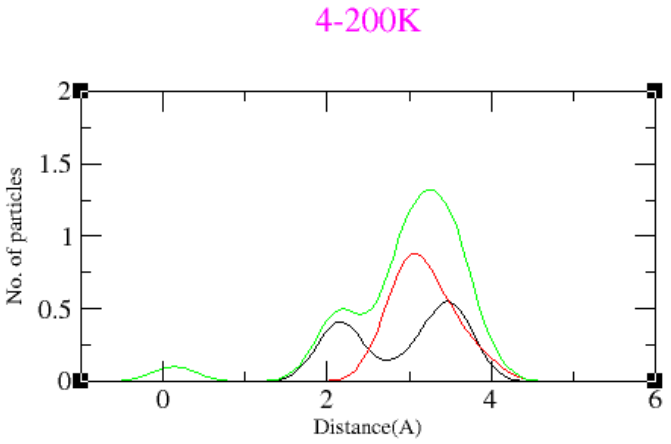


(d)

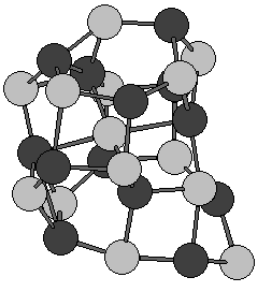

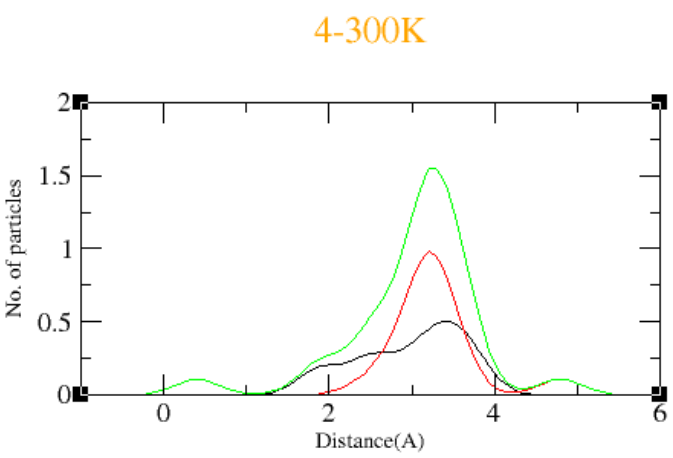


(e)

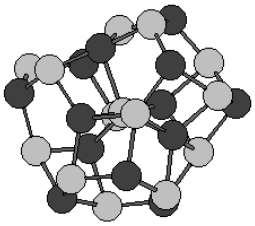

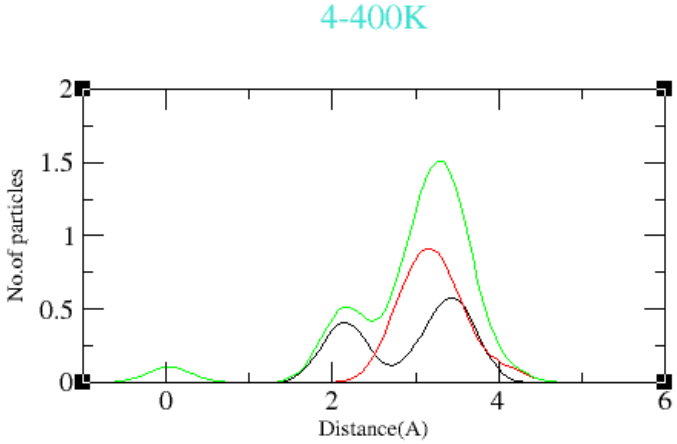


Figure 3.13 (continued)

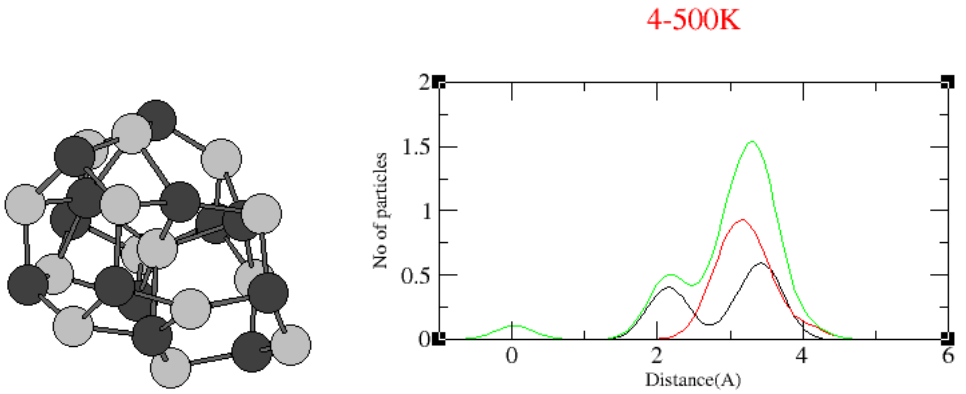


(f)

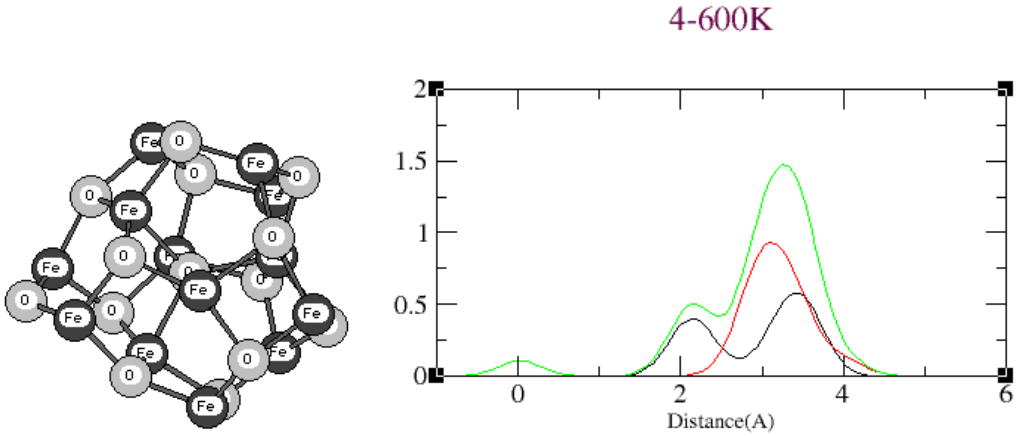


(g)

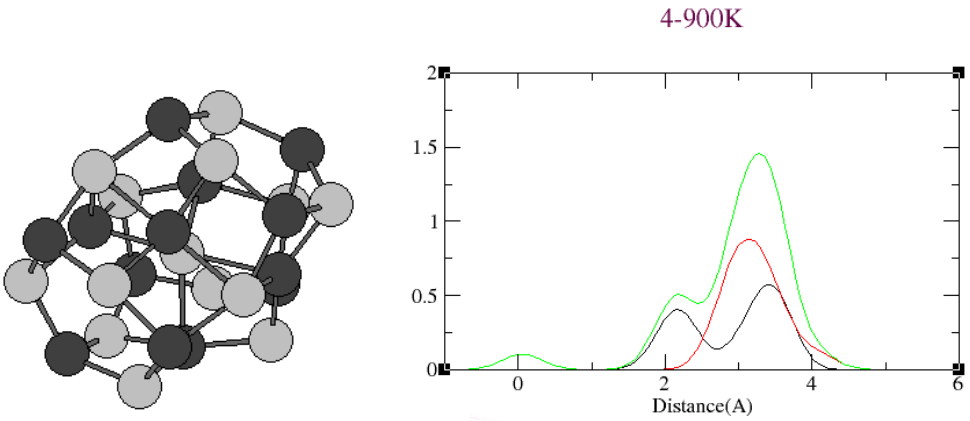


(h)

Figure 3.13 (continued)

The starting structure and the relaxed structures at various temperatures for the nanoparticles with r= 5 Å are displayed in Fig. 3.14. Structure and shape of this spherical nanoparticle transforms smoothly proportional to the gradient in the temperature. The nanoparticle keeps its initial form till 300 K. However, the structure of the nanoparticle starts to deviate from its well-arranged composition as the temperature increment steps progress.

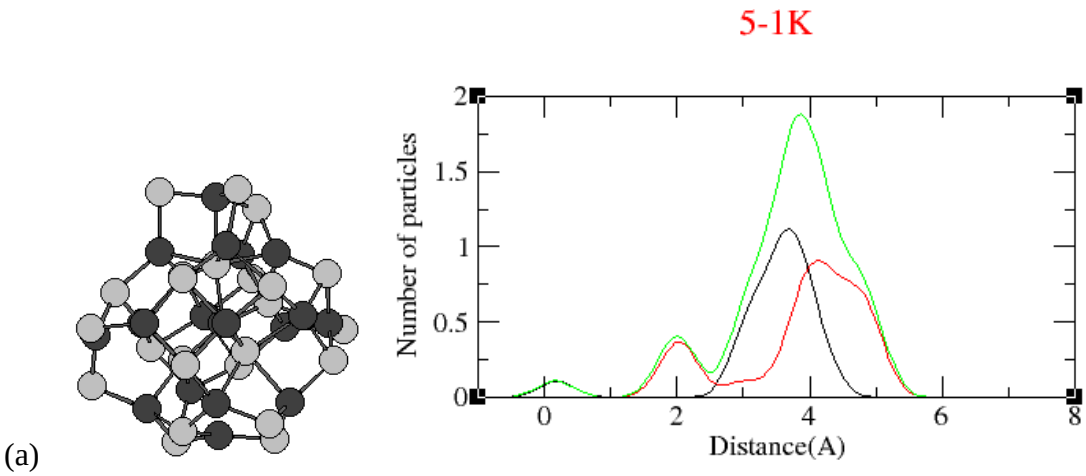


(a)

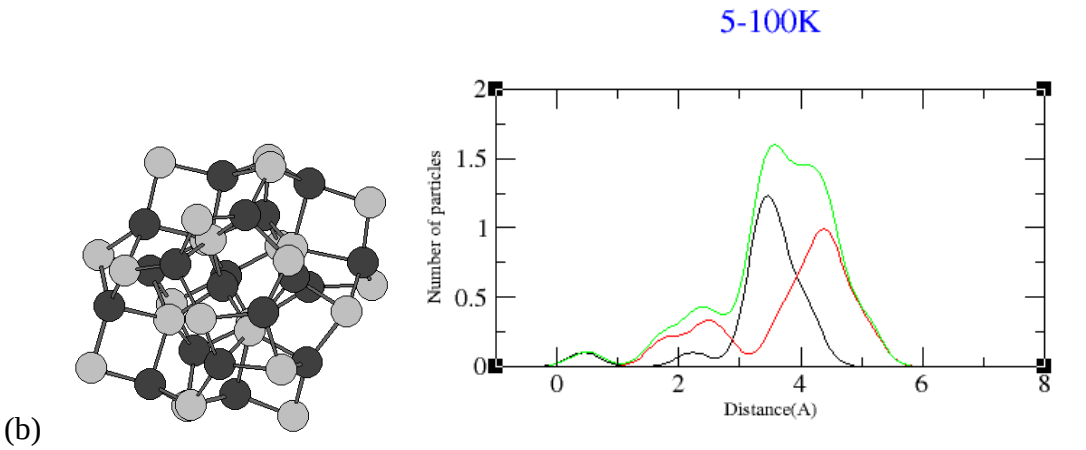


(b)

Figure 3. 14 Relaxed structures of spherical nanoparticle with radius 5 Å at temperature 1K to 900 K with interval 100 K.

(c)

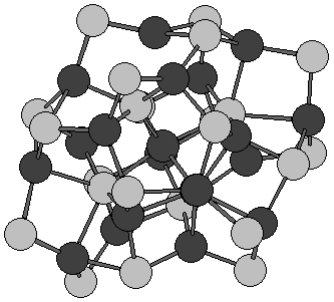

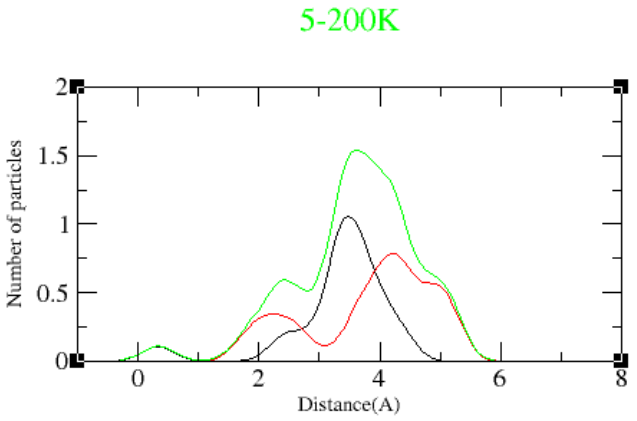


(d)

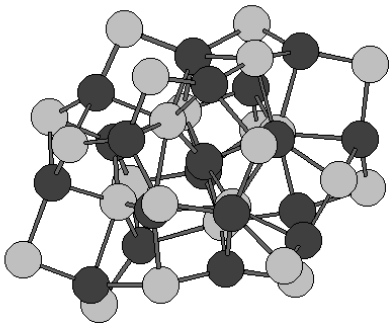

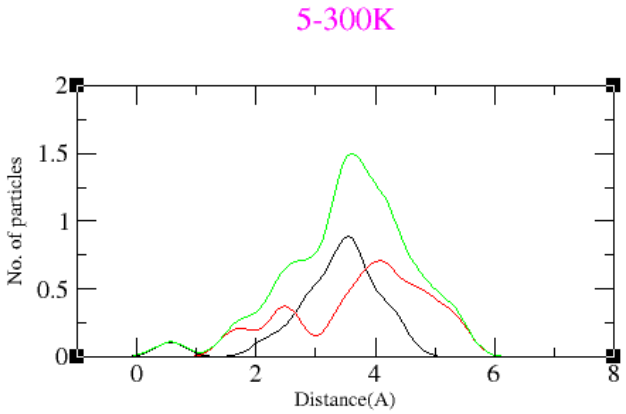


(e)

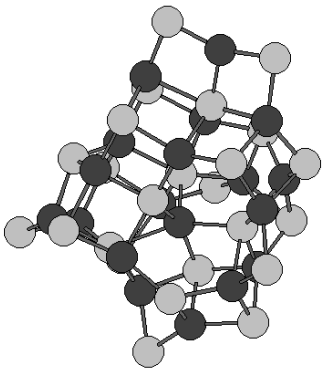

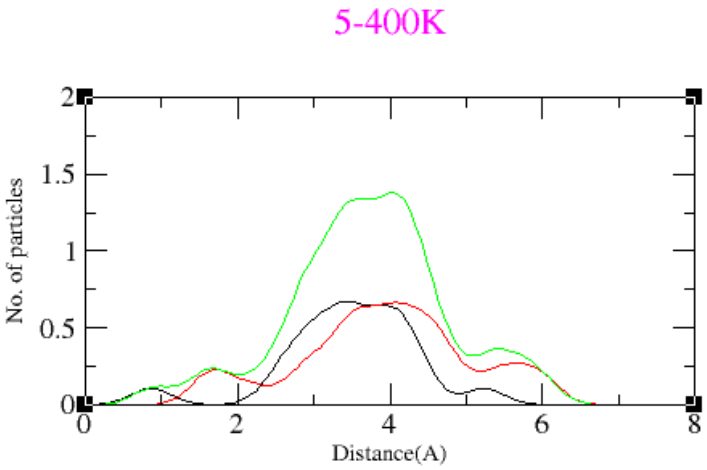


Figure 3.14 (continued)

(f)

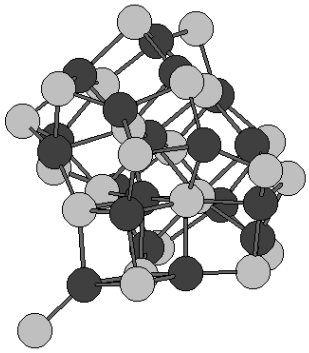

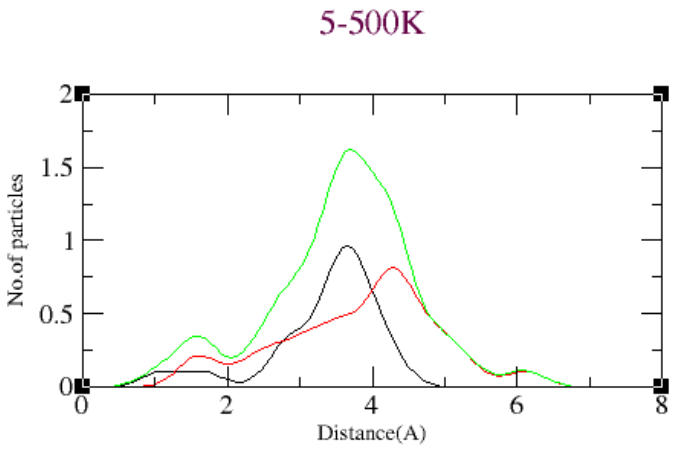


(g)

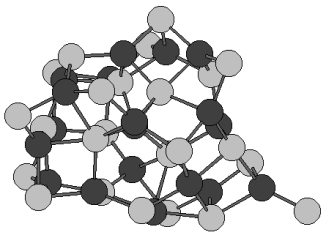

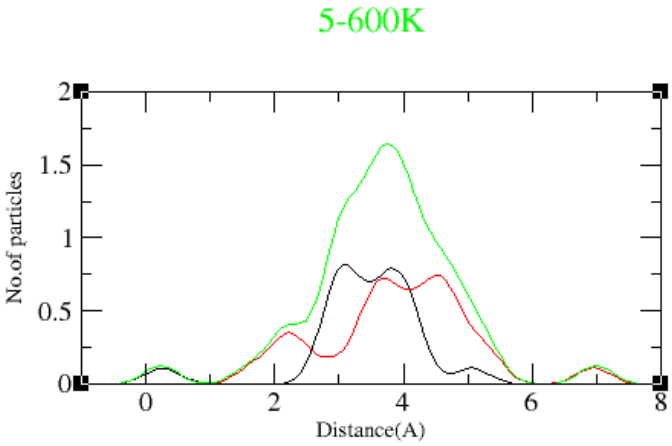


Figure 3.14 (continued)

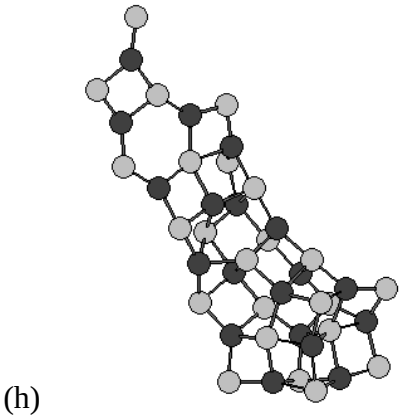

(h)

5-900K

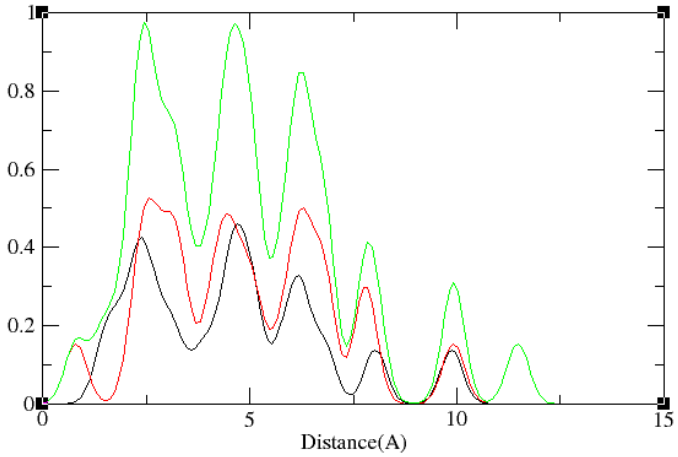


Figure 3.14 (continued)

It seems that nanoparticle at r= 5 Å is less resistive to heat treatment, sphere-like evolution occur at high temperatures and its shape changes to rod-like. The influence of temperature augmentation is seen to be significant on RDF for r= 5 Å, since it is seen two peaks in the total curve, which is related to shell construction. In T= 900K, the spherical structure disappeared completely and nanoparticle has converted to nanorod. In Fig. 3.15, calculation results for r= 6 Å are presented.

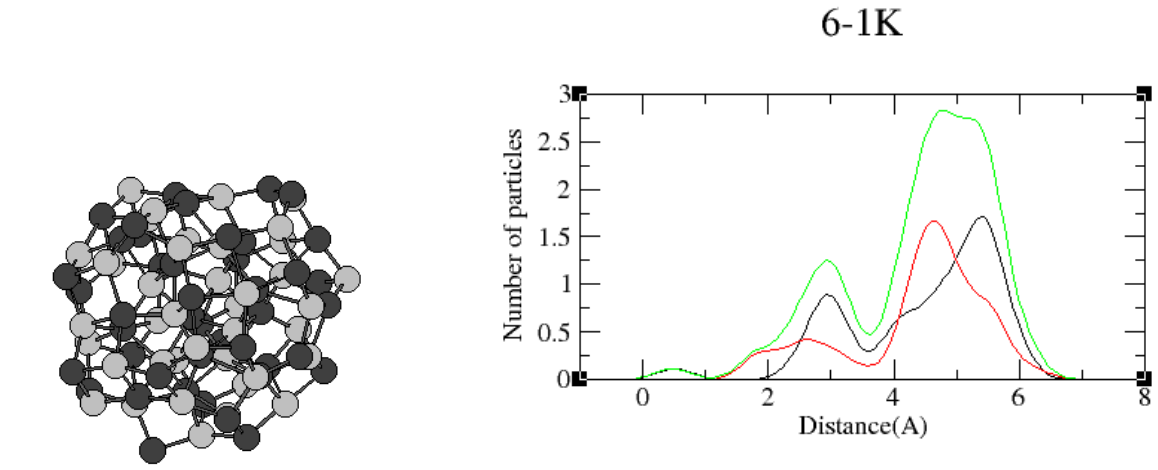


(a)

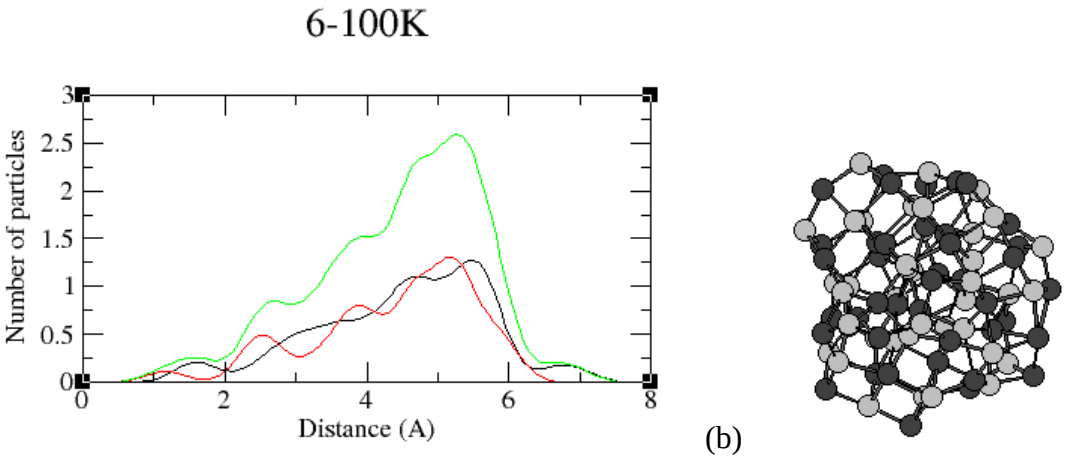


(b)

Figure 3. 15 Relaxed structures of spherical nanoparticle with radius 6 Å at temperature 1K to 900 K with interval 100 K.

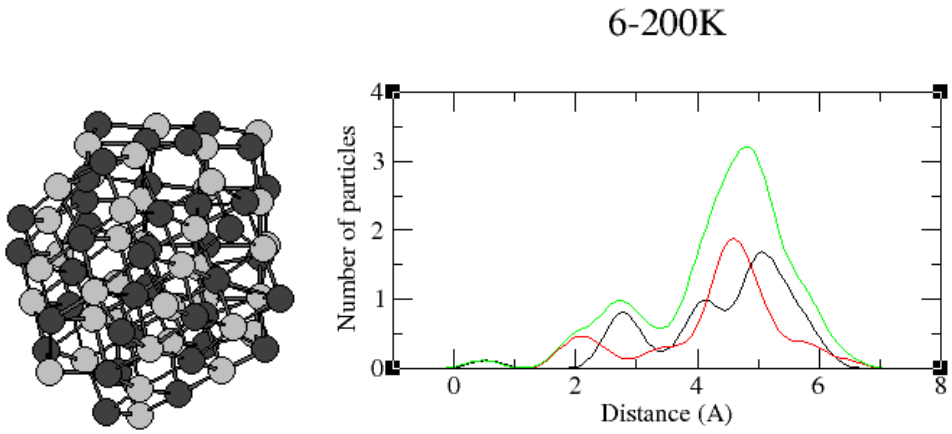


(c)

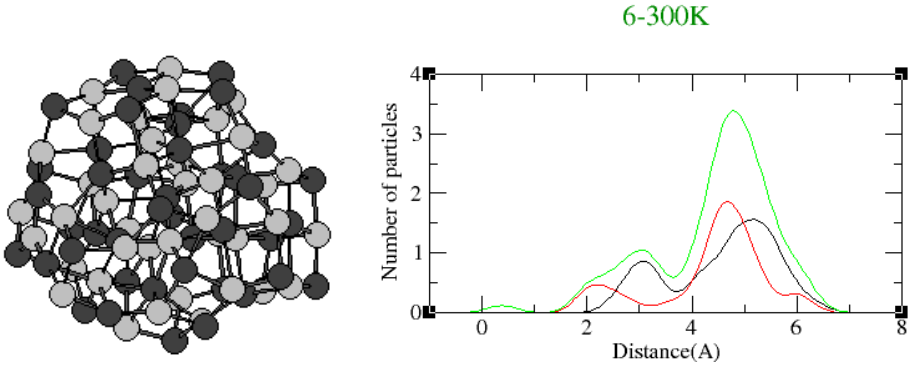


(d)

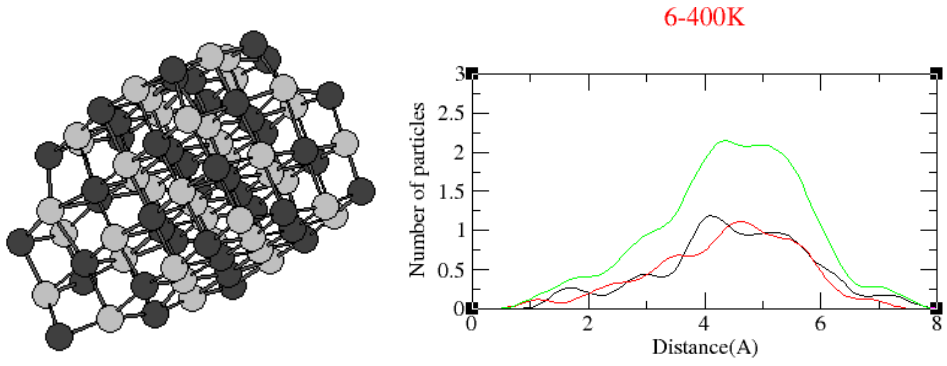


(e)

Figure 3.15 (continued)

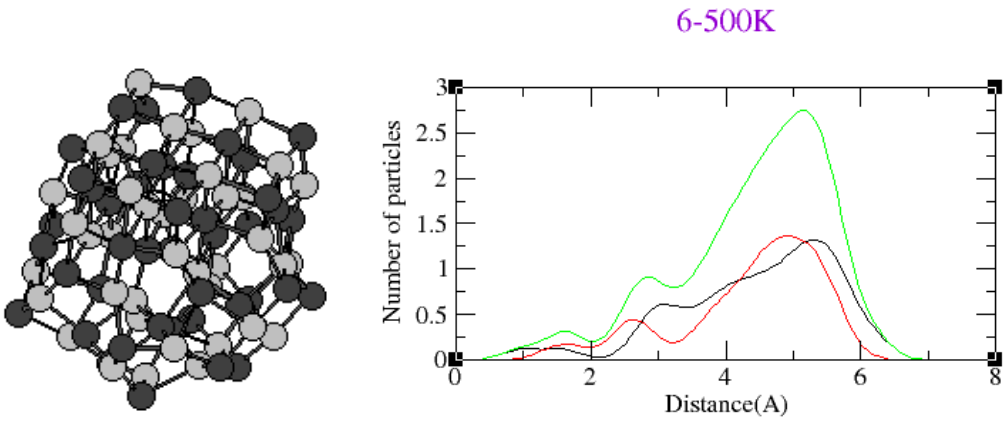


(f)

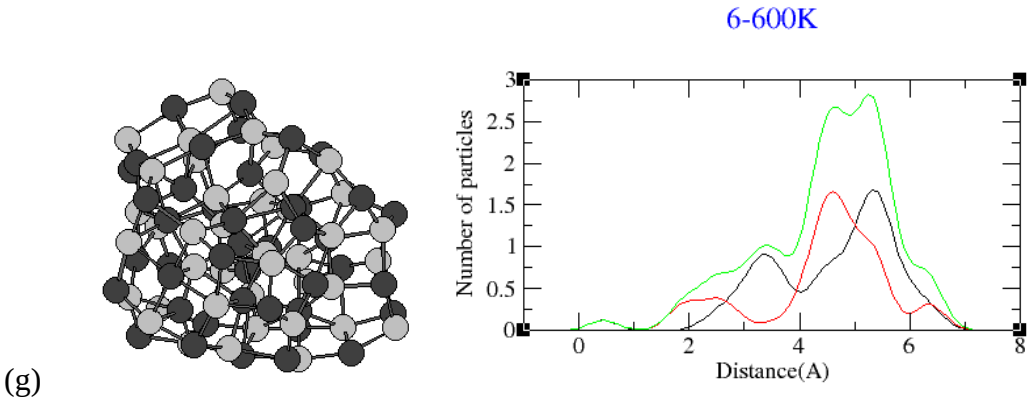


(g)

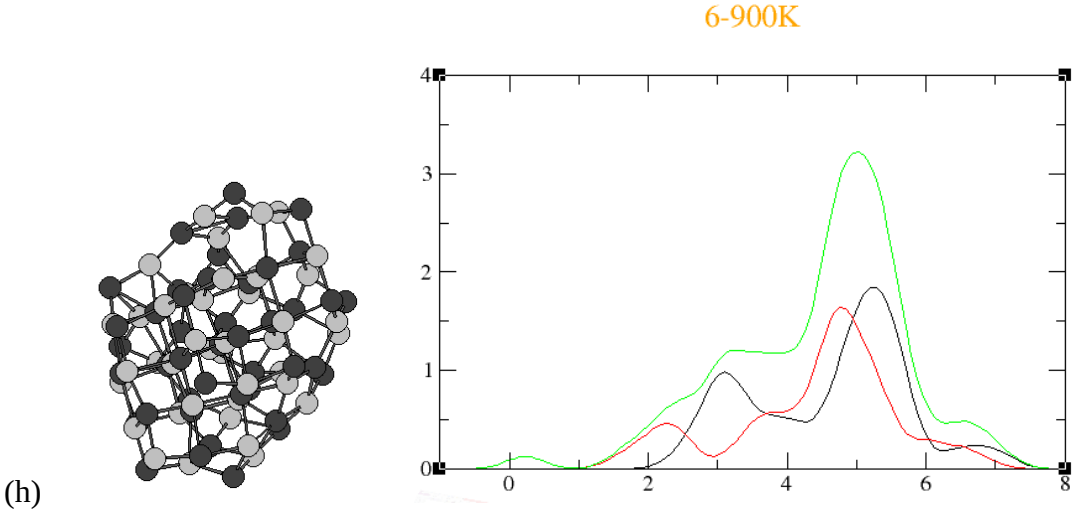


(h)

Figure 3.15 (continued)

According to Fig. 3.15, which show temperature effect on the structure evolution of nanoparticle with r= 6 Å, the results and behavior of nanoparticle seems to be similar to behavior of nanoparticle with r= 4 Å.

In summary, the following conclusions are drawn from this investigation. The oscillations in RDF graph provide a measure of the extent of spatial ordering of the atoms. In a disordered region, where there are no spatial correlations between atoms, RDF approaches the average density of the atoms for large r. However at each of temperatures and for all spheres, RDF of Fe atoms < RDF of O atoms, i.e. Fe atoms placed in inner shells near to CM.

As the particle size increases, the peaks corresponding to deformation part becomes broader, indicating that the larger particles take a longer time to deform. The study demonstrates that deformation in nanoparticles is not very rapid and nearly most of them withhold their original shape and structure.

## 3.3. Study of Electronic and Magnetic Properties of $(Fe_2O_3)_n$ Clusters: Using Density Functional Theory

### 3.3.1. Introduction

Considering aforesaid reasons, structural, magnetic, electrical, chemical and optical properties of nanoparticles are effected by shape and size factors. Since the geometry has significant effect on the various properties of a system, so understanding the relationship between the clusters and their properties is necessary. Generally cluster properties as a function of size do not follow simple scaling laws. Thinking over these aspects, many theoretical and experimental studies have been held during past decades in order to obtain a general understanding of how the properties depend on size, structure and composition of clusters. These small clusters are candidates for producing novel materials for technological applications such as optical storage devices, optical sensors, tele-communications magnetic storage and etc. [120-122].

Clusters are in the group of best candidates for realizing highly functional materials which cannot be attained even by present day technologies [123]. In this work, this special issue is being addressed and contains theoretical study of the iron oxide clusters which covers the determination of the structure of clusters and their electronic and magnetic properties.

Iron oxide clusters are one of the most debated atomic clusters which have attracted much interest due to their peculiar characteristics, diverse chemical and physical behaviors and also its close relevance with environmental corrosion and oxygen transport in biological system. Furthermore, in bulk phase, iron oxide compounds possess interesting magnetic properties. For instance FeO with rock salt structure shows antiferromagnetic ordering at low temperatures [124], $Fe_2O_3$ (hematite) with corundum structure is an antiferromagnetic material, while $Fe_3O_4$ (magnetite) has spinel structure and shows ferrimagnetic behavior [125]. The other theoretical concern relates to the evolution of physical, magnetic and electrical properties as material turns from bulk to cluster. Iron oxide clusters, similar to bulks, in different conditions show magnetic properties. Thus due to their significant potential applications, for example, in biomedicine, drug delivery, spintronics of semiconductors, high density magnetic moment storage and cancer therapy by hyperthermia [126-129], the interest on this peculiar magnetic property has been considerably enhanced.

Over the past decades, various theoretical and experimental works have been carried out in order to investigate the above-mentioned properties. In experiment, iron clusters were studied by photoelectron spectroscopy [130-133], infrared spectroscopy [134-136], Mössbauer spectroscopy [137] and different mass spectrometry based methods [127-139]. Most of the experimental and the theoretical calculations which are based on density functional theory and ab initio methods were concentrated on the small clusters.

In a theoretical study by Gutsev et al [140], electronic properties and structures of the ground and some excited states of the multi-oxide mono-iron clusters, i.e. $FeO_n$ and $FeO_n^-$ clusters ($n$ = 1–4), have been investigated within the density functional theory (DFT) formalism. Besides mentioned properties, electron affinities, vibrations and

thermo-dynamic stabilities have been studied in this survey. Due to their results, during increasing *n*, the spin multiplicity of the ground-state of iron oxide clusters decreases, i.e. ground states of $FeO^-$ and $FeO_2^-$ are quartets, while ground states of $FeO_3^-$ and $FeO_4^-$ are doublets. Various isomers with different spin and spatial symmetries belong to these anions [141]. Some theoretical findings which have been done by Jones et al. proved the existence of single hollow rings structures for equiatomic $Fe_nO_n$ (n=2-5) clusters against bulk FeO with the compact NaCl structure. For cases greater than n=5, clusters congregate to form more complex and new kinds of nanostructures [142]. Some specific studies have been performed in order to calculate vibrational and magnetic properties of magic clusters like $Fe_{13}O_8$ [143]. According to the results of all-electron density-functional-based calculations, one of the possible and stable structures for this cluster is the one by a central Fe atom and a distance of Fe-O relative to the central atom of 3.31 Å which is a ferromagnetic state with a total moment of $32\mu_B$ per cluster. Other several metastable ferro- and ferrimagnetic states with different total moments per cluster have been detected. In addition to mentioned above, Shiroishi et al. had studied some structural and magnetic properties of iron oxide clusters, $Fe_nO_m$ ($n = 1-5$) [144] and anion iron oxides [145,146] using first-principles calculations based on the density functional theory. They confirmed both the structures which have been suggested by Wang et al. [131] and also found that AFM Fe alignment increases as number of oxygen atoms grows at m=n for n=2,3, and 4. Furthermore, applying the same mentioned method and all-electron numerical basis sets, 40 stable isomers of $Fe_nO_m^+$ ($n + m = 5$) clusters have been found through optimization calculations and frequency analysis by B.-F. Xu et al [147]. Various quantities including the energy gaps between HOMO and LUMO, the binding energies and the magnetic moments of the stable isomers have been calculated. Results revealed the total magnetic moments of the isomers highly depend on the magnetic moments of Fe atoms and the arrangement of the magnetic moments of the atoms. In order to have contribution for theoretical perception of iron-oxide formation, López and co-workers [148] survey have been done for studying structural and electronic properties of some iron oxide clusters with various sizes between 33

and 113 atoms and two different space groups including the cubic $Fd3m$ and monoclinic $P2/c$ symmetries, using GGA+$U$ approximation. The low-temperature monoclinic phase of $P2/c$ symmetry seemed more stable than the others since its ground-state cohesive energy was smaller. These results have disclosed that inclination for keeping primary configuration increases for the larger clusters and also the primary optimizing phase of clusters has an important role in determining their electronic properties. Besides Radial and angular distribution functions unfolded that crystalline structures would tend to form cagelike structures after relaxation. By the way, during the production procedure, creating the clusters which are of close to one to one stoichiometry with proper amount of oxygen is possible too. Krisztián Palotásand and his co-workers performed spin-polarized density functional theory simulation within GGA and GGA+U approximation on different structures of nanometer-sized iron oxide atomic clusters with various stoichiometries. Total energies of structures and some collinear magnetic configurations were compared together and the results demonstrated that the structures with low symmetries and the ones which possess ferrimagnetic properties with low magnetic moment are energetically more desired in comparison to high symmetry structures. These researchers studied larger clusters like $Fe_{25}O_{30}$ and $Fe_{33}O_{32}$ and proposed cagelike geometry and rocksalt type structure for each of them, respectively. These calculations were based on GGA and GGA+U methods and considering the results for geometrical relaxations and physical properties, it was seen that remarkable difference occurs by switching from GGA to GGA+U. These results provide the evidence of sensitivity of the structure of transition metal oxide clusters to the exchange correlation energy functional used in the various methods [149]. One of the studies by Sheng-Gui He and co-workers [150] has been performed on cage and non-cage clusters of $(Fe_2O_3)_n$ [$n$ = 2–6, 10] using DFT calculations in order to compare bonding, stability and vibrational frequencies of miscellaneous kinds of structures.

Some other calculation on small iron oxide clusters [151] like, $Fe_2O$, $Fe_2O_2$, $Fe_2O_3$ and $Fe_3O_4$ displayed that the properties of iron oxide clusters strongly appertain to the valence states of iron. In bulk and clusters of iron oxide $Fe_2O_3$, iron atoms are in the

+3 valence state, these clusters with this feature and the stoichiometry of $(Fe_2O_3)_n$ , possess exclusive properties. Regarding these results, in general, it is concluded that doing experimental and theoretical study on the iron oxide $(Fe_2O_3)_n$ clusters is interesting and important.

Along the same line, using density functional theory, we shall investigate stable structures, electronic properties and the most outstanding characteristic feature, magnetic properties, of $(Fe_2O_3)_n$ ($n$ = 2–5) clusters with cage structure. As well as, we are interested in exploring the consequence of size evolution on the magnetic properties of the systems considered.

### 3.3.2. Computational Methods

Our calculations start with the structures for the cage clusters of $(F_2O_3)_n$, with $n$ = 2–5, which were adopted from the work of Sheng-Gui He and co-workers [150] and using Gaussview and Hyperchem softwares, also considering related symmetries, the mentioned cage structures were simulated . At the beginning, for each size of clusters, several initial geometrical structures have been considered and each cluster was optimized utilizing spin-unpolarized calculations. Each $(Fe_2O_3)_n$ cluster was placed in a cubic supercell configuration with a side length of 13.5 Å for $n$ = 1–3 and 16 Å for n=4,5 and enough vacuum space with duplications to avoid interactions between the cluster and its periodic images. Spin-polarized DFT calculations were performed using a plane-wave basis set implemented in the QUANTUM ESPRESSO package [152]. Exchange and correlation (XC) effects are treated within the local-density approximation (LDA) and core electrons are behaved explicitly by using Vanderbilt ultrasoft pseudopotentials [153] as supplied with the Perdew-Zunger (PZ) functional [154]. The KS wave functions expanded in a plane-wave basis set with a kinetic energy cutoff of 380 eV. Different values for the k-point sampling were tested and finally a grid of $5 \times 5 \times 5$ Monkhorst-Pack [155] k-points were used for the calculation of energy and density of states, while the structural relaxations were

performed using the gamma point only. Brillouin zone integration was performed by using the Gaussian smearing method with a width of 0.05 eV. To get the ground state magnetic moment, we have explicitly considered all possible spin configurations states (SCS's) for each cluster then these structures were relaxed and followed by the calculations of electronic and magnetic properties.

The total and absolute magnetizations which are achieved using scf calculations are defined as the integral of the magnetization in the cell and the integral of the absolute value of the magnetization in the cell, respectively:

$$\mu_{tot} = \quad (n_{up} - n_{down}) d^3 r \tag{3.6}$$

$$\mu_{abs} = \quad n_{up} - n_{down} \;\; d^3 r \tag{3.7}$$

where $n_{up}$ and $n_{down}$ are the atomic magnetic moments of atoms with a up and a down spin, respectively.

The relative stability of clusters was examined by calculating their (normalized) binding energies using the following equation:

$$E_b = E_n \;\; n - E_1 \tag{3.8}$$

where $E_n$ and $E_1$ are the energies of the $(Fe_2O_3)_n$ cluster and a single $Fe_2O_3$ molecule, respectively [156].

### 3.3.3. Results and Discussion

Relaxed structure for the rhombohedral unit cell of bulk hematite is displayed in Fig 3.16.

### 3.3.3.1. $Fe_2O_3$ Molecule (n = 1)

Figure 3.17 represents the optimized structure for an isolated $Fe_2O_3$ molecule, with $C_{2v}$ point group and the kite like shape. This structure, with two oxygen atoms at bridge sites and one oxygen at edge, has been obtained as the most stable structure for neutral $Fe_2O_3$ [157], as well as the charged forms, $Fe_2O_3^+$ [144] and $Fe_2O_3^-$ [147]. The calculated net magnetic moment for this molecule is 0.7 $\mu_B$ and the two Fe atoms have

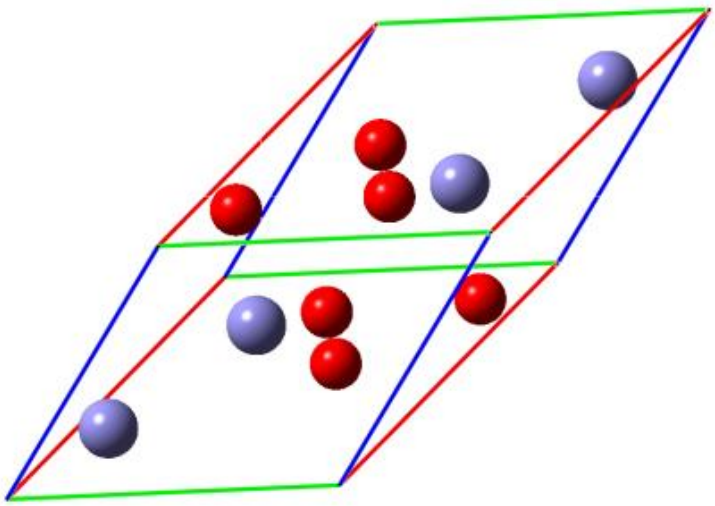

Figure 3. 16 Relaxed structure of the rhombohedral unit cell of hematite. Blue (Gray) color represents iron atoms and red (dark gray) represents oxygen atoms. We will follow the same convention throughout.

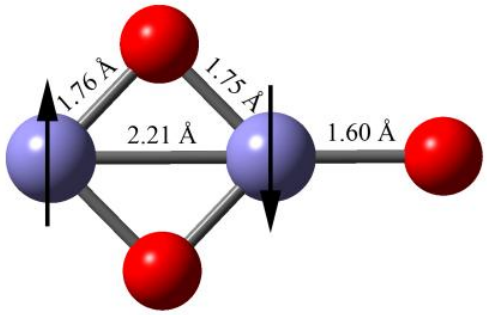


Figure 3. 17 Relaxed structure for the $(Fe_2O_3)_{n=1}$ cluster. The arrows show the spin polarization of Fe atoms.

opposite spin polarizations, in agreement with previous results [147,157]. The magnetization on O atoms does not appear in the figure due to their small values. Cheng and Li obtained similar ground state geometry for $Al_2O_3$ molecule [158].

### 3.3.3.2 $(Fe_2O_3)_{n=2}$ Cluster

The initial structure for $Fe_4O_6$ is shown in Fig. 3.18(a). The Fe-O bond length in the initial tetrahedral structure with $T_d$ point group is 1.89989 Å [150,156,157], the O–Fe–O and the Fe–O–Fe bond angles are 112.071º and 103.981º, respectively. The almost tetrahedral optimized structure of $Fe_4O_6$ cluster obtained in this study is represented in Fig. 3.18(b), the average Fe–O bond length is calculated as 1.69642 ± 0.00019 Å. In this structure, each O atom bonds with two Fe atoms and each Fe atom bonds with three O atoms, the calculated average bond angle for O-Fe-O is 116.075 ± 0.008º and for the bonds of oxygen atom with iron atoms, Fe–O–Fe, the average bond angle is 93.690 ± 0.014º.

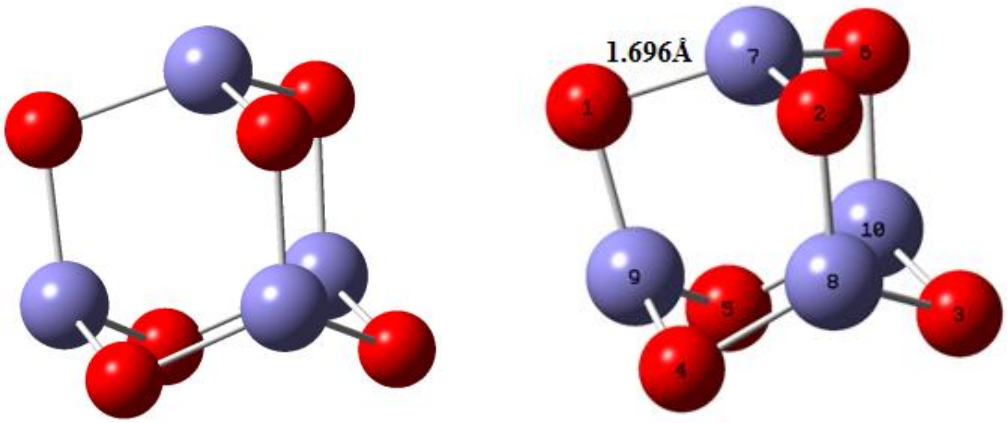


(a) (b)

Figure 3. 18 Initial structure for $(Fe_2O_3)_{n=2}$ cluster (a) and optimized structure for $(Fe_2O_3)_{n=2}$ (b).

It is clear that the optimization results are in accordance with previous studies [150,157]. For the relaxed structure, several spin configuration states were examined using different number of distinct Fe atom types with different starting magnetization values. Three distinct stable low-energy spin configuration states were found, for which the properties are given in Table 3.3. Furthermore, the values of atomic magnetic moments for Fe atoms of these three SCS's are shown in Figure 3.19, positive and negative numbers indicate spin-up and spin-down atoms, respectively. Considering atomic magnetic moments of Fe atoms (polarization values) in Table 3.5 and the optimized structures in Fig. 3.19, we will discern total and absolute magnetic moments, consequently the magnetic properties of these iron oxide clusters will be found (the magnetic moments for oxygen atoms are negligible and therefore are not shown). As complementary to our calculations for the sake of magnetic properties, Table 3.6 indicates some further properties obtained for three low-energy SCS's. The most stable spin configuration states, as well as their corresponding binding and the

Table 3. 3 Spin states obtained for $Fe_4O_6$ cluster (Refer to Fig. 3.18 for atom numbering). Atomic magnetic moments are represented in Bohr mag/cell [156].

| SCS | $\mu_{atomic}$ | | | |
|---|---|---|---|---|
| | **Fe7** | **Fe8** | **Fe9** | **Fe10** |
| n2-1 | -1.60 | 1.15 | 1.15 | 1.15 |
| n2-2 | 1.26 | 0.22 | 0.33 | 0.09 |
| n2-3 | -1.15 | 1.15 | -1.15 | 1.15 |

relative energies, bond length, total and absolute magnetic moments are given in Table 3.4. As it is seen, the most stable SCS (n2-1 state) with $C_{3v}$ point group has a ferrimagnetic arrangement of iron magnetic moments: three up, one down, which the total computed magnetic moment is 2.00 μB (Bohr magnetons) per cell, and the absolute is 5.53 μB per cell. The second SCS (n2-2) which has all four iron atoms lying in a majority spin and is relatively 0.055 eV higher in energy, is a ferromagnetic state with a point group closer to $C_{3v}$ (smaller standard deviation in bond lengths), but shorter Fe–O bonds. These two SCS's have been also obtained in previous calculations [156,159].

The good agreement between the calculated magnetic moments, geometries and magnetic properties with other theoretical and experimental data [150,159] proves the reliability of our theoretical approach. In this regard, we have used it further for extra insight into the magnetic and electronic properties of these systems. There is a third SCS (n2-3) has a perfect tetrahedral geometry and a zero total magnetic moment so anti-ferromagnetic spin ordering. As it is seen in Fig. 3.19(c), in this structure, two Fe atoms have positive and two have negative magnetic moments with equal values. In this present case, this tetrahedral kind of structure lies 0.084 eV higher.

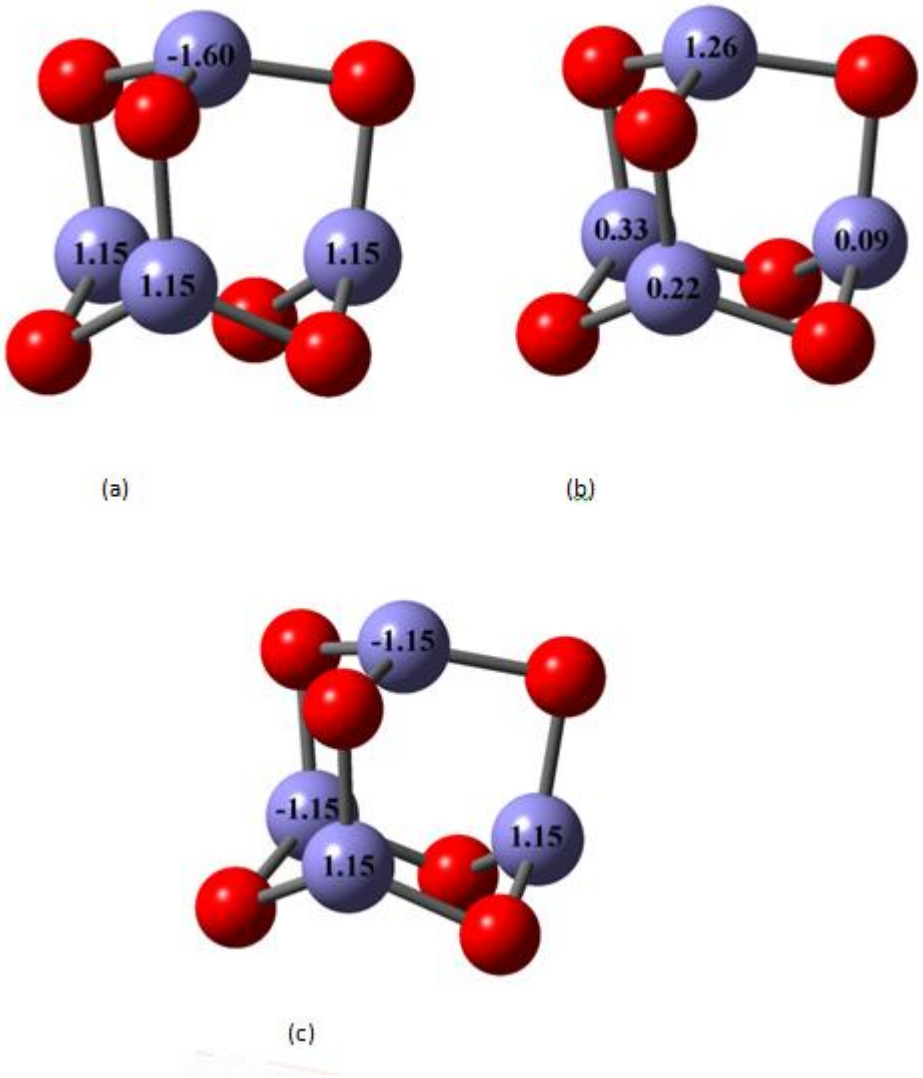


Figure 3. 19 The values of atomic magnetic moments for Fe atoms of three low-energy spin configuration states [156].

All these structures have same atomic arrangements but different spin configuration states, which is consequently the reason for their difference in magnetic moments and magnetic properties.

Inasmuch as, the binding energies for three SCS's of $Fe_4O_6$ are all negative, indicate that they are stable structures. The trend in $E_b$ values is similar to that of the relative

energies ($E_{rel}$ values). All bonds are longer than the bonds in spin-unpolarized relaxed structure shown in Figure 3.18b, but n2-1 and n2-3 have higher Fe–O bonds lengths. Meanwhile, it is relevant to get more insight into clusters and their properties, particularly the electronic structure and discuss them by calculating electron density of states (DOS). In this regard, density of states (DOS) plots for three SCS's of $(Fe_2O_3)_2$ are shown in Figure 3.20. As shown in this figure, energy is plotted in the range of -2 eV to 2 eV, since the magnetic properties are determined near the highest occupied level in DOS distribution, thus our concentration is in the vicinity of highest occupied level in DOS distribution and we set it as zero, i.e. we must first subtract the value of highest occupied level energy from all energy values in dos file, which is produced by the program, in order to set the zero of energy at the highest occupied level. As seen from Fig. 3.20, in some values of energy the density of state in majority-spin channel is different from the values in minority- spin channel. Hence, the n2-1 state shows a semiconductor behavior with a small gap of 0.2 eV in the majority-spin channel. The highest occupied level is mainly contributed by spin-up electrons. In the n2-2 state, the feature worth addressing is the crossing of the DOS at the highest occupied level, i.e. it shows a metallic behavior in spin-up direction whereas there is gap of ~1 eV for other population (spin-down direction) which makes it behaves as semiconductor.

Table 3. 4 Properties of three low-energy spin configuration states obtained for the $Fe_4O_6$ cluster [156].

| **SCS** | $E_{rel}$ **(eV)** | $E_b$ **(eV)** | $d_{Fe–O}$ **(Å)** | $\mu_{tot}$ | $\mu_{abs}$ |
|---|---|---|---|---|---|
| n2-1 | 0.000 | –3.71 | 1.706 ± 0.010 | 2.00 | 5.53 |
| n2-2 | 0.055 | –3.68 | 1.698 ± 0.005 | 2.00 | 2.21 |
| n2-3 | 0.084 | –3.67 | 1.706 ± 0.001 | 0.00 | 5.03 |

In conclusion, the n2-2 state is a half-metal. The n2-3 state is a semi-metal, with a negligible density of states at the highest occupied level, as yet there are two sharp

peaks just below and above it. The relative magnitude and disposition of the peaks are quite similar and simply are mirror images of one another [156].

### 3.3.3.3. $(Fe_2O_3)_{n=3}$ Cluster

Figure 3.21 (a) shows the initial relaxed structure of $Fe_6O_9$ with $D_{3h}$ symmetry. As it could be seen in this figure, there are two types of oxygen atoms in $Fe_6O_9$ cluster: oxygen atoms contributing in six-membered rings are labeled by $O_r$ , in the following figure oxygen atoms from O1 to O6, and oxygen atoms bridging between two 6-rings $O_b$ , the atoms which are tagged as O7, O8, O9 in Figure 3.21. The Fe–O bond lengths in the optimized structure for these two types of oxygens ($O_r$ and $O_b$) are 1.691 and 1.688 Å, respectively.

Turning to the question of energetic stability, we followed the same route for finding stable low-energy spin configuration states, thus we recognized three distinct SCS's.

The computed atomic magnetic moments of each of iron atoms for only two states are depicted in Table 3.7 and shown in Figure 3.22. In the n3-1 state, the atomic magnetic moments of the Fe10, Fe11, Fe13 and Fe14 are positive and the same, while for the Fe12 and Fe15, which have equal $\mu_{atomic,}$ are negative. These configuration results in an overall non-zero net magnetic moment. The complementary results are presented in Table 3.8 Comparing total and absolute magnetic moments, we deduce that the most stable state, n3-1 state is ferromagnetic, in which two Fe atoms have negative and four have positive magnetic moments. The total and absolute magnetic moments are 2.00 and 7.76 $\mu_B$ per cell. The iron atoms in the second stable state for $Fe_6O_9$ cluster, n3-2 state, still possess identical magnetic moments for the Fe10, Fe11, Fe13 and Fe14 but inverse spin alignment. The spins on the Fe12 and Fe15 are equal but antiparallel. These outcomes insinuate that n3-2 state is an anti-ferromagnetic spin ordering, in which three atoms are spin-up and three are spin-down and thus the total magnetic

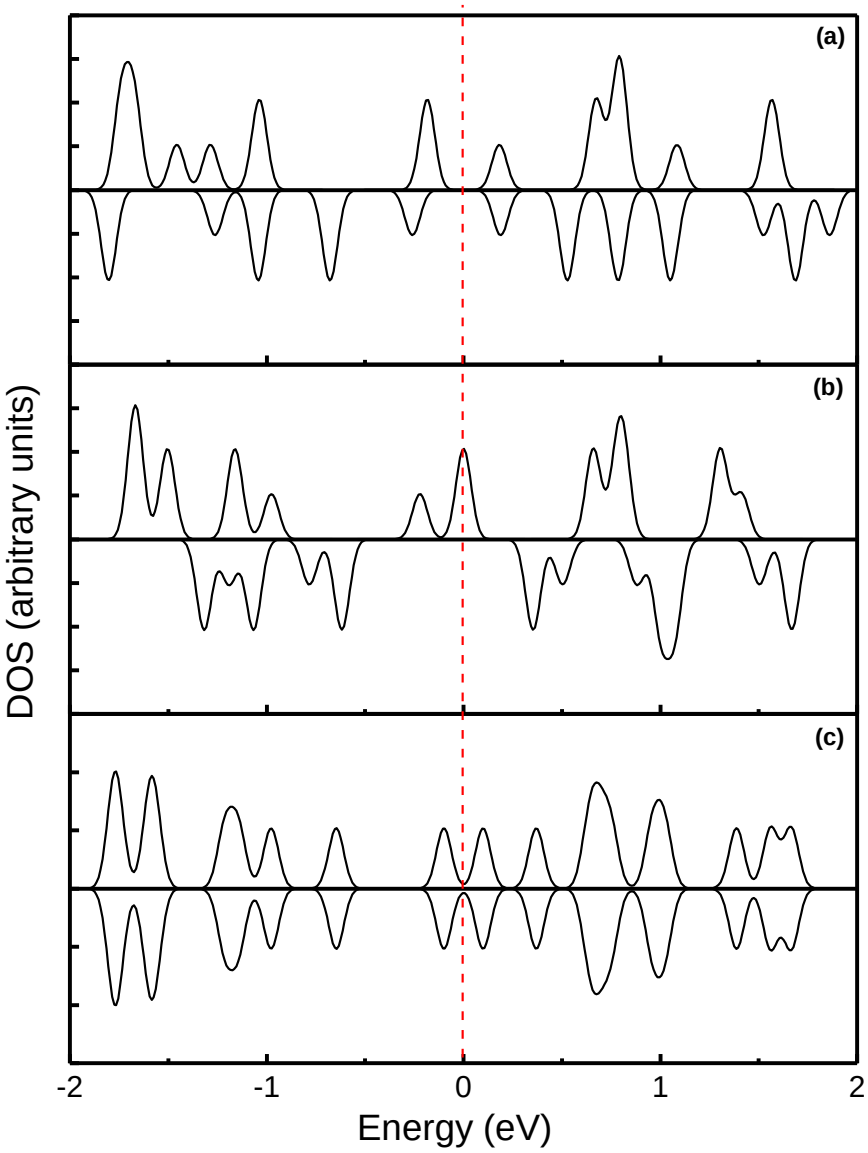


Figure 3. 20 Density of states (DOS) for n2-1 (a), n2-2 (b), and n2-3 (c) $Fe_4O_6$ clusters. Upper and lower panels are for spin-up and spin-down states, respectively. Zero energy indicates the position of the highest occupied level [156].

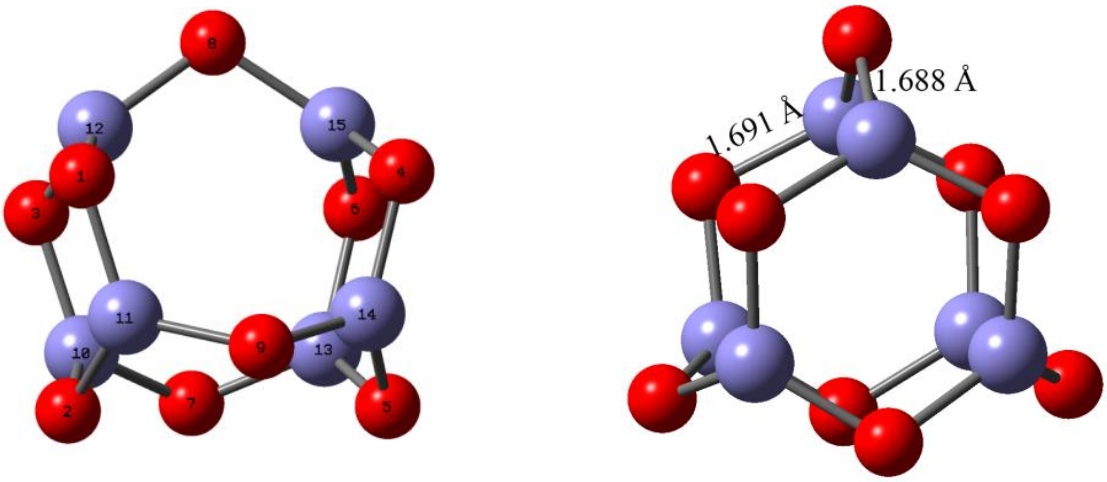


(a) (b)

Figure 3. 21 a) Relaxed structures for the $(Fe_2O_3)_n$ clusters with $n$ = 3. b) optimized structure, for each type of the optimized bond lengths ($Fe–O_r$ and $Fe–O_b$), one number is shown.

Table 3. 5 Stable spin configuration states and atomic magnetic moments of each Fe atoms for $Fe_6O_9$ cluster, atom numbering is shown in Fig. 3.21 [156].

| | $\mu_{atomic}$ | | | | | |
|---|---|---|---|---|---|---|
| **SCS** | **Fe10** | **Fe11** | **Fe12** | **Fe13** | **Fe14** | **Fe15** |
| n3-1 | 1.11 | 1.11 | -1.27 | 1.11 | 1.11 | -1.27 |
| n3-2 | -0.90 | 0.90 | -1.87 | -0.90 | 0.90 | 1.87 |

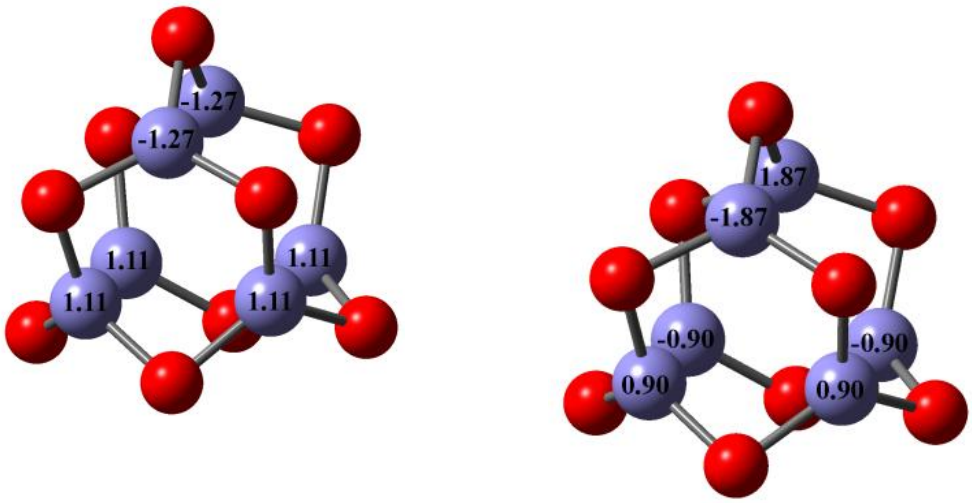


Figure 3. 22 The values of atomic magnetic moments for Fe atoms of the first two low- energy spin configuration states of $Fe_6O_9$ cluster.

Table 3. 6 Properties of three low-energy stable spin configuration states obtained for the $Fe_6O_9$ cluster [149].

| | | | $d_{Fe–O}$ (Å) | | | |
|---|---|---|---|---|---|---|
| **SCS** | $E_{rel}$ **(eV)** | $E_b$ **(eV)** | **Fe–O$_r$** | **Fe–O$_b$** | $\mu_{tot}$ | $\mu_{abs}$ |
| n3-1 | 0.000 | –4.44 | 1.695 ± 0.007 | 1.702 ± 0.005 | 2.00 | 7.76 |
| n3-2 | 0.263 | –4.36 | 1.698 ± 0.019 | 1.697 ± 0.007 | 0.00 | 8.09 |
| n3-3 | 0.332 | –4.33 | 1.689 ± 0.000 | 1.683 ± 0.000 | 0.00 | 0.00 |

moment is zero. The third state of $Fe_6O_9$ is the nonmagnetic state n3-3, the total and absolute magnetic moments both are zero. For the n3-1 state, we found less symmetric than the spin-unpolarized relaxed structure, with a point group near to $C_{2v}$ and elongated bonds. This configuration is energetically more favorable than the others. We observe that the bonds of iron atoms with oxygen atoms in rings, $Fe–O_r$ , with bond length 1.695±0.007 Å are shorter than $Fe–O_b$ bonds with bond length 1.702 ± 0.005 Å. The second stable state for $Fe_6O_9$, n3-2 state, has a less negative binding energy and lie 0.263 eV higher in total energy in comparison with the n3-1 state. In this optimal structure, $Fe–O_r$ and $Fe–O_b$ bonds are equal. The third state of $Fe_6O_9$ cluster, the nonmagnetic state n3-3, with $D_{3h}$ point group and the bond lengths very similar to the initial structure of Figure 3.21 (b) is found to have relative and binding energy 0.332 eV and -4.33 eV, respectively.

We give the total density of states (DOS) of the $Fe_6O_9$ cluster in Fig. 3.23. As can be seen from this figure, because of the spin-up peak below and a spin-down peak above the highest occupied level, the n3-1 is a semi-metal. It is visually obvious that, in the n3-2 state, the observed band gap is 0.2 eV. Furthermore, duo to the similarity between spin-up and spin down in DOS, this state is a semiconductor. The DOS plot for n3-3 in Figure 3c indicates that it is a semi-metal.

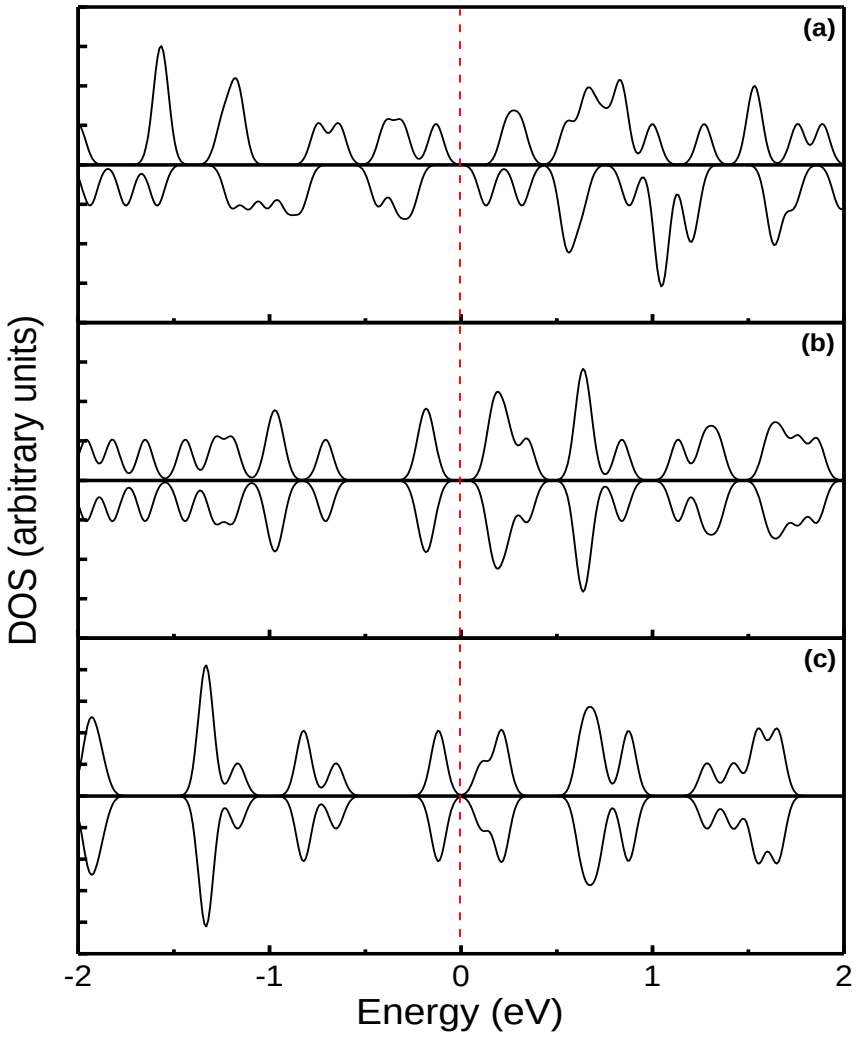


Figure 3. 23 Density of states (DOS) for n3-1 (a), n3-2 (b), and n3-3 (c) $Fe_6O_9$ clusters. Upper and lower panels are for spin-up and spin-down states, respectively.

### 3.3.3.4. $(Fe_2O_3)_{n=4}$ and $(Fe_2O_3)_{n=5}$ Clusters

As we observed during this study, the atomic magnetic moments of Fe and O atoms and their alignments in the cluster are responsible for the various total moments. The structures of clusters affect the magnetic moment of atoms, so they can either weaken

or strengthen each other and display different magnetic properties. Observing these points, we pursue our studying for recognizing properties of larger iron oxide clusters i.e. $Fe_8O_{12}$ and $Fe_{10}O_{15}$. In Fig. 3.24 the optimized structures for these two clusters are shown. The $Fe_8O_{12}$ cluster found to have octahedral symmetry ($O_h$ point group) with average Fe-O bond length of 1.682 Å which is identical for all Fe-O bonds. We give three proposed low energy spin configuration models for $Fe_8O_{12}$ cluster, which two of them are shown in Fig 3.25, the values on each of spheres relates to the atomic magnetic moments of iron atoms. We noticed that Fe atoms play main role on the total magnetic moment in previous clusters, and as expected in the following ones either. Summarized properties of three magnetic SCS's for $Fe_8O_{12}$ cluster are provided in Table 3.9 The spin arrangement of iron atoms shown in the Fig. 3.25 makes the state (n4-1) lower in total energy and contrasting zero net magnetic moment, $\mu_{tot}$, and absolute magnetic moment, $\mu_{abs}$, of 14.34 $\mu_B$ in this state, we conclude that (n4-1) state is an anti-ferromagnetic state, with the longest Fe–O bonds [156]. The n4-2 state is 0.133 eV higher in energy than n4-1, with two atoms having negative magnetic moments. Furthermore, like the state n4-1, one may also note that the $\mu_{tot}$ of 2.00 $\mu_B$, in table 4.4, is remarkably smaller than $\mu_{abs}$ of 11.74 $\mu_B$. Nevertheless, due to non-zero total magnetic moment in this spin configuration, this state exhibits ferrimagnetic property. The third magnetic moments configuration (n4-3) which have also been tested, led to approximately same total and absolute magnetic moments, thus $Fe_8O_{12}$ in the third state (n4-3) is ferromagnetic with atomic magnetic moment of 1.41 $\mu_B$ for all Fe atoms. It has an ordered $O_h$ point group and all its Fe–O bond lengths are equal.

As it is mentioned earlier, to hit the magnetic properties for these clusters, we have studied all possible spin configurations for $Fe_{10}O_{15}$ cluster. In Fig 3.24 (b), the optimized structure of $Fe_{10}O_{15}$ is depictured. Two magnetic states have been found for this cluster, one of these optimized structures is shown in Fig 3.26 Calculated relative energies, binding energies and magnetic moments are given in Table 3.10 [156].

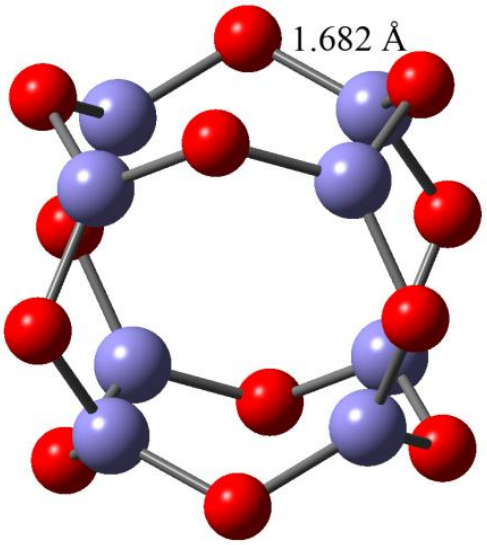


(a)

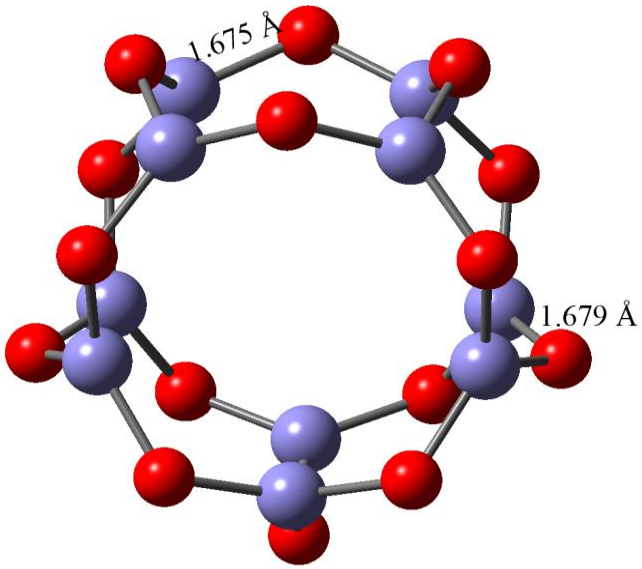


(b)

Figure 3. 24 Optimized structures for the $(Fe_2O_3)_n$ clusters with $n$ = 4 (a) and n=5 (b). For each type of the optimized bond lengths ($Fe–O_r$ and $Fe–O_b$), one number is shown.

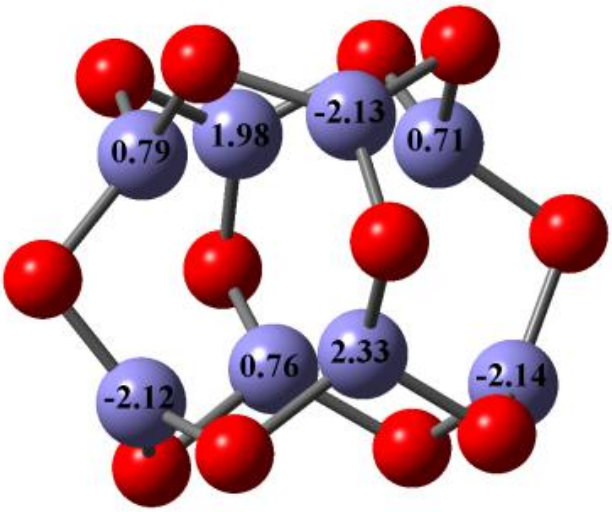


(a)

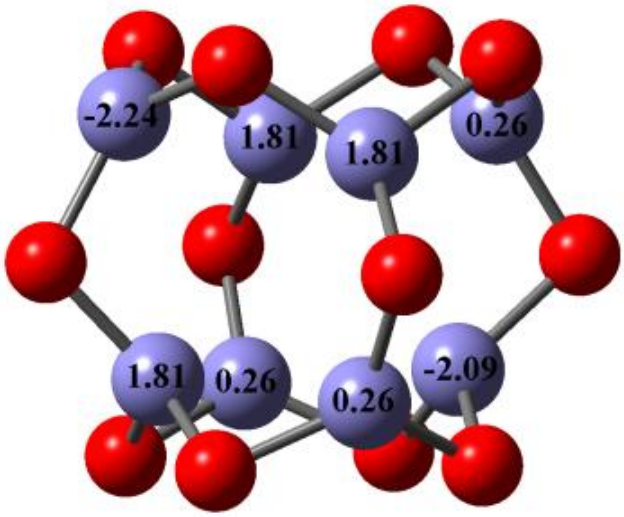


(b)

Figure 3. 25 The values of atomic magnetic moments for Fe atoms of the first low-energy spin configuration states of $Fe_8O_{12}$ cluster.

Table 3. 7 Properties of three low-energy stable spin configuration states obtained for the $Fe_8O_{12}$ cluster.

| SCS | $E_{rel}$ (eV) | $E_b$ (eV) | $d_{Fe-O}$ (Å) | $\mu_{tot}$ | $\mu_{abs}$ |
|---|---|---|---|---|---|
| n4-1 | 0.000 | –4.72 | 1.703 ± 0.035 | 0.00 | 14.34 |
| n4-2 | 0.133 | –4.68 | 1.697 ± 0.028 | 2.00 | 11.74 |
| n4-3 | 0.234 | –4.66 | 1.698 ± 0.000 | 12.00 | 12.26 |

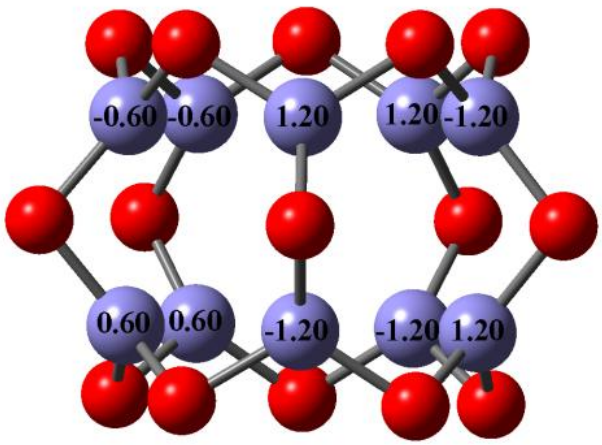


Figure 3. 26 The values of atomic magnetic moments for Fe atoms of the two low-energy spin configuration states of $Fe_{10}O_{15}$ cluster.

The lower energy state (n5-1) is anti-ferromagnetic and the higher energy state (n5-2) is nonmagnetic. These properties arise for the following reasons. As it is seen in the

Fig 3.26, the majority and minority spins summation which constructs the total magnetic moment is zero, while the absolute magnetic moment is 10.96 $\mu_B$. These types of spin configurations give rise to anti-ferromagnetic property of this cluster in the (n5-1) state. Table 3.10 shows an overall decrease in magnetic moments in (n5-2) state which we educe that this state exhibits no magnetic sign. Both of these two states have $D_{5h}$ point group, but it should be pointed out that bond lengths are larger than the spin-unpolarized relaxed structure of Figure 3.24 (b). The overall look of these results anticipates the trend that: binding energy grows monotonically with increasing the cluster size, the highest value is thus found for $Fe_{10}O_{15}$ cluster [156].

Table 3. 8 Properties of three low-energy stable spin configuration states obtained for the $Fe_{10}O_{15}$ cluster.

| | | | $d_{Fe-O}$ (Å) | | | |
|---|---|---|---|---|---|---|
| **SCS** | $E_{rel}$ **(eV)** | $E_b$ **(eV)** | **Fe–O$_r$** | **Fe–O$_b$** | $\mu_{tot}$ | $\mu_{abs}$ |
| n5-1 | 0.000 | –4.71 | 1.672 ± 0.000 | 1.685 ± 0.013 | 0.00 | 10.96 |
| n5-2 | 0.096 | –4.69 | 1.680 ± 0.000 | 1.691 ± 0.006 | 0.00 | 0.00 |

In Fig 3.27 and Fig. 3.28, we present the DOS for majority and minority spin generated from the $Fe_8O_{12}$ and $Fe_{10}O_{15}$ cluster calculations. As it is clear in Fig 3.27(a), howbeit state n4-1 has a net zero magnetization, the DOS plots for the majority and minority spins are different. In this figure for spin-up DOS, we comprehend that it behaves like semiconductor, whiles spin-down DOS has a nonzero value at the highest occupied level, so in this case it is metal, whereupon, it is a half-metallic antiferromagnet [40], which make the $Fe_8O_{12}$ cluster in state (n4-1) as a leading material for spintronics applications [161].

Generally half-metallic antiferromagnets differ from common antiferromagnets. They are the proper subset of stoichiometric half metals which the integer moment per cell is zero. These materials were foretoken to represent an anomalous form of magnetism. [161,163].

It should be mentioned that according to the Coey et al. [164] classification of half-metallic ferromagnets, there are four types of half-metals, our case is the type-$I_B$ half-metals, which is semiconducting with respect to majority spin and metallic with respect to the minority spins.

As it is considered in Fig. 3.27 (b) and (c), the n4-2 and n4-3 states are both half-metals. In Fig. 3.28 we present the DOS both two spin configuration states which have been found for $Fe_{10}O_{15}$ cluster [156].

The DOS for majority-spin states are shown in the upper panel and the minority-spin ones are located in lower panels. Regarding these graphs, the outcome is that both of these structures are semiconductors, with have the same spin-up and spin-down DOS plots [156].

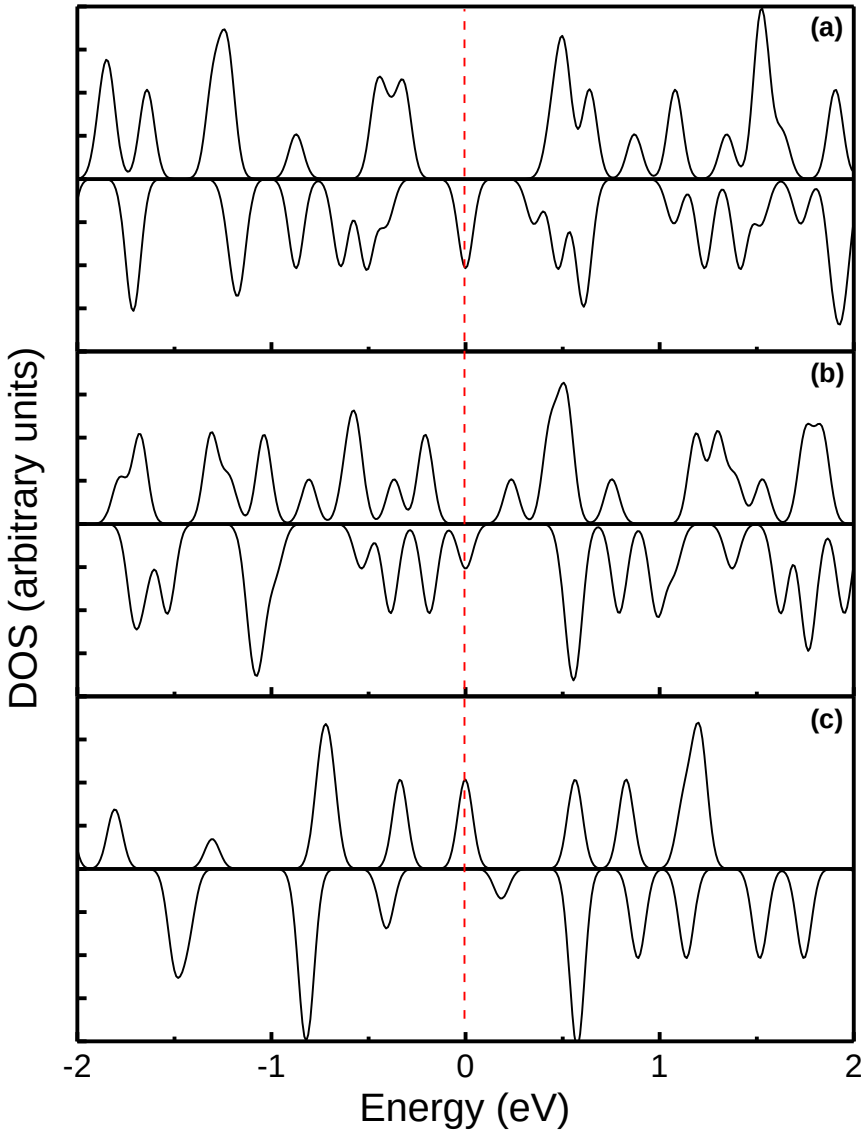


Figure 3. 27 Density of states (DOS) for n4-1 (a), n4-2 (b), and n4-3 (c) $Fe_8O_{12}$ clusters. Upper and lower panels are for spin-up and spin-down states, respectively.

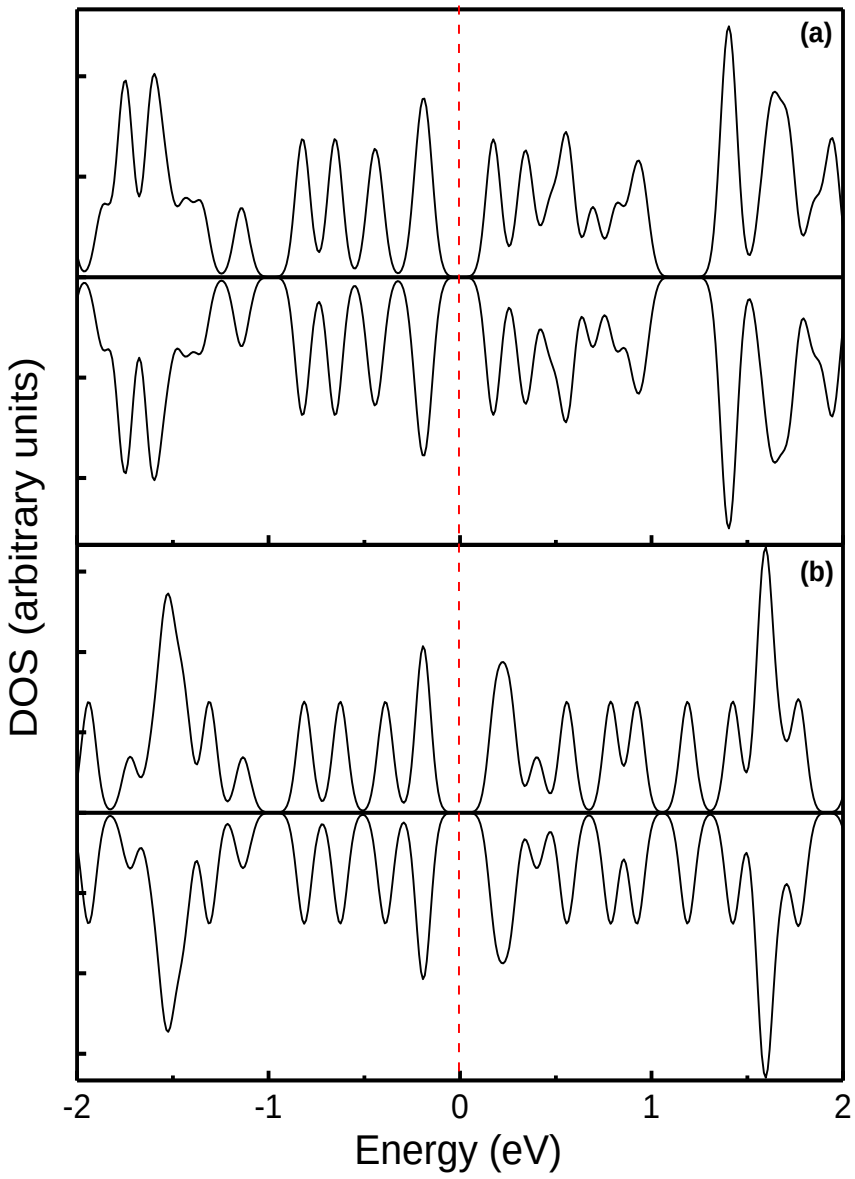


Figure 3. 28 Density of states (DOS) for n5-1 (a) and n5-2 (b) $Fe_{10}O_{15}$ clusters. Upper and lower panels are for spin-up and spin-down states, respectively.

## 3.4. Study of the Influence of Transition Metal Atoms on Electronic and Magnetic Properties of Graphyne Nanotubes Using Density Functional Theory

### 3.4.1. Introduction

As mentioned in the first chapter, since graphyne nanostructures are applicable in novel technology in various forms, thus many studies and researches have been done for recognizing their properties. Ivanovskii has reviewed the theoretical and experimental studies on graphyne in various zero-to three-dimensional nanostructures [52], since these compounds have many potential applications in lithium batteries [165,166], electronic devices and Hydrogen storage media [167] and as a membrane in gas separation [168,169]. They can also be doped in polymeric materials or composites for use in solar cells [170]. Narita, et al. [51] have studied the electronic and structural properties of graphyne compounds using the linear combination of atomic orbitals (LCAO) in LDA approximation. According to their results graphyne is a semiconducting material with a direct band gap of 0.52 eV at the M point.

By the way, theoretical studies indicate that in comparison between graphyne and graphdiyne, the former is more favorable because of its stability and expected to be produced experimentally in future. Remarkable attempts have been allocated to the electronic structure and other properties of graphyne [47, 53, 171-176]. Tongay and co-workers [177], using first-principle plane wave calculation, have proposed different stable periodic structures which contain carbon atomic chains in 1D, 2D and 3D. The more cognizance of stability of graphyne under various conditions is a challenging issue in order to synthesize it experimentally and produce related nanodevices. One of the surveys, on the basis of first-principle method, has been performed for studying the stability and structural transformation of 2D α-graphynes at different sizes [178]. According to another theoretical report [179] based on first-principles method, in comparison between graphyne and graphene, the latter is more stable, since its binding energy is 0.56 eV higher per atom. Consequently, it is still debatable that how long graphyne can exist at high temperatures and in what condition it turns into graphene.

For auspicating lifetime or stability of nanodevices particularly graphene-based devices, Lin and his teammates has proposed a statistic model based on ab- initio calculations [180-181], using this model, Yi-Guo Xu and et al. tried to foretell the change rate of stability of α-, β- and 6,6,12-graphyne with the temperature variation. Their research showed that free-standing single layers of these kinds of graphynes and graphdiyne are stable in the range of room temperature to 1000K, but the conversion from graphyne to graphene happen when the temperature is about 2000K and more [182]. Zhou and et al. [172] have analyzed the electronic structure and bonding of graphyne and its boron nitride analog using density functional theory for the purpose of better understanding of brand-new carbon-based structures. They found that modifying the length of carbon chain and size of hexagonal ring; can modulate the direct bandgap of both of these structures, which is useful for energy band engineering.

As discussed before, during recent years, graphyne, owing to its electronic applications, has been contemplated as competitor of graphene. Since, in contrast to graphene, most of fields like electronic and optical properties or magneto-transport of graphyne are not completely detected yet, Zhe Liu and et al. using a π-electronic tight-binding method, have proposed an effective model which is in good agreement with DFT results for the valence and conduction bands and some features of α-,β-,γ- and (6,6,12) graphyne [183].

In order to find out more about the electronic properties, other theoretical studies have been done on graphyne families. Malko et al. [171] have noticed Dirac cones exist in two-dimensional α-graphyne and other graphyne sheets and proved that these cones are not unique characteristic of graphene and these Dirac-cone like features are not limited to honeycomb structure or hexagonal symmetry and may be seen in other two-dimensional structures either.

Furthermore, several tight-binding and DFT studies have been employed for investigating the electronic and mechanical properties of graphyne-based nanotubes (GNTs) for various forms of graphyne [174-176]. Colucia and his co-workers have generated GNTs from graphite-based nanotubes and using tight-binding calculations,

predicted the electromechanical reaction of these semiconducting nanotubes to charge injection. According to their research, the bandgap of GNTs does not depend on the diameter and chirality of nanotubes and are the same for all possible geometries.

Tuning pristine graphyne structure is of great importance in order to modifying its intrinsic properties recently. Studying the adsorption of 3d atoms on graphyne and graphdiyne sheets showed that not only are the electronic properties affected, but also the magnetization of these sheets are increased under this circumstance, as an example, Fe-graphyne behaved as a magnetic metal [184]. The reason of this alteration in magnetic property originates from the charge transfer between graphyne and graphdiyne sheets and transition metal atoms. These properties are important for spintronics applications.

In another similar research, this group applied density functional plus Hubbard approach and have developed a model for disclosing some principles for Half-Metallicity in transition metal doped conjugated carbon based materials, especially for graphyne systems. Results revealed that some transition metals like Fe and Cr, in doping procedure, show Half-Metallicity but Ni and Mn do not. The energy of gaps and Half-Metallicity are controllable by tuning the valence electron numbers [185]. Moreover, functionalization of graphyne is a way to modify its structural and electronic properties. Fluorination of graphyne is an example of this method in order to make necessary changes in graphyne, in this method, the hybridization state of atoms changes to $sp^3$. As a result this process will open band gap in the band structure [186]. Hydrogen adsorption is another effectual way for functionalization graphyne which can alter the electronic properties of carbon nanostructures. In this regard, Jie Tan et al. using fist-principle calculations studied hydrogenated graphyne and proved that with hydrogen coverage the band gap of 2D hydrocarbon materials will be tunable, as in this case the band gap of hydrocarbon material when all the carbon atoms has been hydrogenated, was increased from 1.01 eV to 4.43 eV [187].

One of the roads still is not known completely in the material science of carbon compounds and graphyne is recognizing their electronic properties modification when they interact with transition metal (TM) atoms [188]. The interaction of these

compounds with transition metals is important because TM atoms are generally used as catalyst in their preparation. Besides, these atoms can be used to tune the bandgap of carbon nanotubes (CNTs) [189,190] which may open novel routs for designing new nanodevices or spintronic devices [191,192]. Some DFT calculations illustrated that transition metals alter the electronic properties of graphdiyne and graphyne sheets and generate various magnetic states such as spin-select half-semiconductors or half-metals. This variation arises from the charge transfer between the transition metal atoms and carbon atoms of the sheet [184].

In this thesis, we are interested in the γ- graphyne (simply called 'graphyne' hereafter) since it is the lowest energy member of the graphyne family and it has the biggest potential to be synthesized in the future. We perform calculations based on density functional theory (DFT) to study the nature of sp and $sp^2$ bonding and the band structure of graphyne. Particularly we are interested in how the metal atoms (Fe, Co, Ni), named also as transition metal (TM) atoms, interact with the graphyne nanotubes and modify their energy band structure [193]. This causes altering of their electronic properties. The interaction of metal atoms with the graphyne carbon atoms is also important because TM atoms are usually used as catalyst in their preparation. Comparison of the results to that obtained for TM interaction with graphyne sheets [26] helps us to understand the effect of curvature (or σ-π hybridization) on the electronic and magnetic properties of graphyne compounds.

### 3.4.2. Method of Calculation

A sheet of graphyne can be rolled to form graphyne based nanotubes (GNT). Depending upon the axis of rolling, the nanotubes can be arm-chair, zig-zag or chiral. The structure of a nanotube can be specified by a vector, (n,m), which defines how the graphyne sheet is rolled up. The vector is defined as $C_h = na_1 - ma_2$ .For example, the vector for zigzag nanotubes is represented by (n,n) and the chiral ones by (n,0), see Fig. 3.29. When the orbitals overlap along an axis between the atoms (internuclear

axis), they form a σ-bond. In this type of bonding the electron density is highest in the space between the atoms. For p orbitals, sideways overlapping is also possible. This results in the formation of π-bonds [194]. Atomic orbitals combine and form extended band structures. The energy gap between the highest occupied and the lowest unoccupied atomic state is called a band gap. As a result of electron excitation, the bands can broaden and start overlapping each other. This is the reason for example how insulator can become semiconductor.

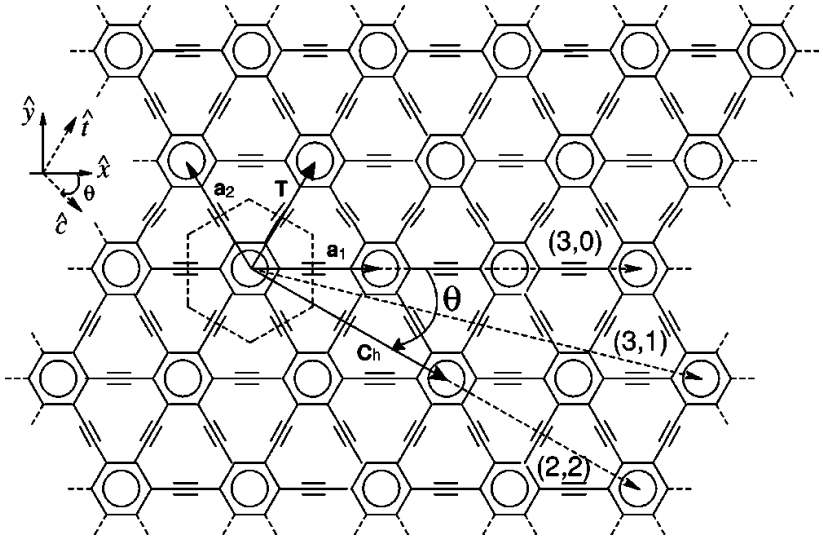


Figure 3. 29 The γ-graphyne sheet unit cell (dashed hexagon) and some chiral vectors. Adapted from Refs. [17] and [36].

The unit cell of the graphyne sheet which is found in our work is displayed in Fig. 3.30 along with its base vectors.

These vectors are defined as $a_1 = ax$ and $a_2 = a\ \ 2\,(-x + 3^{1\ \ 2}y)$, with $a$ = 6.86 Å [195]. A unit cell of this nanotube has 48 carbon atoms and its radius and height are 7.6 and 6.86 Å, respectively.

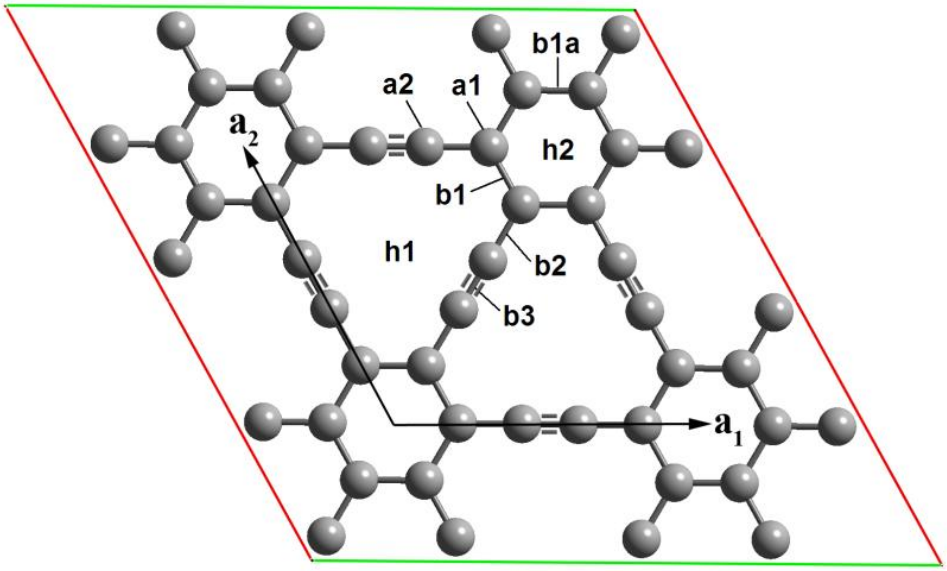


Figure 3. 30 A $\mathbf{2} \times \mathbf{2}$ supercell of graphyne sheet (adsorption sites which are shown in this figure will be explained in the text).

The lengths of different carbon-carbon bonds have been taken from the work of Narita, et al. [51].

In this study, we have used four GNTs to study the effects of diameter and chirality on the interaction with TM atoms. These are (2,2), (3,0), (3,3), and (5,0) tubes. Table 3.9 compares some properties of these four nanotubes. The nanotubes were placed in a tetragonal supercell of $a_{sc}\text{Å} \times a_{sc}\text{Å} \times c_{sc}\text{Å}$, with parameters given in Table 3.9, to simulate an infinitely long 1D periodic system. For example, the (2, 2) graphyne nanotube, shown in Figure 3.31, was placed in a tetragonal supercell of $20\text{Å} \times 20\text{Å} \times 6.86\text{Å}$. The empty spaces along the *x* and *y* directions were included to avoid interactions in the *xy* plane.

Calculations have been done applying spin-polarized DFT method and using plane-waves [153] which implemented in Quantum Espresso package [152]. The interaction between the ionic cores and valance electrons are explained with ultra-soft

pseudopotentials. The generalized gradient approximation (GGA) with Perdew-Burke-Ernzerhof (PBE) functional [196] was employed using a plane-wave cutoff of 300 eV.

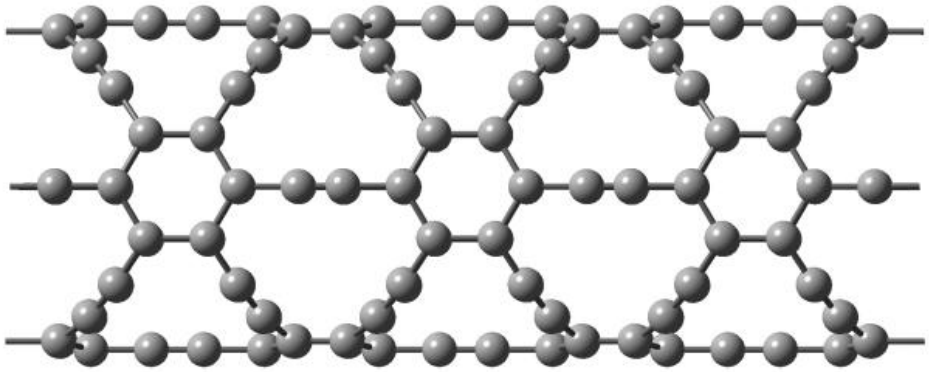

Figure 3. 31 Schematic presentations of (2, 2) graphyne nanotube.

The structure of each of the nanotubes was first optimized and then, one TM atom (Fe, Co, Ni) was placed on the external surface of the nanotube. As it is shown in Figure 3.30, eight different adsorption sites were used for each TM atom. These are atop (a1, a2), bridge (b1, b1a, b2, b3), and hollow (h1, h2) sites. In atop positions, each of TM atoms is located over one of the atoms of nanotube. For the case a1, the TM atom is placed over the carbon atom with $sp^2$ hybridization and for a2, it is over the carbon with sp hybridization. As it is clear in Fig. 3.30, b1, b2 and b3 are bridge positions i.e. each of TM atoms is situated over one of the bonds of nanotube. This bridge bonding for b1 is a kind of $C(sp^2)$-$C(sp^2)$, for b2 and b3 are $C(sp^2)$-C(sp) and C(sp)-C(sp) bonds, respectively. The position b1a is a $C(sp^2)$-$C(sp^2)$ bonding which is parallel to the nanotube axis ( 'a' is the axial indicator). The h1 and h2 are hollow positions. In these cases the TM atom is located over one of the rings of nanotube. For h1, this ring is composed of C-C≡C-C bonds and for h2 is a six-member benzene ring.

As can be seen, all nonequivalent positions have been considered to insert TM atoms. In each of these eight cases, the metal atom in the primitive structure (before relaxation) is placed at a distance of approximately 1.8 Å from adjacent carbon atoms. The metal-adsorbed nanotubes were fully relaxed using the convergence threshold of 0.01 meV in energy and 0.012 eV/Å in force. The Brillouin zone was sampled using a $1 \times 1 \times 11$ Monkhorst-Pack [155] grid of k-points for the calculation of energy and other properties.

Table 3. 9 Properties of four studied graphyne nanotubes (GNTs)

| GNT | no. of atoms | $a_{cs}$ (Å) | $c_{sc}$ (Å) | diameter (Å) |
|---|---|---|---|---|
| (2,2) | 48 | 20 | 6.86 | 7.6 |
| (3,0) | 72 | 20 | 11.88 | 6.6 |
| (3,3) | 72 | 25 | 6.86 | 11.4 |
| (5,0) | 120 | 25 | 11.88 | 10.9 |

To evaluate one of the favorable quantities of adsorption configuration, the binding energy is defined as

$$E_b = E_{(GNT-TM)} - E_{(GNT)} - E_{(TM)} \tag{3.9}$$

where $E_{(GNT-TM)}$ denotes the spin-polarized total energy of fully optimized TM-adsorbed nanotube, $E_{(\mathrm{GNT})}$ is energy of pure nanotube, and $E_{(\mathrm{TM})}$ is spin-polarized total

energy of an isolated TM atom. All three terms were evaluated using a same supercell. A negative value for $E_b$ shows an exothermic adsorption.

### 3.4.3. Results and Discussion

#### 3.4.3.1. (2,2) GNT

Several researches have been done and reported about the structure and properties of pure graphyne which are of the important references for our calculations [50,171,173]. As mentioned before, in present work, three TMs (Co, Fe and Ni) are selected to adsorb on GNTs. All parameters have been fixed and during the self-consistency process, the system was let to be relaxed. It should be pointed out that optimization results of GNTs with metal atoms adsorbed on different sites showed that some of these sites are not stable. In Table 3.12 the structures obtained for three TM and eight adsorption sites on the surface of a (2,2) GNT, binding energies, total magnetic moments and bond lengths are displayed. As seen in this table, metal atoms on atop sites (a1, a2) are not stable and a metal atom initially on a1 or a2 sites moves to b2 or b3 sites, respectively, i.e. the atop configuration prefer bridge positions. For Fe metals, the b1 site is not stable and shifts to h2, while for Ni, b3 complex changes to h1.

Furthermore, all binding energies are negative, which indicate that the interaction between transition metal atoms with graphyne nanotube is favorable. The binding energy of Ni@ (2,2) and Co@ (2,2) are 4.93 eV and 4.83 eV, respectively, which is related to strong interaction between the Ni and Co with C atoms in nanotube, i.e. Ni and Co bind to GNT with more negative binding energies than Fe. As it is seen in this table, the most binding energies belong to the h1 adsorption sites (Figure 3.32), which

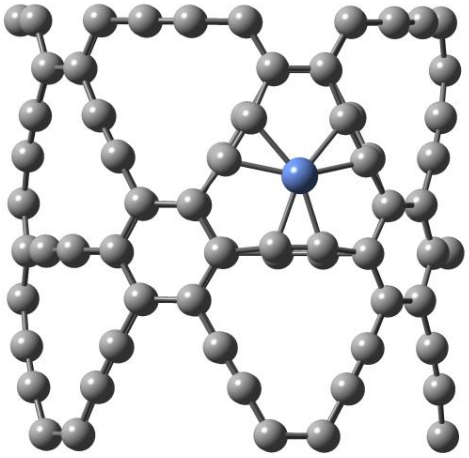

**(a)**

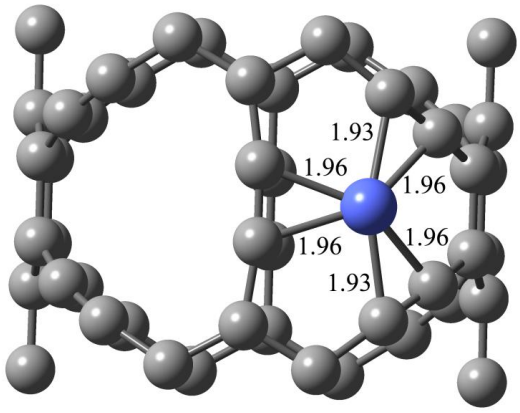


**(b)**

Figure 3. 32 a) optimized transition metal-nanotube complex with the metal adsorbed on h1 site b) Co atom adsorbed on nanotube which has moved to h1 site from its original (values are Co-C bond lengths in Angstrom). Blue and gray balls represent the TM and carbon atoms, respectively [192].

Table 3. 10 Summary of results for transition metal adsorption on a (2, 2) GNTs [193].

| TM | initial site | final site | $E_b$ (eV) | $\mu$ ($\mu_B$) | TM–C distance (Å)[a] |
|---|---|---|---|---|---|
| Fe | | | | | |
| | a1 | b2 | –0.95 | 4.00 | 2.1 (2) |
| | a2 | b3 | –1.32 | 4.00 | 2.0 (2) |
| | b1 | h2 | –1.56 | 2.00 | 2.1 (2), 2.2 (4) |
| | b1a | b1a | –1.06 | 3.81 | 2.1 (2) |
| | b2 | b2 | –1.10 | 4.05 | 2.1 (2) |
| | b3 | b3 | –1.32 | 3.98 | 2.0 (2) |
| | h1 | h1 | –4.58 | 2.06 | 2.0 (6) |
| | h2 | h2 | –1.56 | 2.00 | 2.1 (2), 2.2 (4) |
| Co | | | | | |
| | a1 | b2 | –1.54 | 1.37 | 1.9 (2) |
| | a2 | b3 | –1.71 | 1.16 | 1.9 (2) |
| | b1 | b1 | –1.93 | 1.00 | 1.9, 2.1 |
| | b1a | b1a | –1.93 | 1.00 | 1.9 (2) |
| | b2 | b2 | –1.54 | 1.37 | 1.9 (2) |
| | b3 | b3 | –1.71 | 1.14 | 1.9 (2) |
| | h1 | h1 | –4.83 | 1.00 | 1.9 (2), 2.0 (4) |
| | h2 | h2 | –1.75 | 1.20 | 2.0 (2), 2.2 (4) |
| Ni | | | | | |
| | a1 | b2 | –1.74 | 0.00 | 1.9 (2) |
| | a2 | b3 | –1.87 | 0.04 | 1.9 (2) |
| | b1 | b1 | –1.88 | 0.03 | 1.9, 2.2 |
| | b1a | b1a | –1.87 | 0.03 | 1.9 (2) |
| | b2 | b2 | –1.74 | 0.07 | 1.9 (2) |
| | b3 | h1 | –4.93 | 0.00 | 1.9 (2), 2.0 (4) |
| | h1 | h1 | –4.93 | 0.01 | 1.9 (2), 2.0 (4) |
| | h2 | h2 | –1.75 | 0.03 | 2.0 (2), 2.2 (4) |

[a] number of bonds of each length are given in parentheses.

is in agreement with calculations for Ca adsorption on a (4,2) GNT [187] and graphyne sheets [197]. The TM-C bond lengths for all cases are approximately similar.

In addition to the mentioned quantities, in the Table 3.10, the total magnetic moments of all complexes have been also compared. According to these results, the average magnetic moments of Ni complexes are zero, so these metals are non-magnetic. The other remarkable matter is that the Fe and Co metals possess non-zero magnetic moments and display magnetic complexes, the magnetic moments of Fe complexes are almost twice more than the Co ones.

### 3.4.3.2. (3,0) GNT

As part of our ongoing study of the effect of transition metals adsorption on graphyne nanotubes, we have applied three metals (Fe, Co and Ni) on (3,0) GNT. The corresponding optimized binding energies, stable sites and magnetic moments of these configurations are listed in Table 3.11. For iron atoms, our calculations display that the most favorable adsorption site is hollow site, h1. The three atoms on atop site a1 and bridge site b1 and b2 are not stable and move to the h1 site, while the atom on a2 site changes to b3 site. For all cases, it seems that most of the atoms on atop and bridge positions are not stable and change their position to hollow site, which yields the most binding energy. This route is repeated similarly for Co and Ni atoms adsorptions on (3,0) GNT either, i.e. in this case, also, the a1 and a2 sites change their positions to h1 and b3 sites, which lie in higher energies than the others. Generally in a (3,0) nanotube four stable sites are h1,b3, h2 and b1a. The strongest binding occur when TM atoms are located at the hollow and bridges sites. The system has magnetic moments of 2 $\mu_B$ and 4 $\mu_B$ for Fe complexes and 1 $\mu_B$ for Co complexes, but still Ni complexes are non-magnetic [193].

### 3.4.3.3. (3,3) and (5,0) GNTs

As mentioned above, the Fe, Co and Ni atoms are initially placed on eight different sites of the relaxed graphyne nanotubes. The adsorbed structures are optimized and the corresponding results are presented in Table 3.12 and Table 3.13. Our calculations show that for (3,3) and (5,0) GNTs, like to two aforesaid nanotubes, the most interesting site is h1with average binding energy of almost 5.00 eV. For example in the case of a (5,0) tube, virtually all structures relax to a h1. One subtle point which is considerable is that the binding energies for Ni complexes are very different for all sites from the similar ones in (2,2) and (3,0) nanotubes. In these two nanotubes, (3,3) and (5,0) cases, the Ni atoms bind strongly to GNTs in comparison with other nanotubes. About the magnetic moments, the same behavior has been followed; Fe complexes own the most magnetic moments. In the second tier, Co complexes exist and finally Ni complexes which are non-magnetic. The net magnetic moment for Fe@(3,3) nanotube at b3 site is 4 $\mu_B$ which is large, thus this Fe-doped nanotube can be proposed as nanomagnet. Our calculations are in good agreement with other studies for carbon nanotubes [193, 197,199].

### 3.4.3.4. Magnetic and Electronic Properties

To shed more light on structure and magnetic properties of these TM-doped GNTs, we have studied the adsorption of a metal atom on h1 site with more details. The outcomes are presented in Table 3.14. In accord with previous results [32,34], the absolute value of the binding energy obtained from spin-polarized calculations ($E_b^p$) is smaller than the value corresponding to spin-unpolarized calculations ($E_b^u$). As cited before, in all cases, the TM atom remains in the plane of the acetylenic ring and makes bonds with six nearest neighbor carbon atoms (Figure 3.32a), with bond lengths less than 2 Å.

Table 3. 11 Summary of results for transition metal adsorption on (3,0) graphyne nanotube.

| TM | initial site | final site | $E_b$ (eV) | $\mu$ ($\mu_B$) | TM–C distance (Å) |
|---|---|---|---|---|---|
| Fe | | | | | |
| | a1 | h1 | –4.60 | 2.00 | 2.0 (6) |
| | a2 | b3 | –1.86 | 2.00 | 1.9 (2) |
| | b1 | h1 | –4.60 | 2.00 | 2.0 (6) |
| | b1a | b1a | –1.24 | 4.00 | 2.0 (2) |
| | b2 | h1 | –4.60 | 2.00 | 2.0 (6) |
| | b3 | b3 | –1.86 | 2.00 | 1.9 (2) |
| | h1 | h1 | –4.60 | 2.00 | 2.0 (6) |
| | h2 | h2 | –1.76 | 2.00 | 2.1 (4), 2.3 (2) |
| Co | | | | | |
| | a1 | h1 | –4.83 | 1.00 | 1.9 (2), 2.0(4) |
| | a2 | b3 | –2.12 | 1.00 | 1.9 (2) |
| | b1 | a1 | –1.90 | 1.00 | 1.9, 2.0(2) |
| | b1a | b1a | –1.53 | 1.00 | 1.9 (2) |
| | b2 | - | - | - | - |
| | b3 | b3 | –2.05 | 1.00 | 1.8 (2) |
| | h1 | h1 | –4.83 | 1.00 | 1.9 (2), 2.0 (4) |
| | h2 | h2 | –1.90 | 1.00 | 2.0 (4), 2.1 (2) |
| Ni | | | | | |
| | a1 | h1 | –4.78 | 0.46 | 2.0 (6) |
| | a2 | b3 | –2.49 | 0.03 | 1.8 (2) |
| | b1 | h2d | –2.13 | 0.56 | 1.9, 2.0(2) |
| | b1a | b1a | –1.99 | 0.02 | 1.9 (2) |
| | b2 | h1 | –4.78 | 0.46 | 2.0(6) |
| | b3 | b3 | –2.49 | 0.03 | 1.8 (2) |
| | h1 | h1 | –5.05 | 0.00 | 2.0 (6) |
| | h2 | h2 | –2.08 | 0.04 | 2.1 (4), 2.3 (2) |

Table 3. 12 Results for transition metal adsorption on (3,3) graphyne nanotube.

| TM | initial site | final site | $E_b$ (eV) | $\mu$ ($\mu_B$) | TM–C distance (Å)[a] |
|---|---|---|---|---|---|
| Fe | | | | | |
| | a1 | - | - | - | - |
| | a2 | b3 | –1.57 | 4.00 | 2.0 (2) |
| | b1 | h1 | –4.54 | 2.00 | 2.0 (6) |
| | b1a | - | - | - | - |
| | b2 | b3 | –1.57 | 4.00 | 2.0 (2) |
| | b3 | b3 | - | - | - |
| | h1 | h1 | –4.54 | 2.00 | 2.0 (6) |
| | h2 | h2 | –1.85 | 2.00 | 2.1 (6) |
| Co | | | | | |
| | a1 | b2 | –1.37 | 1.37 | 1.9 (2) |
| | a2 | b3 | –1.55 | 1.00 | 1.8 , 2.0 |
| | b1 | h1 | –4.71 | 1.00 | 1.9(4), 2.0(2) |
| | b1a | b1a | –1.69 | 1.00 | 1.9 (2) |
| | b2 | h1 | –4.71 | 1.00 | 1.9 (4), 2.0(2) |
| | b3 | - | - | - | - |
| | h1 | h1 | –4.72 | 1.00 | 1.9 (4), 2.0 (2) |
| | h2 | h2 | –1.69 | 1.05 | 2.0 (2), 2.1 (4) |
| Ni | | | | | |
| | a1 | h1 | –5.15 | 0.00 | 1.9 (2), 2.0(4) |
| | a2 | b3 | –1.99 | 0.52 | 1.9 (2) |
| | b1 | h1 | –5.15 | 0.00 | 1.9 (2), 2.0(4) |
| | b1a | h1 | –5.14 | 0.00 | 1.9 (2), 2.0(4) |
| | b2 | h1 | –5.15 | 0.00 | 1.9 (2), 2.0(4) |
| | b3 | b3 | –2.13 | -0.06 | 1.9 (2) |
| | h1 | h1 | –5.15 | 0.00 | 1.9 (2), 2.0 (4) |
| | h2 | h2 | –2.05 | 0.00 | 2.0 (2), 2.1 (4) |

Table 3. 13 Results for transition metal adsorption on (5,0) graphyne nanotube.

| TM | initial site | final site | $E_b$ (eV) | $\mu$ ($\mu_B$) | TM–C distance (Å)[a] |
|---|---|---|---|---|---|
| Fe | | | | | |
| | a1 | - | - | - | - |
| | a2 | - | - | - | - |
| | b1 | - | - | - | - |
| | b1a | - | - | - | - |
| | b2 | - | - | - | - |
| | b3 | b3 | –2.04 | 2.02 | 1.9 (2) |
| | h1 | h1 | –4.88 | 2.00 | 2.0 (6) |
| | h2 | h2 | –2.16 | 2.00 | 2.1 (4), 2.2 (2) |
| Co | | | | | |
| | a1 | h2 | –1.98 | 1.00 | 2.1 (4), 2.2(2) |
| | a2 | b3 | –2.07 | 1.50 | 1.9 (2) |
| | b1 | h2 | –1.98 | 1.00 | 2.1(4), 2.2 (2) |
| | b1a | - | - | - | - |
| | b2 | h1 | –4.99 | 1.00 | 1.9 (2), 2.0(4) |
| | b3 | b3 | –2.02 | 1.32 | 1.8 (2) |
| | h1 | h1 | –4.99 | 1.00 | 1.9 (2), 2.0 (4) |
| | h2 | h2 | –1.98 | 1.00 | 2.1 (4), 2.2 (2) |
| Ni | | | | | |
| | a1 | h1 | –5.34 | 0.00 | 1.9 (4), 2.0(2) |
| | a2 | - | - | 0.00 | - |
| | b1 | h1 | –5.33 | 0.00 | 1.9( 4), 2.0(2) |
| | b1a | h1 | –5.34 | 0.00 | 1.9 (3), 2.0(3) |
| | b2 | h1 | –5.34 | 0.00 | 1.9 (3), 2.0(3) |
| | b3 | b3 | –2.48 | -0.02 | 1.8 (2) |
| | h1 | h1 | –5.34 | 0.00 | 1.9 (4), 2.0 (2) |
| | h2 | h2 | –2.23 | 0.00 | 2.1 (4), 2.2 (2) |

Table 3. 14 Properties of graphyne nanotubes with a transition metal (TM) atom adsorbed on the h1 site. $E_b^p$ and $E_b^u$ are binding energies obtained from spin-polarized and spin-unpolarized calculations, respectively. $d_{TM\text{-}GNT}$ is the average distance of the transition metal from six neighboring carbon atoms, $\mu_B$ is the net magnetic moment of the system and $C$ is the charge transferred from the metal to nanotubes.

| system (TM@GNT) | $E_b^p$ (eV) | $E_b^u$ (eV) | $d_{TM\text{-}GNT}$ (Å) | $\mu_B$ | $C$ (e) |
|---|---|---|---|---|---|
| Fe@(2,2) | –4.58 | –6.30 | 1.99 | 2.06 | 0.80 |
| Co@(2,2) | –4.83 | –5.82 | 1.95 | 1.00 | 0.77 |
| Ni@(2,2) | –4.93 | –5.22 | 1.96 | 0.01 | 0.95 |
| Fe@(3,0) | –4.60 | –6.50 | 1.98 | 2.00 | 0.81 |
| Co@(3,0) | –4.83 | –5.91 | 1.95 | 1.00 | 0.80 |
| Ni@(3,0) | –5.05 | –5.26 | 1.96 | 0.00 | 0.96 |
| Fe@(3,3) | –4.54 | –6.33 | 1.98 | 2.00 | 0.88 |
| Co@(3,3) | –4.72 | –5.89 | 1.95 | 1.00 | 0.80 |
| Ni@(3,3) | –5.15 | –5.34 | 1.96 | 0.00 | 0.95 |
| Fe@(5,0) | –4.88 | –6.43 | 1.97 | 2.00 | 0.82 |
| Co@(5,0) | –4.99 | –5.96 | 1.95 | 1.00 | 0.82 |
| Ni@(5,0) | –5.34 | –5.39 | 1.96 | 0.00 | 0.98 |

In comparison with carbon nanotubes [33], the larger binding energies and shorter bond lengths shows that binding in TM-GNT complexes is stronger than TM-CNTs.

As stated above, for Co and Fe metals, the TM-GNT systems are magnetic, while Ni complexes are non-magnetic though. These values agree well with the observations for graphene sheets [182] and carbon nanotubes [189]. The total magnetic moment over the metal atomic basins is close to the value of the net magnetic moment of the system, because the major contribution in spin-polarization is related to the transition metal, as it is shown in spin-density isosurfaces in Fig. 3.33. These graphs which are for Fe and Co on a (2,2) GNT demonstrate that the positive polarization is contributed significantly from the TM atom and the neighboring carbon atoms show smaller, negative spin-polarization.

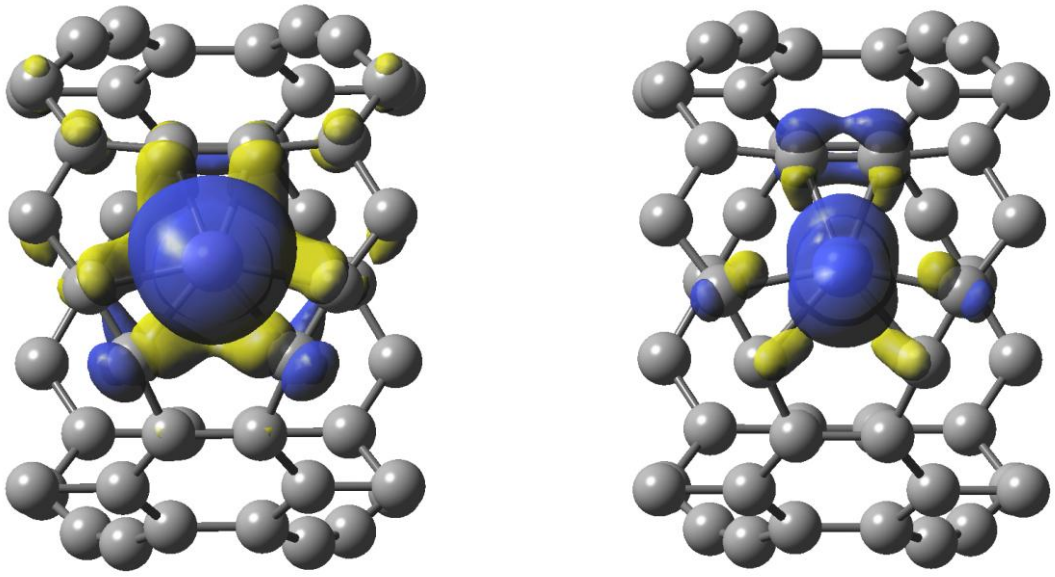

(a) (b)

Figure 3. 33 Spin-density isosurfaces for Fe (a) and Co (b) adsorbed (2,2) GNTs. Blue (dark) and yellow (light) regions correspond to positive and negative polarization, respectively. The isodensity value is 0.002 $\mu_B$/Bohr$^3$.

Pristine graphyne nanotubes are non-magnetic, this changes in the magnetic moment of the systems is related to TM atoms and comes from these atoms. Compared to the values of 4 (3) for an isolated Fe (Co) atom, the magnetic moment of the systems is reduced due to the formation of TM-C bonds. This reduction is derived from charge transfer from metal to nanotube. Table 3. 14 shows that Ni complexes have the most negative binding energies and largest values of the transferred charge. In order to precise electronic properties, electronic band structures for bare and TM-adsorbed GNTs are shown in Figures 3.34 –3.37. For bare nanotubes, the calculations show that all of them are direct band-gap semiconductors. The (2,2) GNT (Figure 3.34a) has a band gap of 0.6 eV at the Z point. The band gap at the Γ point is larger (~1.0 eV).

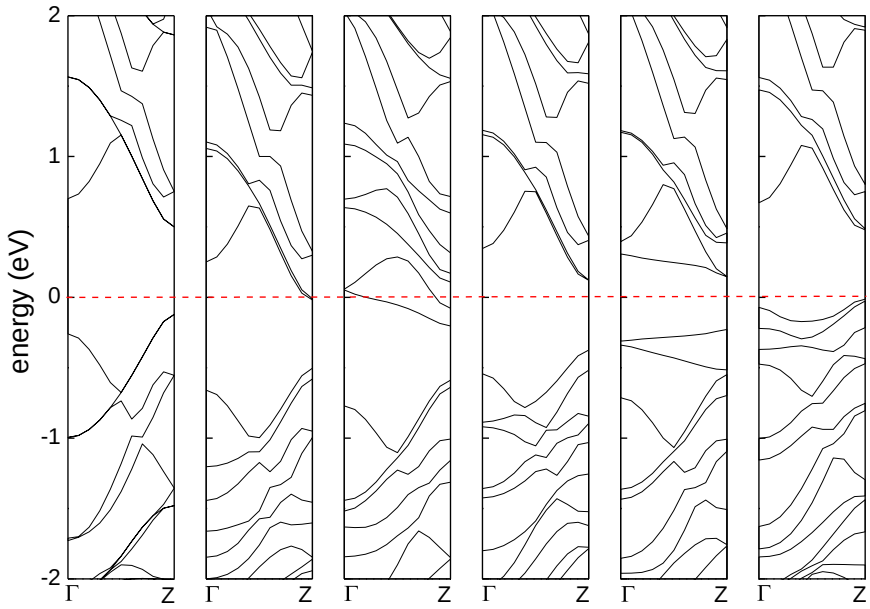


Figure 3. 34 Electronic band structures for a bare (2,2) graphyne nanotube (a) and TM-adsorbed (2,2) nanotubes (b-f). Parts (b) to (f) are for TM = Fe (spin-up), Fe (spin-down), Co(spin-up), Co(spin-down), and Ni, respectively. The dashed line at zero energy indicates the position of the highest occupied level.

For the pristine (3,0) nanotube (Figure 3.35a), the gap increases to 1.2 eV at the Γ point. Both (3,3) and (5,0) GNTs have a band gap value of 0.7 eV at the Γ point. The shape of the bands in the bottom of the conduction band for the bare (5,0) GNT is in agreement with previous calculations [36]. There is no DFT data about the electronic band structure of GNTs, but tight binding calculations show that the band gap of GNTs is independent of their diameter and chirality [36]. Our results show that for (3,3) and (5,0) nanotubes which have similar diameters (Table 3.11), the band gaps are equal, i.e., for a fixed diameter, the band gap is independent of chirality. However, we cannot completely justify the independence of band gap from the tube's diameter, since the (3,0) tube violates this rule. If we consider the band gap at the Γ point, we can say that with increasing diameter, the band gap decreases.

Upon TM adsorption, the highest occupied level shifts up to the conduction band and new states are formed in the band gap, which originate from the adsorbed metal atom. For Fe and Co, the band structures are spin-polarized, but the Ni-GNT complexes are nonmagnetic, with no spin-splitting in bands. For the Fe-(2,2) GNT complex, two new states are appeared in the minority spin channel, above and below the highest occupied level, which have a small overlap (Figure 3.34c). Therefore, the spin-down channel is a semimetal. The bottom of the conduction band in the majority spin-channel, which is derived from the conduction band of the bare tube, crosses the highest occupied level and also overlaps with higher bands (Figure 3.34b), which characterizes a metal. So this system is a metal in spin-up and a semi-metal in spin-down channel. With an adsorbed Co atom, the (2,2) nanotubes becomes a half-semiconductor, with a gap of 0.5 eV in the majority and 0.4 eV in the minority spin channel (Figures 3.34 d,e). Both of them have direct band gaps at the Z point. An empty and two filled bands are formed in spin-down channel. The Ni adatom narrows the band gap of the bare tube and the corresponding complex is a semiconductor with a direct band gap of 0.5 eV at the Z point. The observations here are in general agreement with the results for a graphyne sheet [183].

For the (3,0) GNT, Both Fe-GNT and Co-GNT systems are half-semiconductors, with band gaps larger than those for a (2,2) GNT. The newly-formed filled state in the

minority spin channel of Fe (Figure 3.35c) is close to the highest occupied level, but does not cross it, so, in contrast to the (2,2) tube, the system is not metallic. The band gap is 1.1 eV in spin-up and 0.75 eV in spin-down states, both at the Γ point. In the case of Co, new bands are formed both in majority and minority spin channels (Figures 3.35 d,e). The spin-up channel has an indirect band gap of 1.0 eV, while the spin-down bands show a direct band gap of 0.45 eV at the M point. Similar to the (2,2) tube with a Ni atom, the band gap of a (3,3) nanotube reduces to ~0.85 eV when a Ni atom adsorbs. The Ni-(3,0) GNT system has a direct band gap of ~0.85 eV at the Γ point.

The results for (3,3) and (5,0) nanotubes (Figures 3.36 and 3.37) are similar to the (2,2) and (3,0) tubes, respectively, but the band gaps are generally smaller in these larger-diameter tubes. An exception is for the Fe adsorption on a (3,3) GNT, in which the system is still a semimetal in the minority spin channel, but it is a semiconductor in the majority spin direction. Therefore, Fe-(3,3) GNT system can be viewed as a half-semimetallic system.

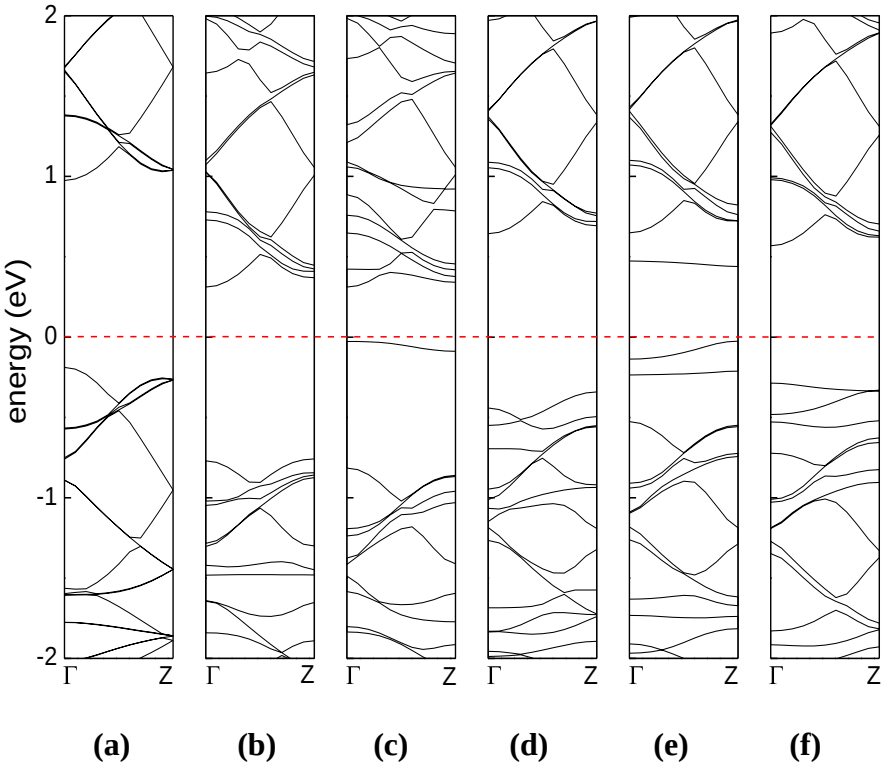


Figure 3. 35 Electronic band structures for a bare (3,0) graphyne nanotube (a) and TM-adsorbed (3,0) nanotubes (b-f). Parts (b) to (f) are for TM = Fe (spin-up), Fe(spin-down), Co(spin-up), Co(spin-down), and Ni, respectively. The dashed line at zero energy indicates the position of the highest occupied level.

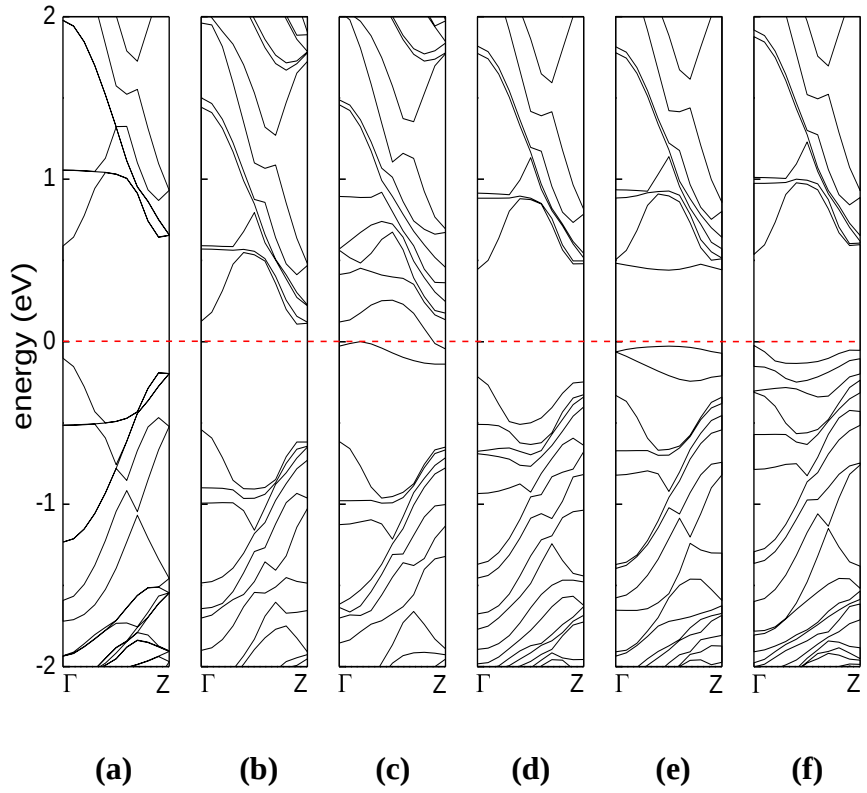


Figure 3. 36 Electronic band structures for a bare (3,3) graphyne nanotube (a) and TM-adsorbed (3,3) nanotubes (b-f). Parts (b) to (f) are for TM = Fe (spin-up), Fe (spin-down), Co(spin-up), Co(spin-down), and Ni, respectively. The dashed line at zero energy indicates the position of the highest occupied level.

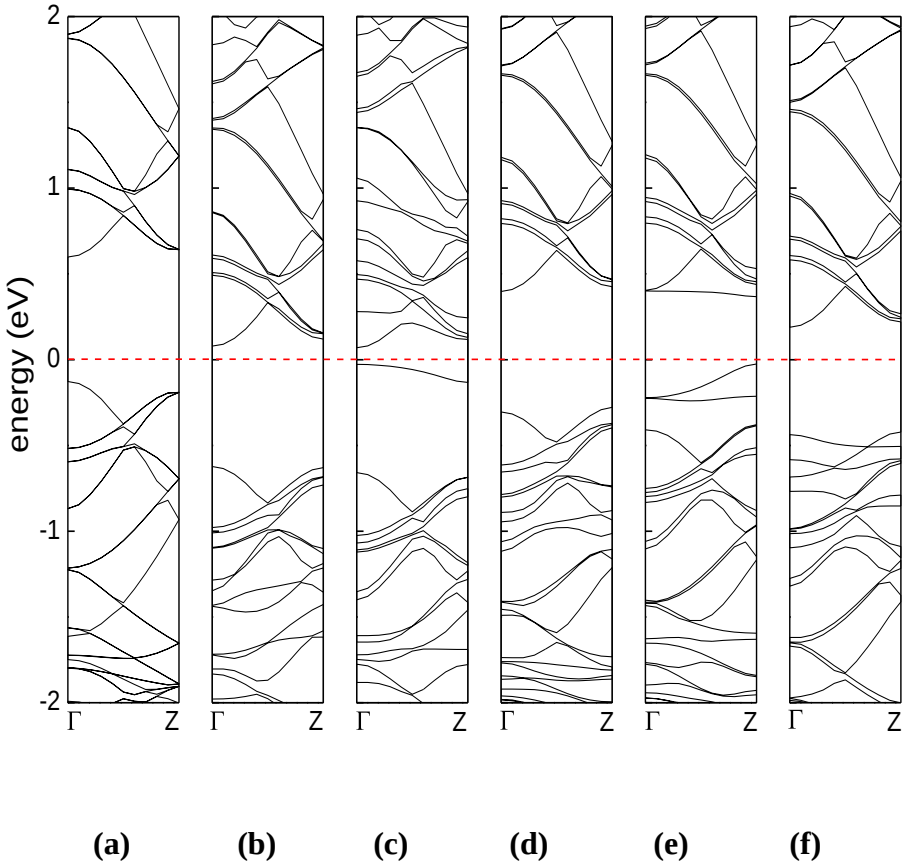


Figure 3. 37 Electronic band structures for a bare (5,0) graphyne nanotube (a) and TM-adsorbed (5,0) nanotubes (b-f). Parts (b) to (f) are for TM = Fe (spin-up), Fe (spin-down), Co(spin-up), Co(spin-down), and Ni, respectively. The dashed line at zero energy indicates the position of the highest occupied level.

# CHAPTER 4

# CONCLUSIONS

During this study, several achievements were made. Generally, we have concentrated mainly on the calculation of structural, electronic and magnetic properties of various nanostructures. We focused on iron oxide nanostructures and also Graphyne nanotubes.

In the chapter 1 we have introduced the physics of 0D and 1D nanostructures and characteristic of iron oxides, $Fe_2O_3$ and its various polymorphs and their magnetic properties and also Graphyne. We have discussed their importance from both the scientific and technological point of view.

In the chapter 2 we have discussed our molecular dynamics method, what we have implemented later for iron oxide nanorods and spherical nanoparticles. We have also discussed the basic ideas of density functional theory, which is the method to study iron oxide clusters and graphyne nanotubes.

In the first part of chapter 3 we have implemented the molecular dynamics on the iron oxide nanorods and spherical nanoparticles. In particular, the structure and stability of beta-iron oxide nanorods at temperatures 1K and 300K have been studied by using molecular dynamic technique. The structural properties and radial distribution functions of spherical nanoparticles studied at temperature range from 1K to 900K by 100K intervals using the same method.

Furthermore, we performed our other calculations using the DFT method. We figured out that DFT is successful to investigate such systems, as clusters (iron oxide clusters) and graphyne nanotubes.

Within this method, in the third part of chapter 3 we systematically investigated the structural, electronic and magnetic properties of $(Fe_2O_3)_n$ clusters (n = 1-5). The

results for small clusters showed good agreement with other calculations. We observed an interesting result for the $Fe_4O_{12}$ cluster of iron oxide, in the first spin configuration state. It was that these states for $n$ = 4 (n4-1) was a half-metallic antiferromagnet, which is important in spintronics applications. The most of the considered clusters were semi-metal or half-metal due to presence of Fe atoms.

In the last part of chapter 3 we have also discussed the effect of transition metal adsorption on electronic and magnetic properties in graphyne nanotubes. We tried four different sizes of graphyne nanotubes and various possible adsorption configurations and their effect on the electronic band structure of graphyne nanotubes. The results showed that adsorption sites and nanotube sizes are key factors and playing important roles on electronic and magnetic properties of graphyne nanotubes.

The continuing development of material science and nanostructure technologies make evident the need for detailed theoretical understanding of these systems. Several theoretical approximations have been developed to study their basic properties. In this regard, trends in structure, electronic and magnetic properties, investigated in this thesis, and also for optical properties may be studied as change of number of atoms in the clusters, nanotubes and nanoparticles at different temperatures or using various cases of adsorption and doping metals

The iron oxide nanotubes could be one of the interesting projects because of their high ratio of surface area to volume. Various reactions or defects can be applied on these nanotubes in order to control their stability or properties for industrial application. On the other hand, magnetic nanotubes might be an amazing subject to study.

Properties of iron oxide clusters with many atoms for instance more than a hundred atoms, which are less studied compared to the small clusters may be investigated since that can be more easily found in real life and laboratories. Similar to nanotubes several reactions and defects can be carried out on the iron oxide clusters, especially with larger clusters. The features of magnetic clusters like iron oxide clusters or clusters which include other metals in their structure offer wide range applications in medical and technical areas. These materials are appropriate candidates for the cancer therapy, pharmaceutical industry as transporters for accommodating small molecules in the

body and also are useful in Magnetic Drug Targeting. The wide range of applications and unending possibilities of these materials display the need for a wide range and readily available materials, and prove the importance of finding thermodynamically stable iron oxide clusters with a very high magnetic moment.

Using DFT, it has been shown that transition metals, Fe and Co are good candidates to be adsorbed to increase the magnetization of graphyne nanotube. For future purposes to evaluate the candidacy of non-transition metals or another element/material adsorption or substitution, it would be a good idea to test their effect on electronic and magnetic properties. Certainly, due to importance of carbon-based materials in modern technology, future studies are necessary in understanding and investigating various and key properties of graphyne and graphdiyne derivatives in various dimensions (nanotubes, nanoflakes, nanoribbons, 0D nanocones, 3D nanotube networks, etc.), also detecting and developing novel preparation routes of these materials.

Simulating and applying electronic transport in nanoscale devices is one of the appealing subjects in researches in recent years. Studying the electronic transport in different molecular devices, including atomic wires or organic molecules sandwiched between various metal surfaces is of importance for new technology especially in the limit of miniaturization. The materials and nanotubes that we studied in this thesis, may be used as electrodes or linkers or electron transports in molecular electronic devices using DFT method.

## REFERENCES


[1] C. Rao and A. Cheetham, Science and technology of nanomaterials: current status and future prospects, Journal of Materials Chemistry, 11 (2001) 2887.

[2] I. Safarik and M. Safarikova, Magnetic nanoparticles and biosciences, Monatshefte Fur Chemie, 133 (2002) 737.

[3] R. Kelsall, I. Hamley and M. Geoghegan, Nanoscale Science and Technology, John Wiley & Sons, UK , 2005.

[4] G. Cao, Nanostructures & Nanomaterials, Imperial College Press, London, 2004.

[5] M. F. Ashby, P. J. Ferreira and D. L. Schodek.Nanomaterials, Nanotechnologies and Design: An Introduction for Engineers and Architects, Elsevier Electronic Books, 2009.

[6] I. Hrivnak (Editor), Nanocrystalline Materials, Cambridge International Science Publishing Cambridge, GBR, 1995.

[7] B. Teo and X. Sun, Silicon-based low-dimensional nanomaterials and nanodevices, Chem. Rev., 107 (2007) 1454.

[8] H. Toffoli, Ş. Erkoç, and D. Toffoli, Modeling of nanostructures. In Handbook of computational chemistry, Springer Science, (2012) 996.

[9] W.A.d. Heer, The physics of simple metal clusters: experimental aspects and simple models, Rev. Mod. Phys, 65 (1993) 611.

[10] M. Brack, The physics of simple metal clusters: self-consistent jellium model and semiclassical approaches, Rev. Mod. Phys., 65 (1993) 677.

[11] C. Henry, Surface studies of supported model catalysts, Surface Science Reports, 31 (1998) 235-325.

[12] A.P. Alivisatos, K.P. Johnsson, X. Peng, T.E. Wilson, C.J. Loweth, M.P. Bruchez Jr. and P.G. Schultz, Organization of 'nanocrystal molecules' using DNA, Nature, 382 (1996) 609.

[13] A. Sundaresan and C. Rao, Implications and consequences of ferromagnetism universally exhibited by inorganic nanoparticles, Solid State Communications, 149 (2009) 1197.

[14] C. Burda, X. Chen, R. Narayanan and M.A. El-Sayed, Chemistry and properties of nanocrystals of different shapes, Chem Rev, 105 (2005) 1025.

[15] Q. Pankhurst, J. Connolly, S. Jones and J. Dobson, Applications of magnetic nanoparticles in biomedicine, J. Phys. D Appl. Phys. , 36 (13) (2003) R167.

[16] S. P. Gubin, Magnetic Nanoparticles, Wiley-VCH Verlag GmbH&Co. KGaA, Weinheim 2009.

[17] R. Zboril, M. Mashlan and D. Petridis, Iron (III) oxides from thermal processes synthesis, structural and magnetic properties, Mossbauer spectroscopy characterization, and applications, Chem. of Mater., 14 (2002) 969.

[18] R. M. Cornel and U. Schwertmann: The Iron Oxides. Structure, properties, reactions and uses, VCH, Weinheim 1996.

[19] T. Muruyama and T. Kanagawa, Electrochromic properties of Iron oxide thin films prepared by chemical vapor deposition, J. Electrochem. Soc., 143 (1996) 1675.

[20] T. Gonzales-Carreno, M.P. Morales and C.J. Serna, Fine β-$Fe_2O_3$ particles with cubic structure obtained by spray pyrolysis, J. Mater. Sci. Lett., 13 (1994) 381.

[21] R. Zboril, M. Mashlan, D. Krausova and P. Pikal: Cubic β-$Fe_2O_3$ as the product of the thermal decomposition of $Fe_2(SO_4)_3$, Hyperfine Interact., 121-122 (1999) 497.

[22] E. Tronc, C. Chan´eac and J. P. Jolivet, Structural and magnetic characterization of $\varepsilon$-$Fe_2O_3$, J. Solid State Chem.,139 (1998) 93.

[23] W. H. Bragg and W. L. Bragg, X-rays and crystal structure, 3rd ed., G. Bell and Sons, London, 1918.

[24] G. Kletetschka, P. J. Wasilewski and P. T. Taylor, Hematite vs. magnetite as the signature for planetary magnetic anomalies?, Phys. Earth Planet. Inter., 119 (2000) 259.

[25] T. P. Raming, A. J. A. Winnubst, C. M. V. Kats and A. P. Philipse, The synthesis and magnetic properties of nanosized hematite (α-$Fe_2O_3$) particles, Journal of Colloid and Interface Science, 249 (2002) 346.

[26] G. Kim, K. H. Han, C. H. Lee and J. Y. Jeong, Crystallographic and magnetic properties of nanostructured Hematite synthesized by the Sol-Gel process, J. Korean Phys. Soc., 38 (2001) 798.

[27] E. L. Williamson, R. Venturini, R. A. Graham and B. Morosin, Morin transition of shock-modified hematite**,** Phys. Rev. B, 34 (1986) 1899.

[28] E. V. San, E. D. Grave and R. E. Vanderberghe, Field-induced spin transitions in hematite powders as observed from Mossbauer spectroscopy, J. Magn. Magn. Mater. 269 (2004) 54.

[29] R.L. Blake, R.E. Hessevick, T. Zoltai and L.W. Finger, Refinement of the hematite structure, Am. Mineral., 51 (1966) 123.

[30] R. M. Cornell and U. Schwertmann, The iron oxides: structure, properties, reactions, occurrences and uses. 2nd ed.: WILEY-VCH GmbH & Co. KGaA, Weinheim, 2003.

[31] J. D. Bernal, Geometry of the structure of monatomic liquids, Nature, 183 (1959) 141.

[32] U. Schwertmann and R. M. Cornell, Iron oxides in the laboratory, VCH VmbH, 1991.

[33] R. Schrader, G. Buttner and Z. Anorg, Powder diffraction file No. 16-653, JCPDS-International Center for Diffraction Data, Swarthmore, PA, 1993.

[34] L. Walter-Levy and E. Quemeneur, Powder diffraction File No. 16-895, JCPDS-International Center for Diffraction Data, Swarthmore, PA, 1993.

[35] I. Dezsi and J. M. D. Coey, Magnetic and thermal properties of $\varepsilon$-$Fe_2O_3$, Phys. Status. Solidi. A ,15 (1973) 681.

[36] F.A. Cotton and G. Wilkinson, Advanced inorganic chemistry, 5nd ed, Wiley, NewYork, 1988.

[37] S. Gubin, Y. A. Koksharov, G. Khomutov and Y. G. Yu, Magnetic nanoparticles: preparation, structure and properties, Russ. Chem. Rev., 74(6) (2005) 489.

[38] Q. Song, Size and shape controlled synthesis and superparamagnetic properties of spinel ferrites nanocrystals, Georgia Institute of Technology, USA, 2005.

[39] S. O. Kasap, Principles of electronic materials and devices, McGraw Hill, New York, 2002.

[40] N.A. Spaldin, Magnetic materials; fundamentals and applications. New York: Cambridge, University Press, 2003.

[41] W. Callister, Materials science and engineering: An Introduction. New York: Jonn Wiley & Sons, 2007.

[42] A. Firouzi, D.J. Schaefer, S.H. Tolbert, G.D. Stucky, and B.F. Chmelka, Magnetic-field-induced orientational ordering of alkaline lyotropic silicate-surfactant liquid crystals, J. Am. Chem. Soc., 119 (1997) 9466.

[43] S. H. Tolbert, A. Firouzi, G.D. Stucky, and B.F. Chmelka, Magnetic field alignment of ordered silicate-surfactant composites and mesoporous silica. Science, 278 (1997) 264.

[44] K. J. Klabunde, Nanoscale Materials in Chemistry, John Wiley&Sons, Inc., Publication, 2001.

[45] J. M .D Coey, Magnetic properties of iron in soil iron oxides and clay materials. In: J, W, Stucki, B, A, Goodman, U. Schwertmann (eds), Iron in soils and clay minerals. D. Reidel Pub. Co., (1988) 397.

[46] R. A. Flinn, P. K. Trojan, Engineering materials and their Applications, $4^{th}$ edition, Copyright by John Wiley & Sons, Inc, 1990.

[47] A. Hirsch, The era of carbon allotropes, Nature Mater., 9 (2010) 868.

[48] J. W. Rohlf, Modern Physics from Aα to Z0, Wiley-VCH, 1994.

[49] R. H. Baughman, H. Eckhardt, and M. Kertesz, Structure-property predictions for new planar forms of carbon: layered phases containing $sp^2$ and sp atoms, J. Chem. Phys. 87 (1987) 6687.

[50] H. Zhang, M. Zhao, H. Bu, X. He, M. Zhang, L. Zhao, Y. Luo, Ultra-high hydrogen storage capacity of Li-decorated graphyne: A first-principles prediction, J. Appl. Phys., 112 (2012) 084305.

[51] N. Narita, S. Nagai, S. Suzuki, and K. Nakao, Optimized geometries and electronic structures of graphyne and its family, Phys. Rev. B, 58 (2) (1998) 11009.

[52] A.L. Ivanovskii, Graphynes and graphdyines, Prog. Solid State Chem.41 (2013) 1.

[53] G. Li, Y. Li, H. Liu, Y. Guo, Y. Li and D. Zhu, Architecture of graphdiyne nanoscale films, Chem. Commun. 46 (2010) 3256 .

[54] V. Bulatov and V. W. Cai, Computer simulations of dislocations, Oxford University Press, 2006.

[55] D. Frenkel and B. Smit, Understanding molecular simulation: from algorithms to applications, Academic press, 2001.

[56] G.D. Billing and K. V. Mikkelsen, Introduction to molecular dynamics and chemical kinetics, New York: J. Wiley & Sons, 1996.

[57] M. Born and K. Huang, Dynamical theory of crystal lattices, 2nd ed., Clarendon Press, Oxford, 1954.

[58] R. Parr and W. Yang, Density functional theory of atoms and molecules, Clarendon Press, Oxford, 1989.

[59] S. D. Ivanov, A.P. Lyubartsev, and A. Laaksonen, Bead-Fourier path integral molecular dynamics, Phys. Rev. E, 67 (2003) 066710.

[60] T. Schlick, Molecular Modeling and Simulation, Springer, Berlin, 2002.

[61] M. P. Allen, D. J. Tildesley, J. R. Banavar, Computer simulation of liquids. Phys. Today, 42 (1989) 71.

[62] M. P. Allen and D. J. Tildesley, Computer simulation of Liquids, Clarendon Press, Oxford, 1987.

[63] L. Verlet. Computer experiments on classical fluids. I. Thermodynamical properties of Lennard-Jones molecules. Phys. Rev., 159 (1967) 98.

[64] L. Verlet. Computer experiments on Classical Fluids. II. Equilibrium correlation functions. Phys. Rev., 165 (1968) 201.

[65] S. Erkoc, Lecture notes on simulations of many-particle systems, METU, 2004.

[66] A. R. Leach. Molecular Modelling: Principles and Applications. Pearson Education Limited, 2001.

[67] M. P. Allen, Introduction to molecular dynamics simulation, Comp. soft matter. From synthetic polymers to proteins, Lecture Notes, Norbert Attig, Kurt Binder,

Helmut Grubmuller, Kurt Kremer (Eds.), John von Neumann Institute for Computing, Julich, NIC Series, 23 (2004) 1.

[68] S, Nose, A molecular dynamics method for simulations in the canonical ensemble. Mol. Phys., 52 (1984) 255; W. G. Hoover, Canonical dynamics: Equilibrium phase-space distributions, Phys. Rev. A, 31 (1985) 1695.

[69] M. Born and R. Oppenheimer, Zur quantentheorıe der molekül (On the quantum theory of molecules), Ann. Phys. 84 (1927) 457.

[70] D. R. Hartree, The wave mechanics of an atom with a non-coulomb central field. Part I. Theory and methods, Proc. Cam. Phil. Soc., 24 (1928) 89.

[71] V. Fock, Näherungsmethode zur Lösung des quantenmechanischen Mehrkörperproblems (First publication on Hartree-Fock method), Z. Phys, 61 (1930) 126.

[72] J.C. Slater, Atomic shielding constants, Phys. Rev., 36 (1930) 57.

[73] P. Hohenberg and W. Kohn, Inhomogeneous electron gas, Phys. Rev. B, 136 (1964) 864.

[74] W. Kohn and L. Sham, Self-consistent equations including exchange and correlation effects, J. Phys. Rev., 140 (1965) A1133.

[75] (a) H. Thomas, The calculation of atomic fields, Proc. Camb. Phil. Soc., 23 (1927) 542. (b) E. Fermi, Un metodo statistico per la determinazione di alcune priorieta dell'atome, Rend. Accad. Naz. Lincei., 6 (1927) 602.

[76] P. A. M. Dirac, Note on exchange phenomena in the Thomas-Fermi atom, Proc. Cambridge Phil. Roy. Soc., 26 (1930) 376.

[77] J. Kohanoff and N. I. Gidopoulos, Handbook of molecular physics and quantum chemistry, 1st Ed., Chichester: John Wiley & Sons Ltd., 2003.

[78] D. M. Ceperley and B. J. Alder, Ground state of the electron gas by a stochastic method, Phys. Rev. Lett., 45 (1980) 566.

[79] J. P. Perdew and A. Zunger, Self-interaction correction to density-functional approximations for many-electron systems, Phys. Rev. B, 23 (1981) 5048.

[80] S. H. Vosko, L. Wilk and M. Nusair, Accurate spin-dependent electron liquid correlation energies for local spin density calculations, Can. J. Phys., 58 (1980) 1200.

[81] S. Goedecker, M. Teter and J. Hutter, Separable dual-space Gaussian pseudopotentials, Phys. Rev. B, 54 (1996) 1703.

[82] J. P. Perdew, J. A. Chevary, S. H. Vosko, K. A. Jackson, M. R. Pederson, D. J. Singh and C. Fiolhais, Atoms, molecules, solids, and surfaces: Applications of the generalized gradient approximation for exchange and correlation, Phys. Rev. B, 46 (1992) 6671.

[83] A. D. Becke, Density-functional exchange-energy approximation with correct asymptotic behavior, Phys. Rev. A, 38 (1988) 3098.

[84] C. T. Lee, W. T. Yang and R. G. Parr, Development of the Colle-Salvetti correlation-energy formula into a functional of the electron density, Phys. Rev. B, 37 (1988) 785.

[85] A. D. Becke, Density functional thermochemistry III. The role of exact exchange, J. Chem. Phys., 98 (1993) 5648.

[86] J. Jortner and C. Rao, Nanostructured advanced materials. Perspectives and directions, Pure Appl. Chem., 74 (2002) 1491.

[87] M. Pitcher, Nanochemistry - A chemical approach to nanomaterials, Science, 313 (2006) 300.

[88] Y. Xia, P. Yang, Y. Sun, Y. Wu, B. Mayers, B. Gates, Y. Yin, F. Kim and Y. Yan, One-dimensional nanostructures: Synthesis, characterization, and applications, Adv. Mater., 15 (2003) 353.

[89] W. Zhou, Y. Zhang, X. Niu and G. Min, One-dimensional sic nanostructures: synthesis and properties, in 'One-dimensional nanostructures, lecture notes in nanoscale science and technology', ed. Z. M. Wang, Springer, London, (2008) 17.

[90] J. Hu, T. Odom and C. Lieber, Chemistry and physics in one dimension: Synthesis and properties of nanowires and nanotubes, Acc. Chem. Res., 32 (1999) 435.

[91] Z.L. Wang, Zing Oxide nanostructures: growth, proeprties and applications, J Phys.: Condens. Matter, 16 (2004) 829.

[92] X. Bai, P. Gao, Z. Wang and E. Wang, Dual-mode mechanical resonance of individual ZnO nanobelts, Appl. Phys. Lett., 82 (2003) 4806.

[93] W. Hughes and Z. Wang, Nanobelts as nanocantilevers, Appl. Phys. Lett., 82 (2003) 2886.

[94] R.F. Oulton, V.J. Sorger, D.A. Genov, D.F.P. Pile and X. Zhang, A hybrid plasmonic waveguide for subwavelength confinement and long-range propagation, Nature. Photon., 2 (2008) 496.

[95] W. Law, K. Yong, A. Baev, R. Hu and P. Prasad, Nanoparticle enhanced surface plasmon resonance biosensing: Application of gold nanorods, Opt. Express, 17 (2009) 19041.

[96] P. Zijlstra, J. Chon and M. Gu, Five-dimensional optical recording mediated by surface plasmons in gold nanorods, Nature, 459 (2009) 410.

[97] M. Law, J. Goldberger and P. Yang, Semiconducor nanotubes and nanowires, Annu. Rev. Mater. Res., 34 (2004) 83.

[98] C.Zhang, Y. Yan, Y.S. Zhao and J. Yao, Synthesis and applications of organic nanorods, nanowires and nanotubes Annu. Rep. Prog. Chem., Sect. C: Phys. Chem., 109 (2013) 211

[99] X. Zhang, Y. Zhang, J. Xu, Z. Wang, X. Chen, D. Yu, P. Zhang, H. Qi and Y. Tian, Peculiar ZnO nanopushpins and nanotubes synthesized via simple thermal evaporation, Appl. Phys. Lett., 87 (2005) 123111.

[100] L. Vayssieres, On the design of advanced metal oxide nanomaterials, Int. J. of Nanotechnology, 1 (2004) 1.

[101] L. D. Marks, Experimental studies of small particle structures, Rep. Prog. Phys., 57 (1994) 603.

[102] D. Fiorani, A. Testa, F. Lucari, F. D'Orazio and H. Romero, Magnetic properties of maghemite nanoparticle systems: surface anisotropy and interparticle interaction effects, Phys. Rev. B: Condens. Matter, 320 (2002) 122.

[103] Z. Wang, X. Hu, P. Kall and U. Helmersson, High Li+-ion storage capacity and double-electrochromic behavior of sol-gel-derived iron oxide thin films with sulfate residues, Chem. Mater, 13 (2001) 1976.

[104] A.E. Berkowitz, F.T. Parker, F.E. Spada, and D. Margulies, Fine particles in magnetic recording media, in studies of magnetic properties of fine particles and their

relevance to materials science, in: J. L. Dormann, D. Fiorani (Eds.), Elsevier, Amsterdam (1991) 309.

[105] S. Alaei, S. Erkoc, Structural properties of beta-Fe2O3 nanorods under strain: molecular dynamics simulations, J. Comput. Theor. Nano S., 11 (2014) 242.

[106] U.S. Rochelle M. Cornell, The iron oxides: structure, properties, reactions, occurrences and uses, 2nd Completely Revised and Extended Edition, 2006.

[107] A. Martinez, M. Garcia-Lobato, D. Perry, A. Barranon, study of the properties of iron oxide nanostructures, In: Research in New Nanotechnology Developments, (2009) 183.

[108] L. B. Dor, E. Fischbein, and Z. Kalman, Acta Crystallographica B, 667 (1976).

[109] A. Pedone, G. Malavasi, M.C. Menziani, A.N. Cormack, and U. Segre, A new self-consistent empirical interatomic potential model for oxides, silicates, and silica-based glasses, J. Phys. Chem. B, 110 (2006) 11780.

[110] C. Weigel, L. Cormier, G. Calas, L. Galoisy and D. T. Bowron, Intermediate-range order in the silicate network glasses Na $Fe_xAl_{1-x}$ $Si_2O_6$ (x=0, 0.5, 0.8, 1): A neutron diffraction and empirical potential structure refinement modeling investigation, Phys. Rev. B. 78 (2008) 064202 (11).

[111] P. M. Morse, Diatomic molecules according to the wave mechanics .II. vibrational levels, Phys. Rev., 34 (1929) 57.

[112] P. Atkins and J. Paula, Physical chemistry, 8th Ed., W. H. Freeman and Company, New York, 2006.

[113] J. E. Jones. On the determination of molecular fields. I. From the variation of the viscosity of a Gas with temperature. In Proc. R. Soc. Lond., A, 106 (1924) 441.

[114] J. C. Slater, Quantum theory of molecules and solids, New York, MaGraw-Hill, 1963.

[115] P. W. Bridgman, Studies in large plastic flow and fracture with special emphasis on the effects of hydrostatic pressure. McGraw-Hill, New York, USA, 1952.

[116] D. A. Mc. Quarrie, Statistical mechanics, Harper Collins, New York, 1976.

[117] D. Frenkel and B. Smit, Understanding molecular simulation: From algorithm to applications, 2nd Ed., Academic Press, San Diego, 2002.

[118] H. J. C. Berendsen, Simulating the physical world: Hierarchical modeling from quantum mechanics to fluid dynamics, Cambridge University Press, Cambridge, 2007.
[119] J. Yarnell, M. Katz, R. Wenzel and S. Koenig, Structure factor and radial distribution function for liquid Argon at 85 °K, Phys. Rev. A, 7 (6) (1973) 2130.
[120] J. Zheng and R. M. J. Dickson, Individual water-soluble dendrimer-encapsulated silver nanodot fluorescence, Am. Chem. Soc., 124 (2002) 13982.
[121] L. A. Peyser, T. -H.Lee and R. M. Dickson, Mechanism of Agn nanocluster photoproduction from silver oxide films, J. Phys. Chem. B, 106 (2002) 7725.
[122] C. D. Geddes, A. Parfenov, I. Gryczynski and J. R. Lakowicz, Luminescent blinking from silver nanostructures, J. Phys. Chem. B, 107 (2003) 9989.
[123] V. Kumar, K. Esferjani and Y. Kawasoe, Computer simulations on clusters: Structures and electronic properties, in: Y. Kawasoe, T. Kondow, K. Ohno (Eds.), Clusters and Nanomaterials, Springer Series in Cluster Science, Springer-Verlag, Berlin, Germany (2001) 9.
[124] I. Chamritski and G. Burns, Infrared- and raman-active phonons of magnetite, maghemite, and hematite: A computer simulation and spectroscopic Study, J. Phys. Chem. B, 109 (2005) 4965.
[125] Z.D. Pozun and G. Henkelman, Hybrid density functional theory band structure engineering in hematite, J. Chem. Phys., 134 (2011) 224706.
[126] P. Tartaj, M.P. Morales, S. Veintemillas-Verdaguer, T. Gonzalez-Carreno and C.J. Serna, The preparation of magnetic nanoparticles for applications in biomedicine, J. Phys. D: Appl. Phys., 36 (2003) R182.
[127] S. Laurent, D. Forge, M. Port, A. Roch, C. Robic, L.V. Elst and R.N. Muller, Magnetic iron oxide nanoparticles: Synthesis, stabilization, vectorization, physicochemical characterizations, and biological applications, Chem. Rev., 108 (2008) 2064.
[128] A.S. Teja and P.-Y. Koh, Synthesis, properties and applications of magnetic iron oxide nanoparticles, Prog. Cryst. Growth Charact. Mater., 55 (2009) 22.

[129] A. Figuerola, R.D. Corato, L. Manna and T. Pellegrino, From iron oxide nanoparticles towards advanced iron-based inorganic materials designed for biomedical applications, Pharmacol. Res., 62 (2010) 126.

[130] G. L. Gutsev, C. W. Bauschlicher, Jr., H. J. Zhai, and L. S. Wang, Structural and electronic properties of iron monoxide clusters $Fe_nO$ and $Fe_nO^-$ (n=2–6): A combined photoelectron spectroscopy and density functional theory study, J. Chem. Phys., 119 (2003) 11135.

[131] L. S. Wang, H. B. Wu and S. R. Desai, Sequential oxygen atom chemisorption on surfaces of small iron clusters, Phys. Rev. Lett., 76 (1996) 4853.

[132] H. B. Wu, S. R. Desai and L. S. Wang, Erratum: Observation and photoelectron spectroscopic study of novel mono- and diiron oxide molecules: $FeO_y^-$ (y = 1-4) and $Fe_2O_y^-$ (y = 1-5), J. Am. Chem. Soc., 118 (1996) 5296.

[133] J. Husband, F. Aguirre, P. Ferguson, and R. B. Metz, Vibrationally resolved photofragment spectroscopy of $FeO^+$, J. Chem. Phys., 111 (1999) 1433.

[134] S. Chang, G. Blyholder and J. Fernandez, Iron-oxygen interactions in an argon matrix, Inorg. Chem., 20 (1981) 2813.

[135] Y. Yamada, H. Sumino, Y. Okamura, H. Shimasaki and T. Tominaga, Mössbauer studies on laser evaporated iron atoms and their reactions with oxygen in argon matrices, Appl. Radiat. Isot., 52 (2000) 157.

[136] L. Andrews, G. V. Chertihin, A. Ricca, and C. W. Bauschlicher, Reactions of Laser-Ablated Iron Atoms with Oxygen Molecules: Matrix Infrared Spectra and Density Functional Calculations of OFeO, FeOO, and $Fe(O_2)$, J. Am. Chem. Soc., 118 (1996) 467.

[137] S. J. Riley, E. K. Parks, G. C. Nieman, L. G. Pobo, and S. Wexler, Metal deficient iron oxide clusters formed in the gas phase, J. Chem. Phys., 80 (1984) 1360.

[138] D. Schröder, P. Jackson, and H. Schwarz, Dissociation patterns of small $Fe_mO_n^+$ (m = 1-4, $n \leq 6$) cluster cations formed upon chemical ionization of $Fe(Co)_5/O_2$ mixtures, Eur. J. Inorg. Chem., 6 (2000) 1171.

[139] D. N. Shin, Y. Matsuda, and E. R. Bernstein, On the iron oxide neutral cluster distribution in the gas phase. I. Detection through 193 nm multiphoton ionization, J. Chem. Phys., 120 (2004) 4150.

[140] G.L. Gutsev, S.N. Khanna, B.K. Rao and P. Jena, Electronic structure and properties of $FeO_n$ and $FeO_n^-$ clusters, J. Phys. Chem. A, 103 (1999) 5812.

[141] Z. Cao, W. Wu and Q. Zhang, The hybrid DFT and molecular orbital study of structure and molecular bonding of $FeO_4$ and $FeO_4^-$, J. Mol. Struct.: THEOCHEM 489 (1999) 165.

[142] N. O. Jones, B. V. Reddy, F. Rasouli, and S. N. Khanna, Structural growth in iron oxide clusters: Rings, towers, and hollow drums, Phys. Rev. B 72, 165411 (2005).

[143] J. Kortus and M. R. Pederson, Magnetic and vibrational properties of the uniaxial $Fe_{13}O_8$ cluster, Phys. Rev. B, 62 (2000) 5755.

[144] H. Shiroishi, T. Oda, I. Hamada and N. Fujima, Structure and magnetism on iron oxide clusters $Fe_nO_m$ (n = 1-5): Calculation from first principles, Eur. Phys. J. D, 24 (2005) 85.

[145] H. Shiroishi, T. Oda, I. Hamada and N. Fujima, Structure and magnetism of anion iron oxide clusters, Mol. Simulat., 30 (2004) 911.

[146] H. Shiroishi, T. Oda, I. Hamada and N. Fujima, Structure and magnetism of anion iron oxide clusters $Fe_nO_m^-$ (n=3,4), Polyhedron 24 (2005) 2472.

[147] B.-F. Xu, C.-L. Yang, M.-S. Wang and X.-G. Ma, Structural, electronic, and magnetic properties of $Fe_nO_m^+$ ($n + m = 5$) clusters, J. Mol. Struct.: THEOCHEM, 957 (2010) 26.

[148] S. López, A.H. Romero, J. Mejía-López, J. Mazo-Zuluaga and J. Restrepo, Structure and electronic properties of iron oxide clusters: A first-principles study, Phys. Rev. B, 80 (2009) 085107.

[149] K. Palotás, A. N. Andriotis, and Alexandros Lappas, Structural, electronic, and magnetic properties of nanometer-sized iron-oxide atomic clusters: Comparison between GGA and GGA+U approaches, Phys. Rev. B, 81 (2010) 075403.

[150] X.-L. Ding, W. Xue, Y.-P. Ma, Z.-C. Wang and S.-G. He, Density functional study on cage and noncage $(Fe_2O_3)_n$ clusters, J. Chem. Phys. 130 (2009 ) 014303.

[151] B. V. Reddy, F. Rasouli, M. R. Hajaligol, and S. N. Khanna, Novel mechanism for oxidation of CO by $Fe_2O_3$ clusters, Fuel, 83 (2004)1537.

[152] P. Giannozzi, S. Baroni, N. Bonini, M. Calandra, R. Car, C. Cavazzoni, D. Ceresoli, G.L. Chiarotti, M. Cococcioni, I. Dabo, A. Dal Corso, S. Fabris, G. Fratesi, S. de Gironcoli, R. Gebauer, U. Gerstmann, C. Gougoussis, A. Kokalj, M. Lazzeri, L. Martin-Samos, N. Marzari, F. Mauri, R. Mazzarello, S. Paolini, A. Pasquarello, L. Paulatto, C. Sbraccia, S. Scandolo, G. Sclauzero, A.P. Seitsonen, A. Smogunov, P. Umari and R.M. Wentzcovitch, QUANTUM ESPRESSO: A modular and open-source software project for quantum simulations of materials, J. Phys.: Condens. Matter 21, (2009) 395502.

[153] D. Vanderbilt, Soft self-consistent pseudopotentials in a generalized eigenvalue formalism, Phys. Rev. B, 41 (1990) 7892.

[154] J.P. Perdew and A. Zunger, Self-interaction correction to density-functional approximations for many-electron systems, Phys. Rev. B, 23 (1981)5048.

[155] H.J. Monkhorst and J.D. Pack, On special points for Brillouin Zone integrations, Phys. Rev. B, 13 (1976) 5188.

[156] S. Alaei, S. Jalili and S. Erkoc, Study of Electronic and Magnetic Properties of $(Fe_2O_3)_n$ Clusters Using Density Functional Theory, Ind. J. Mater. Sci. Thechnol., 2014 (in press).

[157] L. W. Finger and R. M. Hazen, Crystal structure and isothermal compression of $Fe_2O_3$, $Cr_2O_3$ and $V_2O_3$ to 50 kbars, J. Appl. Phys. 51 (1980) 5362.

[158] R. Li and L. Cheng, Structural determination of $(Al_2O_3)_n$ (n=1-7) clusters based on density functional calculation, Comput. Theor. Chem., 996 (2012) 125.

[159] A. Kirilyuk, A. Fielicke, K. Demyk, G. von Helden, G. Meijer and Th. Rasing, Ferrimagnetic cagelike $Fe_4O_6$ cluster: Structure determination from infrared dissociation spectroscopy, Phys. Rev. B, 82 (2010) 020405.

[160] H. van Leuken and R.A. de Groot, Half-metallic antiferromagnets Phys. Rev. Lett., 74 (1995) 1171.

[161] X. Hu, Half-Metallic Antiferromagnet as a Prospective Material for Spintronics, Adv. Mater. 24 (2012) 294.

[162] R.E. Rudd and W.E. Pickett, Single-spin superconductivity: Formulation and Ginzburg-Landau theory, Phys. Rev. B, 57 (1998) 1.

[163] W.E. Pickett and H. Eschrig, Half metals: from formal theory to real material issues, J. Phys.: Condens. Matter, 19 (2007) 315203.

[164] J. M. D. Coey, M. Venkatesan, M. A. Bari, Half-Metallic Ferromagnets, High Magnetic Fields in Lecture Notes in Physics, Vol. 595, (Eds.: C. Berthier, L. P. Levy, G. Martinez), Springer Berlin Heidelberg, 2002, 377.

[165] K. Srinivasu and S.K. Ghosh, Electronic structure, optical properties, and hydrogen adsorption characteristics of supercubane-based three-dimensional porous carbon, J. Phys. Chem. C, 116 (2012) 25015.

[166] C. Sun and D.J. Searles, Lithium storage on graphdiyne predicted by DFT calculations, J. Phys. Chem. C, 116 (2012) 26222.

[167] C. Li, J. Li, F. Wu, S.-S. Li, J.-B.Xia and L.-W.Wang, High capacity hydrogen storage in Ca decorated graphyne: A first-principles study, J. Phys. Chem. C, 115 (2011) 23221.

[168] Y. Jiao, A. Du, M. Hankel, Z. Zhu, V. Rudolph and S.C. Smith, Graphdiyne: A versatile nanomaterial for electronics and hydrogen purification, Chem. Commun. 47 (2011) 11843.

[169] S.W. Cranford and M.J. Buehler, Selective hydrogen purification through graphdiyne under ambient temperature and pressure, Nanoscale, 4 (2012) 4587.

[170] H. Du, Z. Deng, Z. Lu, Y. Yin, L. Yu, H. Wu, Z. Chen., Y. Zou, Y. Wang, H. Liu and Y. Li, The effect of graphdiyne doping on the performance of polymer solar cells, Synthet. Met. 161 (2011) 2055.

[171] D. Malko., C. Neiss, F. Cines and A. Gorling, Competition for graphene: Graphynes with direction-dependent dirac cones, Phys. Rev. Lett. 108 (2012) 086804.

[172] J. Zhou, K. Lv, Q. Wang, X. S. Chen, Q. Sun and P. Jena, Electronic structures and bonding of graphyne sheet and its BN analog, J. Chem. Phys. 134 (2011) 174701.

[173] E. Konstantinov, S.O. Dantas and P.M.V.B. Barone, Electronic and elastic properties of two-dimensional carbon planes, Phys. Rev. B 74 (2006) 035417.

[174] V.R. Coluci, S.F. Braga, S.B. Legoas, D.S. Galvao and R.H. Baughman, Families of carbon nanotubes: Graphyne-based nanotubes, Phys. Rev. B, 68 (2003) 035430.

[175] V.R. Coluci, S.F. Braga, S.B. Legoas, D.S. Galvao and R.H. Baughman, New families of carbon nanotubes based on graphyne motifs, Nanotechnology 15 (2004) S142.

[176] A.N. Enyashin, Y.N. Makurin and A.L. Ivanovskii, Quantum chemical study of the electronic structure of new nanotubular systems: α-graphyne-like carbon, boron–nitrogen and boron–carbon–nitrogen nanotubes, Carbon 42 (2004) 2081.

[177] S. Tongay, S. Dag, E. Durgun,, R.T. Senger and S. Ciraci, Atomic and electronic structure of carbon strings, J. Phys.: Condens. Matter.,17 (2005) 3823.

[178] V. Ongun Ozelik and S. Ciraci, Size dependence in the stabilities and electronic properties of α-Graphyne and its boron nitride analogue, J. Phys. Chem. C, 117 (2013) 2175.

[179] H. Zhang, M. Zhao, X. He, Z. Wang, X. Zhang, and X. Liu, High mobility and high storage capacity of lithium in sp–$sp^2$ hybridized carbon network: The case of Graphyne, J. Phys. Chem. C, 115 (2011) 8845.

[180] Z. Lin, W. Yu, Y. Wang, and X. Ning, Predicting the stability of nanodevices, EPL, 94(4) (2011) 40002.

[181] L. Wang-Yao, L. Zheng-Zhe, X. Jian-Jun, and N. Xi-Jing, A statistical model for predicting thermal chemical reaction rate: Application to bimolecule reactions, Chin. Phys. Lett. 29 (2012) 080504.

[182] Y-G. Xu, C. Ming, Z,-Z. Lin, F.-X .Meng, and X-J Ning, If graphynes turn into graphene: the thermal stability study, arXiv: 1310.2116v1 (2013).

[183] Z. Liu, G. Yu, H. Yao, L. Liu, L. Jiang and Y. Zheng, New J. Phys., 14 (2012) 113007.

[184] J. He, S.Y. Ma, P. Zhou , C. X. Zhang CX, C. He and L.Z. Su, Magnetic properties of single transition-metal atom absorbed Graphdiyne and Graphyne sheet, arXiv:1207.4380 (2013).

[185] J. He , P. Zhou , S.Y. Ma, C.X. Zhang, C He and L.Z. Su, Magnetic exchange coupling and anisotropy of 3d transition-metal nanowire on the surface of Graphyne sheet, arXiv:1305.1791v2 (2013).

[186] A.N. Enyashin and A.L. Ivanovskii, Fluorographynes: stability, structural and electronic properties, Superlattice. Microst., 55 (2013) 75.

[187] J. Tan, X. He and M. Zhao, First-principles study of hydrogenated graphyne and its family: Stable configurations and electronic structures, Diam. Relat. Mater., 29 (2012) 42.

[188] S. G. Hao, G. Zhou, W. H. Duan, J. Wu and B. L. Gu, Tremendous spin splitting effects in open boron nitride nanotubes: application to nanoscale spintronic devices, J. Am. Chem. Soc., 128 (206) 8453.

[189] E. Durgun, S. Dag, V.M.K. Bagci, O. Gulseren, T. Yildirim and S. Ciraci, Systematic study of adsorption of single atoms on a carbon nanotube, Phys. Rev. B, 67 (2003) 201401.

[190] E. Durgun, S. Dag, S. Ciraci and O. Gulseren, Energetics and electronic structures of individual atoms adsorbed on carbon nanotubes, J. Phys. Chem. B, 108 (2004) 575.

[191] Y. Yagi, T.M. Briere, M.H.F. Sluiter, V. Kumar, A.A. Farajian and Y. Kawazoe, Stable geometries and magnetic properties of single-walled carbon nanotubes doped with 3*d* transition metals: A first-principles study, Phys. Rev. B, 69 (2004) 075414.

[192] S. Jalili, M. Akhavan and J. Schofield, Study of titanium adsorption on perfect and defected $BC_3$nanotubes using density functional theory, Mol. Phys., 111 (2013) 888.

[193] S. Alaei, S. Jalili, S. Erkoc, Study of the influence of transition metal atoms on electronic and magnetic properties of graphyne nanotubes using density functional theory, Fuller. Nanotub. Carbon Nanostruct. (2014) (in press)**,** DOI: 10.1080/1536383X.2013.863767.

[194] R. Saito, M. Fujita, G. Dresselhaus, and M. S. Dresselhaus, Electronic structure of graphene tubules based on $C_{60}$**,** Phys. Rev. B, 46 (1992) 1804.
[195] V. R. Coluci, D. S. Galvao and R. H. Baughman, J. Chem. Phys., 121 (2004)7.
[196] J.P. Perdew, K. Burke and M. Ernzerhof, Generalized gradient approximation made simple, Phys. Rev. Lett., 77 (1996) 3865.
[197] Y.S. Wang, P.F. Yuan, M. Li, W.F. Jiang, Q. Sun and Y. Jia, Calcium-decorated graphyne nanotubes as promising hydrogen storage media: A first-principles study, J. Solid State Chem., 197 (2013) 323.
[198] Y.-L. Mao1, X.-H. Yan and Y. Xiao, First-principles study of transition-metal-doped single-walled carbon nanotubes, Nanotechnology, 16 (2005) 3092.
[199] K. Tsukagoshi, B.W. Alphenaar and H. Ago, Coherent transport of electron spin in a ferromagnetically contacted carbon nanotube, Nature, 401 (1999)572.

## CURRICULUM VITAE

PERSONAL INFORMATION

Surname, Name: Alaei, Sholeh
Nationality: Iranian
Date and Place of Birth: 11 Sep. 1980, Urmia
Marital Status: Single
Phone: +90 531 827 20 56
email: e170648@metu.edu.tr

EDUCATION

High School: Shahed High School, Urmia, 1998.
B.S.: Department of Physics, Urmia Univeristy, Iran, Sep. 2002.
M.Sc: Department of Physics, Tabriz Univeristy, Iran, March, 2005
Fall 2009 - present Ph.D. Program, Middle East Technical University (METU), Ankara

WORK EXPERIENCE

2005- 2009 Department of Physics, Islamic Azad University of Iran, Urmia Branch, Research Assistant

PUBLICATIONS

1. Saleh Asharfi and Sholeh Alaei, Measuring γ –ray dose of terrestrial samples using β-γ Spectrometry, Iran. J. Radiat. Res., 8(4), 237- 242, 2011.

2. Sholeh Alaei and Sakir Erkoc, Structural properties of β-Fe2O3 nanorods under strain: molecular dynamics simulations, J. Comput. Theor. Nanosci. 11 (2014) 242-248.

3. Sholeh Alaei, Seifollah Jalili, Sakir Erkoc, Study of the influence of transition metal atoms on electronic and magnetic properties of Graphyne nanotubes using density functional theory, Fullerenes, Nanotubes and Carbon Nanostructures Journal (in press). DOI: 10.1080/1536383X.2013.863767.

4. Sholeh Alaei, Seifollah Jalili, Sakir Erkoc, Study of electronic and magnetic properties of $(Fe_2O_3)_n$ clusters using density functional theory, Indian Journal of Material Sciences and Technology (IJMST) (in press).

PROCEEDINGS PRESENTED IN INTERNATIONAL MEETINGS

1. Sholeh Alaei, Saleh Ashrafi, Sattar Anvarian, 'Natural radioactivity in soil, water and building materials of Marand areas of Iran', 27-30 April, 2004, 2nd International Conference on Nuclear Science and Technology, Shiraz, Iran (Speaker).

2. Sholeh Alaei, Sakir Erkoc, 'Structural properties of $Fe_2O_3$ nanorods under strain: molecular dynamics simulations', 27 June -1 July, 2011, 7th Nanosceince and Nanotechnology Conference, Istanbul, Turkey (Poster).

3. Sholeh Alaei, Seifollah Jalili, Sakir Erkoc, 'Density functional theory study of the interaction of transition metal atoms with Graphyn nanotubes: electronic and magnetic properties', 2-7 June, 2013, 7th Molecular Quantum Mechanics Congress, Lugano, Switzerland (Poster).

PS:

The publications 2-4 and the proceedings 2-3 are the results of this thesis study.